MORPHOLOGICAL TOWER : A TOOL FOR MULTI-SCALE IMAGE PROCESSING

Susanta Mukhopadhyay

Indian Statistical Institute

203, Barrackpore Trunk Road

Calcutta 700 035

India

Thesis submitted to Indian Statistical Institute for partial fulfillment of the requirements for the degree of Doctor of Philosophy

To My Parents

Abstract

An image is a recorded replication of natural scene or objects using suitable sensor and recording media. The visual quality of the recorded image may be enhanced using various types of low-level processing namely *noise smoothing, contrast enhancement.* The images of the same scene recorded by several sensors reveal more information but in their own respective ways. This advantage of multi-sensor imaging system is realized through the *fusion* of the multimodal images. One more important higher-level processing is segmentation where the image is decomposed into a set of meaningful regions (e.g. objects and background). An image, in general, contain objects of varying scales or size. Therefore the objects of an image should be treated according to its scale. Image processing operations in which the objects are treated as per their scales are termed as *multi-scale* techniques. The associated scale-space should satisfy a number of criteria namely *causality, rotational invariance, edge localization, scale-invariance, scale-calibratedness.* Mathematical morphology is a special class of image processing technique, that, by and large, preserves the shape of the features in the filtered versions of the image. Morphological operations may be extended in multi-scale sense. Multi-scale morphological operations take care of both the scale and the shape of the features in an image. In this thesis we have implemented a morphological scale-space, based on structural opening and closing with convex structuring element, using a stack of images of same size and refer it by *morphological tower.* Then the proposed implementation has been employed as a *tool* to solve a number of problems in image processing which include noise smoothing, contrast enhancement for graylevel images, contrast enhancement of color images, fusion of multimodal 2D images and segmentation of graylevel images.

In noise smoothing, the features of the image at various scales corrupted with noise, are extracted and stacked in different levels of morphological towers. While constructing the smoothed image by recombining the feature images we assign progressively

smaller weights to feature images at lower scales since the noise affects the features of smaller scales more. In local contrast enhancement the approach is same as that of noise smoothing except the order emphasis given to the feature images. The construction of locally enhanced image involves recombining the feature images with progressively more weights to features of smaller scales.

Enhancing the contrast of color images is an extension of that of graylevel images. The intensity image constructed by considering the magnitude of the color vector at pixel location is enhanced like a graylevel image. The enhanced color image is obtained by combining the enhanced intensity image with the preserved direction cosines. The hue and the saturation of the color image are preserved.

In image fusion, the scale-specific features extracted from the registered pair of images are stacked in different morphological towers. At each scale we select the features which are best represented in any of the modalities. The selected features are combined to construct the fused image.

In segmentation, the proposed algorithm extracts and identifies the scale-specific features which either grow, or merge or saturate with the increment in scale. The contours of the features which are either merging or saturating with increasing scale are traced. Finally the contours of all features of all scales are integrated.

We have presented the strong and weak points of the proposed implementation of the multi-scale representation of the graylevel image in the concluding section. The scopes for further research are also suggested.

Acknowledgment

I am grateful to my supervisor Prof. B. Chanda of Electronics and Communication Sciences Unit (ECSU), Indian Statistical Institute, Calcutta for having introduced me to the exciting field of image processing and computer vision. I am fortunate to have had the opportunity to share some of his great knowledge in the field.

I thank all Professors of ECSU for their kind cooperation. I am grateful to Prof. D. Dutta Majumder for his invaluable advises and continuous encouragement. I wish to express my gratitude to Prof. J. Das and Prof. A. K. De for their immense help and strong support. I am also very much indebted to Prof. N. R. Pal and Prof. S. Pal for their continuous encouragement. I am grateful and indebted to Dr. D. P. Mukherjee for the powerful drive and motivation he gave me during the last half of my research program.

I wish to convey my gratitude to Prof. P. K. Nandy of B.E. College, Howrah, for his invaluable opinions and suggestions.

I am grateful to Mr. D. Chakraborty, SRF, ECSU, for his technical assistance.

I am thankful to all staff members of ECSU.

I am also grateful to my friends of the Machine Intelligence Unit, ISI.

I would like to thank Prof. C. A. Murthy of Machine Intelligence Unit, Indian Statistical Institute and Dr. P. Ghosh of Wipro GE Medical systems, Bangalore, India for technical discussions.

Finally, I would like to express my gratitude for the support and encouragement I have received from my parents.

Contents

List of Figures

List of Tables

Chapter 1

Introduction

1.1 Importance of Image Processing

A major part of human perception of the world enriched with dynamically evolving information content takes place through the *vision* system. The human vision system acquires information from 3-d objects or scenes, processes the acquired information, and builds knowledge about the viewed object or scene. The prime objective of computer vision system is to realize an expert system which can perform like the human visual system. A typical computer vision system acquires data employing suitable sensors, processes the acquired information using standard methodologies. The human visual system is more efficient than the computer vision system as far as the factors like *precision, speed of operation, accuracy* etc. are concerned. However, human vision system has got a number of limitations too. It has to depend solely on the eye in visualizing the objects. The spectral range of vision of our eye is band-limited. Computer vision system, on the other hand, has the scope of employing a number of sensors with different ranges of visibility. A computer vision system may

employ *x-ray, infra-red ray, ultrasonics* etc. in viewing the object or the scene under study. The accessibility of the object or scene under study is another important factor to be considered for comparison. For example, the human vision system has no access to biological organs like cells, brain-matters, bones etc. Also it can not view a remote object as efficiently as a satellite. However, the computer vision systems mostly work on recorded 2-d representation of the 3-d objects. The reduction in dimensionality causes enormous loss in the information content of the objects. Digital image processing involves both high-level and low-level operations on the acquired image data to facilitate building up knowledge about the objects under study.

A digital image is a viewable 2-d representation of data. Almost every field of scientific studies involves observation and analysis of collected or recorded data. These data may be represented in a viewable form as an image. The formation of digital image, thus, involves various steps. The visual quality and the information content of the recorded image may not be sufficient to render the image successfully for further processing and analysis. In addition, certain information are readily visible in the image while some are not. Information which are not readily visible in the image need special treatment. The main aim and objective of this thesis is to realize a generalized tool for computer-aided image processing and analysis. However, for various reasons the reproduction of an object or scene onto an image incorporates a number of overheads which are to be managed efficiently. Let us have a look at some of the common factors influencing the visual quality and information content of an image. Discussions of the issues are limited to the extent of the scope of the thesis work.

1.2 Factors affecting the quality of digital images

There are several factors controlling the visual quality of an image. Some of the dominant factors relevant to the thesis works are discussed below.

- **The effect of noise**

  The first and foremost factor to be considered is the effect of noise on the recorded image. Noise is inevitably present in any physical system. The medium surrounding the object is often a vital source of noise. The recording medium is also responsible for introducing noise into the image. Apart from these there are other sources of noise which may result from various reasons. An example is the bit error occurring during image data communication. Irrespective of the source and type of noise, the overall effect of noise is a gross degradation in the visual quality of the image. In general, the exact *type* of noise and the spatial position of their occurrences are not known *a priori*. As a result, there always exist a confusion in discriminating signal from noise. Sometimes the effect of noise in the recorded image may be severe to such an extent that the image may not be usable without removal or smoothing of noise from it.

- **The effect of ambient light intensity**

  Another important issue is the availability of the ambient light while recording the image. An inadequate ambience causes poor illumination of the objects. The difference between the maximum and minimum illumination or the intensity is termed as the dynamic range of the image. If the entire dynamic range of intensity is not used exhaustively, the image is said to suffer from poor contrast. Thus, a poor ambience results in in-exhaustive utilization of the dynamic range of intensity in the recorded image. For a typical gray-level image this is manifested by poorly discernible dark (or bright) features over bright (or dark) background. The lack in clarity of the image features makes the image

unsuitable for subsequent use. In some cases, it may so happen that in spite of the exhaustive use of the entire dynamic range of gray-level, the contrast or visibility at some local regions of the image may be poor enough to depict the features at those regions with required clarity. The problem of such poor local contrast results in poor sharpness of various subtle image features at different local regions. As a remedy we have to make use of local or global contrast enhancement scheme.

The issues discussed above have serious influence on the visual quality of the acquired image data. For a meaningful usage of the acquired image data, the image must be subjected to a set of *low-level processing*. These low-level processing include *noise smoothing*, *contrast stretching*, *restoration*, *sharpening* etc. These are broadly termed as image *enhancement* techniques. The picture quality of an image is also degraded due to object discernibility. In such cases the image needs to undergo higher level processing. The problem of object discernibility in an image may be caused by various reasons. We discuss two such causes which are relevant to this thesis.

- **The effect of sensor**

  The sensor involved in the recording of the image plays a very important role in depicting the features. Different objects in the same scene may not be detected with equal clarity by the same sensor. Due to this difference in response, a sensor fails to visualize all the objects of the same scene with equal clarity. The image formed using a sensor therefore fails to depict all salient and subtle features. This is true for almost all sensors. The response of objects to different sensors are sometimes complementary and sometimes redundant. Therefore the images of the same scene recorded by several sensors reveal more information but in their own respective way. Analysing the set of such images without integrating them does not reduce the inconvenience. The ample scope of multi-

sensor imaging system is not realized as long as the multimodal images are not *fused* in terms of their information content.

- **Ambiguity among the regions**

  Different regions of interest in the image might require different kind of processing. The regions are not separated automatically. Thus, an image even after undergoing several relevant preprocessing and refinement might be found to be not suitable for a direct analysis for image description and interpretation unless and until the different regions of interest within the image are separated. This task is performed by an operation called *segmentation*. The purpose of image segmentation is to divide an image into a number of disjoint regions so that the features within each region have visual similarity with respect to properties like gray-level, color, reflectivity and texture. The segmented homogeneous regions are mutually disjoint subsets of the entire image. As already mentioned, each segment or some of the segments might need independent or different kind of processing for exploiting subtle information inherent in it. For example, a remotely sensed image representing the temperature profile of a region requires proper stratification of the region into a number of disjoint sub-regions calibrated according to the thermal profile. A biomedical image of a human brain with a lesion, in a similar way, needs a proper contouring the lesion for computer aided diagnosis of the disease. A segmentation algorithm aims at serving the purpose stated above. Another important role of segmentation algorithm is to keep object-based information of an image.

1.3 Image processing tools and techniques

In this section we briefly mention the image processing tools we have used. Image processing techniques are broadly classified into two groups (i) spatial domain

techniques and (ii) frequency domain techniques. In the spatial domain techniques various types of neighborhood operators are directly applied on the pixel values of the image. In the frequency domain techniques, operators are applied on the transformed version or the spectrum of the image. In this thesis we have adopted spatial domain techniques where the operators employed are borrowed from a class of well defined set of operators called *morphological operators.*

1.3.1 Mathematical morphology

Mathematical morphology is a well-known technique used in image processing and computer vision. The application of *mathematical morphology* [96, 142, 87] to image processing and analysis has initiated a new approach for solving a number of problems in the related field. This set theoretic, shape oriented approach treats the image as a set and the kernel of operation, commonly known as *structuring element* (SE), as another set. Different standard morphological operations namely *dilation, erosion, opening, closing* etc. are basically set-theoretic operations between these two sets. The shape and the size of the SE play an important role in detecting or extracting features of given shape and size from the image. Mathematical morphology has extensive applications in various problems of image processing.

1.4 Multi-scale processing

In recent years, the multi-scale and multi-resolution approaches in image processing problems have become quite popular for various reasons. In general, an image comprises of objects or features of different scales. On the other hand, image processing techniques often make use of some pre-specified threshold or parameter values. In-

deed these parameter values, when chosen globally, irrespective of scales of the objects or features, can not do justice to them equally. In other words an operation while being executed on an image must treat the objects or features according to their scales. Thus the need for processing the image based on the size or scale of different objects or features present in the image has initiated several *multi-scale* and *multi resolution* techniques. Multi-scale techniques extract scale specific information from the image, process them and finally integrate them to produce desired output. The entire process may be realized through linear or non-linear filters and, accordingly, it gives rise to a linear or non-linear scale space representation of the image under study. Detailed descriptions about the scale-space filtering in connection to image processing are available in [69, 21, 168, 71, 68, 83, 7, 8]. Quite often the multi-scale algorithms help in considerable reduction in time and computational complexities. Mathematical morphology and multi-scale processing may be combined to avail the advantages of both the methods [13, 22, 15, 24, 122].

1.5 Problems undertaken in the thesis work

The problems covered in this thesis work are

- noise smoothing,
- local contrast enhancement of gray-scale images,
- local contrast enhancement of color images,
- multimodal image fusion, and
- segmentation

1.5.1 Noise Smoothing

Problem description

A very common source of degradation in a digital image is noise contamination. Noise may be present in an image due to different reasons and its effect in degrading the image is different for different kind of noise. The image corrupted with noise generally suffers from having low *signal-to-noise* ratio and may not be suitable for further processing without removing or reducing the effect of noise in it. For example, a biomedical image corrupted with noise can not be used reliably for clinical diagnosis of disease. A satellite image corrupted with speckle noise fails to represent the remote-sensed data of, say, a geographical terrain. Hence removal of noise from the image is of utmost importance in image processing and analysis. However, removal of noise by every known noise cleaning algorithm is associated with partial removal of the desired signal component also. For example, *mean filter*s [131] generally blur the edges and the corner points present in the image.

Since the removal of noise may affect information content of the image it becomes quite relevant to deal with the behavior of the noise. This mainly includes statistical modeling, analysis and estimation of the associated noise. Most often the exact nature or type of the noise are not known beforehand. However, the type of noise degrading the image is dependent on the imaging system. Accordingly a suitable mathematical or statistical noise model may be fit to quantify or estimate the parameters of the model. The statistical behavior of noise is generally described by a probability density function. The noise process may be linear or non-linear and the noise may be additive or multiplicative. The noise may be signal dependent or signal independent as well. As a result, a noise removal scheme or algorithm cannot be identically efficient in removing all kinds of noise from images.

Related works

There are various noise removal schemes each having their own merits and demerits. Some of these are spatial domain techniques while others are frequency domain techniques. The spatial domain techniques, usually, smooth noise by employing the knowledge acquired from the neighborhood of each pixel in the noisy image. For example, the well known *mean filter* [131] replaces intensity at each pixel of the noise corrupted image by the average intensity computed over a prescribed neighborhood. In other variants of mean filters this average is computed by assigning intuitive weightages to the pixels contained in the neighborhood. Davis et. al. have proposed an algorithm for noise cleaning which employs iterative local averaging [37]. *Median filters* [131], on the other hand, compute median in stead of the average. While mean filters have the problem of blurring the edges present in the image, median filters, by and large, preserve them by reducing the effect of statistical outliers present in the local neighborhood. Crimmins [35] developed a geometric filter which has proved to be efficient in removing speckle noise from satellite image data. Restoring an image from its noisy version is performed in frequency domain by means of *low pass filtering, inverse filtering, Wiener filtering* [131]. However, almost all conventional noise removal algorithms mentioned above do not take care of shapes and scales of the objects or features present in the image.

Morphological techniques are being used for solving various image processing problems including noise smoothing. The most common noise removal techniques using mathematical morphology are *opening* and *closing* [62] or their cascades known as *alternating sequential filters* [148]. Safa and Flouziat [133] have used mathematical morphology in removing speckle from radar images. Schonfeld and Goutsias [140] have done an optimal morphological pattern restoration from noisy binary images. Lin et.al. [76] have used morphology in reducing noise of VQ encoded images through anti-gray coding. Floreby et. al. [41] have developed a noise removal technique using

morphological pyramid decomposition and modified reconstruction. A scheme for morphological anisotropic diffusion for smoothing noise from gray-scale images has been suggested by Segall and Acton [141]. In our work [117, 111] we have devised a noise smoothing technique using multi-scale morphology that also preserve edges.

1.5.2 Local contrast enhancement of graylevel images

Problem description

A poor illumination of the object or the scene to be imaged causes a low contrast in the image. Such a degraded image cannot render itself successfully for subsequent processing toward image understanding and interpretation. The ad-hoc methods normally applied for global contrast enhancement does not improve the local contrast. The local contrast enhancement requires the algorithm to take care of the local information. The objective is to stretch the local histogram without appreciably affecting the global histogram of the image. The basic notion of local contrast enhancement is to stretch the difference of the intensity at a pixel location from the mean intensity value over some prescribed neighborhood surrounding it. However, it is worthy to incorporate the shape information of the local features along with the local intensity statistics while performing local contrast stretching.

Related works

The problem of poor contrast in the degraded image is usually solved by *histogram stretching* [60, 131] or by *histogram equalization* technique [131, 52]. There are few variations of histogram equalization technique e.g. histogram modification [50, 51]. The conventional histogram equalization technique treats the image globally. Since

the image characteristics differ considerably from one region to another in the same image, it is reasonable to adopt a context-sensitive technique based on local contrast variation especially when the local histogram does not follow the global histogram. Dorst [39] adapted histogram stretching method over a neighborhood around the candidate pixel for local contrast stretching. While, various modifications [124, 121, 109] of histogram equalization (or modification) are suggested based on adapting the same over a sub-region of the image. Contrast stretching methods using local statistics are also reported [78, 79, 119]. Acton et. al. [4] have proposed an image enhancement technique based on nonlinear regression that employs simulated annealing. Attas et. al. [10] have devised a variational approach to local contrast enhancement through a suitable optimization of some desirable characteristics of gray-level histogram of output image. Similar approach for constrained local histogram equalization has been adopted by Zhu et. al. [170]. Boccignone and Picariello [19] have suggested a multi-scale approach to contrast enhancement using a non-linear scale-space representation of image generated by anisotropic diffusion. Another multi-scale contrast enhancement technique is developed by Toet [154] through non-linear pyramid recombination. In our work [113, 112] we have devised a technique for local contrast enhancement of grayscale images using multi-scale morphology.

1.5.3 Local contrast enhancement of color images

Problem description

With the rapid increase in the usage and applications of color video media, it has become a necessity to develop tools and algorithms for color image processing. Some concepts and tools used in gray-level image operations may be extended in case of color images. However, the treatments generally performed on gray-level images may not be readily extendible to case of color images due to various practical issues. The

visual appearance of a color image is controlled by various factors or attributes and uncontrolled modification of any of them may have undesired effect on the appearance and the purpose may be defeated. Unlike gray-scale images, color images keep the color information at each pixel location in the form of a triplet. The eye perceives an overall effect of these triplets. There is no definite guideline as such to alter the values in the 3-tuple at each pixel location so that the color in the resulting image may be viewed with high contrast. Different color models are used in representing and dealing with color information. The commonly used hardware-oriented color models are (i) RGB, (ii) CMY and (iii) YIQ. These models, though are widely used in image processing algorithms, do not reflect intuitive color notions or perception of human vision. For such reasons other models namely HLS, HSV or HVC, for representing color are proposed. For a better description about the widely used color models [Foley et. al. [42]] may be consulted. The red, green and the blue components in an RGB representation of an image are basically the proportions of the primary colors to produce an overall visual effect at each pixel location. In HLS representation, the color information is controlled by the hue component and any modification of this component gives rise to an altogether different color sensation to human eye. For such reasons, almost all kinds of processing of color images tend to keep the hue component substantially unchanged.

Related works

There exist various techniques for contrast enhancement of color images. A scheme for color image enhancement employing genetic algorithm is proposed by Shyu et. al. [144]. Tang et. al. [151] have proposed a method of enhancing color images via Chromaticity diffusion. A hue preserving enhancement scheme for a class of color images is proposed by Gupta et. al. [59]. A multi-scale approach for color image enhancement has been proposed by Toet [156]. Strickland et. al. [150] have

proposed a scheme for color enhancement based on saturation. A description of color equalization methods and its application to color images is given in [20]. In our work [115, 118] we have devised a technique for local contrast enhancement of color images using multi-scale morphology which preserves hue and saturation of the color image.

1.5.4 Multimodal Image Fusion

Problem description

As discussed earlier, in a multi-sensor data acquisition system the image data of an object consists of information acquired by different sensors from different perspective and possibly at different resolution. The clarities of the object features may be different in different imaging modalities. For example, in the arena of biomedical imaging, two widely used modalities, namely the Magnetic Resonance Imaging (MRI) and the Computed Tomographic (CT) scan do not reveal identically every detail of brain structure. While CT scan is especially suitable for imaging bone structure and hard tissues, the MR images are much superior in depicting the soft tissues in the brain that play very important roles in detecting diseases affecting the skull base. These two imaging modalities are thus complementary in many ways and no one is totally sufficient in terms of their respective information content. Thus images resulting from a single modality cannot meet the clinical requirement for the purpose of diagnosis and treatment. However, viewing a series of multimodal images of the same object separately and individually does not provide a better solution because of such inconvenience.

The advantages of multi-sensor data may be fully exploited by integrating the complementary features seen in the images generated by several sensors. A process of

such integration, widely termed as *fusion*, generates an image composed of features that are best detected or represented in the individual modalities. A technically fused image can render itself more successfully for any subsequent processing like object recognition, feature extraction, segmentation etc. in comparison to images of individual modalities. Image data fusion is widely demanded work in the field of multi-sensor data acquisition and interpretation systems.

The first step toward fusion, which may be interpreted as a preprocessing step is the *registration*. Registration is a process of bringing down the constituting images to a common coordinate system subject to some common geometrical references called *ground control points* (GCPs). A feature or object common to all the modalities may have different position and scale in different modalities. Fusion of such images is meaningful only when such common objects (or control points) are made to have identical geometric configuration with respect to size, location and orientation in all the images. In the next step the images are combined to form a single fused image through a judicious selection of features from different images.

Related works

Many researchers have been working in the field of image fusion in connection to biomedical imaging, machine vision, remote sensing applications in defiance and atmospheric fields. Li, Manjunath and Mitra [81] have suggested a multi-sensor image fusion using wavelet transform in which a cascaded sequence of forward and reverse wavelet transform on multimodal images produces a fused image. Matsopoulos et al [97] have devised a hierarchical image fusion scheme that integrates features extracted from morphological pyramids of the multimodal images. Generally, data fusion in multimodal images [1, 33, 84] is partly redundant as some regions are depicted in all the modalities and is partly complementary as each modality highlights

certain features that are absent in images of other modalities. There are various techniques and approaches for fusing multimodal images. Many methods are based on classification of pixels [18]. In this direction Hurn et. al. [67] have suggested a Bayesian probabilistic method for biomedical image fusion. While Mukherjee et. al. [110] have developed an algorithm for fusing CT and MR images based on entropy. In our work [114, 30] we have devised a multi-scale technique for fusion of multi-modal images using morphology.

1.5.5 Segmentation

Problem description

In image segmentation different homogeneous regions of the image are separated out. A segmentation algorithm, therefore, has to employ certain rules in order to classify the pixels of the image into different disjoint regions. Image segmentation techniques may be classified into a number of groups depending on the approach of the concerned algorithm. These include *feature thresholding, contour based techniques, region based techniques, clustering, template matching, statistical methods* etc. Each of these approaches has its own merits and demerits in terms of applicability, suitability, performance, computational cost etc. and no one can meet all the demands. An amplitude thresholding technique, for example, suffers from the problem of yielding contours with non-uniform thickness with discontinuities due to difficulty in selecting optimum threshold. The well-known watershed algorithm - a morphological instance of region based approach, apart from being computationally intensive, suffers from over or under-segmentation due to improper choice of marker points. Besides, the criteria of homogeneities may not always be quite well defined.

Related works

Segmentation of gray level images is an well studied problem. There exist several methods following different approaches for segmenting gray-level images [44]. Gray-level thresholding is one of the oldest techniques for image segmentation [131, 130, 129]. Threshold may be chosen based on *histogram* [28, 27], or by analyzing intra-region and inter-region homogeneity [166]. Canny [26] has suggested a contour based technique employing hysteresis thresholding. A different approach using anisotropic diffusion and PDE-based regularization for segmentation has been developed by Romeny [153], Weickert [165]. Segmentation algorithms based on nonlinear diffusion have been devised by Niessen et. al. [120], Jackway [70]. Salembier and Serra [136] have proposed a multi-scale image segmentation technique using mathematical morphology. A different approach based on local monotonicity has been suggested by Acton et. al. [23]. Another segmentation method proposed by Frank et. al. [43], uses combination of optimal and adaptive thresholding. An overview of border detection and edge linking methods in connection to segmentation can be found in [65]. Region-based segmentation techniques, by and large, detect homogeneity in terms of parameters like gray-level, color, texture etc. A number of region growing techniques for color image segmentation may be found in [47, 139, 162]. A hierarchical merging method has been suggested by Goldberg et. al. [49]. The watershed algorithm and its variants [38, 17, 104, 99, 100. 101, 106, 127, 103, 102, 163] in morphological image processing are found to produce reasonably good segmentation results. The problem of image segmentation has been handled by different types of tools with different underlying concepts. Image segmentation using neuro-fuzzy techniques, genetic algorithms, wavelets, fractals, anisotropic diffusion pyramid etc may be found in [9, 157, 32, 16, 5]. Surveys on image segmentation techniques may be found in [3, 61]. In our work [116] we have devised a multi-scale technique for segmentation of graylevel images using morphology.

1.6 Organization of the thesis

The thesis is organized in the following way. The thesis is divided into 7 chapters. The first chapter presents general discussion on the thesis work. In the second chapter a brief introduction to multi-scale and morphological techniques for image processing are presented. The basic framework for rest of the thesis using multi-scale morphology is also developed in this chapter. The next four chapters cover the five different but interlinked applications of the proposed methodology to image processing. The last chapter discusses on the entire thesis work.

In Chapter 1 (i.e. the current chapter) we first discuss on the general issues and problems of image processing. We emphasize on a few of IP problems to concentrate on the focus area of the thesis. In this context we have first discussed on the factors affecting the visual quality of gray-level images in section 1.2. This section discusses on the effect of noise, ambience, sensors on the quality of the image along with the remedial steps. Section 1.3 briefly mention the tools and techniques we use in this thesis. We have discussed very briefly about multi-scale processing in section 1.4. The set of problems actually handled elaborately in this thesis is mentioned in section 1.5. Sections 1.5.1 - 1.5.5 present the problems one by one in the order they presented in the subsequent chapters. For each problem we have cited the recent works related to that particular problem carried out by other researchers. The chapter ends with brief discussions on the organization of the thesis.

In chapter 2 we discuss the multi-scale image processing and multi-scale morphology in greater details. In section 2.1 we discuss the need and rationale for multi-scale image processing. In sections [2.1.1-2.1.5] we have discussed respectively about (i) various steps of multi-scale image processing, (ii) the properties or criteria to be satisfied by multi-scale operators, (iii) some standard multi-scale techniques (iv) advantages and (v) disadvantages of multi-scale image processing. The scale-space tool conceived

and employed in this thesis is a non-linear morphological scale-space. In this context we have discussed different aspects of mathematical morphology in section 2.2. This covers the basic morphological operations in case of gray-level images, their multi-scale extension etc. Section 2.2.2 discusses on the performance of multi-scale filters realized using conventional morphological operations in satisfying the demands of an ideal scale-space filter. In section 2.2.3 we have discussed on morphological filters by reconstruction. The multi-scale decomposition of the gray-level image among its scale-specific features are presented in section 2.2.4. Finally, the scale-space representation conceived in this thesis work (i.e. the morphological tower) is described in section 2.2.5.

In chapter 3 we consider the problem of image enhancement for gray-scale images. Two basic enhancement problems - namely noise smoothing and contrast improvement are considered. In the first part of chapter 3 we present an edge preserving noise smoothing scheme solved using morphological tower. In section 3.2 we have described the proposed method. Section 3.2.1 describes the theoretical formulation of noise smoothing technique using multi-scale morphology. Section 3.2.2 gives a simplified illustration of the proposed formulation on one-dimensional function. Section 3.2.3 presents elaborately various steps of the implementation of the proposed algorithm. The experimental results and discussions are given in section 3.3. A modification of the proposed scheme considering the noise statistics is presented in section 3.4. In the second part of chapter 3 we present a multi-scale technique for improving the local contrast of gray-level images using morphological tower. Section 3.5 gives an elaborate description of the proposed method. In section 3.5.1 we have first presented the theoretical formulation of local contrast enhancement using multi-scale morphology. A simplified illustration of the proposed scheme is presented in section 3.5.2 by enhancing a function using the proposed scheme. Section 3.5.3 presents elaborately various steps of the implementational aspects of the proposed algorithm. Section 3.6 gives a discussion on the result and its comparison with that of other well-known

techniques. Finally, concluding remarks are cited in section 3.7.

In chapter 4 we present a multi-scale scheme for improving the color contrast using morphological tower. Section 4.2 presents the proposed method in details. The underlying theory of the proposed color image enhancement is discussed in section 4.2.1. The discussion leads to a transformation of a hue preserving color enhancement using the intensity image. Section 4.2.2 presents the theoretical formulation of the proposed enhancement using multi-scale morphology. The effect of the proposed enhancement scheme on the color properties like hue, saturation and lightness is also presented here. Section 4.2.3 presents elaborately various steps of the implementational aspects of the proposed algorithm. Section 4.3 presents the experimental results of the proposed scheme. The experimental results also include the outputs of other standard color enhancement schemes. A quantitative performance analysis is also provided to rate the efficacy of the proposed method. Finally, concluding remarks are cited in section 4.4.

In chapter 5 we present a multi-scale scheme for fusing multimodal $2D$ images using morphological tower. Section 5.2 discusses a point-based method of image registration adopted as a preprocessing step prior to fusion. The proposed method is presented in section 5.3. The theoretical formulation of the proposed multi-scale morphological scheme for fusing multimodal images is presented in section 5.3.1. We present a simple illustration of the proposed scheme in one-dimension in section 5.3.2. This is followed by the implemenational details using morphological towers in section 5.3.3. The experimental results and the discussions are detailed in section 5.4. Concluding remarks are cited in section 5.5.

In chapter 6 we present a multi-scale segmentation scheme for gray-level images using morphological tower. In section 6.2 we have presented the proposed method. The theoretical formulation of the proposed method is discussed elaborately in section

6.2.1 while the implementational details are given in section 6.2.2. The experimental results are presented in section 6.3. Finally, the concluding remarks are given in section 6.4.

The last chapter presents an overall discussion on the thesis work which covers the merits and demerits of the works presented in the thesis and the future direction using the proposed concept.

Chapter 2

Multi-scale Image Processing

2.1 Importance of multi-scale processing

The visual appearance of an image is controlled by several factors which include gray-level, edges, shapes and orientations of the image features, textures and color. Human vision system, in most cases, employs its inherent qualitative or subjective judgment to identify features based on the properties mentioned above. A real image, in most of the cases, consists of objects of various size and shape, color, and possibly texture pattern. Simultaneous recognition of a collection of such objects requires enormous low-level processing. The machine vision system, however, cannot perform qualitative analysis and it has to rely on objective measurements. In machine vision these objective measurements are performed using various operations on the recorded image. These operations are performed either on the spatial domain or on the transformed domain. An example of such operation is edge detection which highlights the edges of the features in the image. Human eye has the intrinsic ability to mark out the edges or contours of the objects present in an image, but, the machine has to rely on

mathematical operations which trace the edges based on, say for example, the homogeneity of the regions. Thus, the processes of image regularization and integration of features are quite natural part of human vision and these need to be implemented in case of machine vision to make it work like human vision.

Dealing with the objects of different size and shape in the image is a very interesting aspect of machine vision [83]. Human eye has the inherent ability to distinguish objects at different scales efficiently [94]. The processing of objects at multiple scales are independent in case of human vision. In most of the prevailing image processing operators, the concept of scale of the objects is not incorporated explicitly. The notion of *local neighborhood* is incorporated in most of the early operators. In human vision the concept of local neighborhood is relative - in the sense that the extent of the local neighborhood is dependent on the scale or size of the object or feature encompassed by the neighborhood. The spatial domain operators in machine vision by and large make use of *masks* spanning the local neighborhood under study. However, the local neighborhood does not take care of the scale of the object contained in that neighborhood. As a result of this the operator processes objects of various scales with equal emphasis. An example may be cited for a better clarification. The image of a natural scene consisting of a crop field along with sky, water, houses on being processed by a mean filter [131] for removal of noise in the sky region may lose the information corresponding to the crop-field.

The need for processing the objects of various sizes present in the image has caused the origination of the scale-specific operations. These scale-specific image processing operations are broadly classified as *multi-resolution* and *multi-scale* techniques. However, the concept of representing an image at multiple scales is not new. Early works related to multi-scale processing may be found in [132, 128, 94, 152, 168, 74].

2.1.1 The steps of multi-scale processing

The basic steps in any type of multi-scale or multi-resolution techniques used in image processing are

- To design a kernel or mask for extracting information at different scales present in the image under study. The mechanism for the extraction of information at different scales may employ linear methods involving the convolution of the image with the kernel at that scale. Alternatively it may employ nonlinear methods like order statistics.
- To process the information extracted from the image at different scales. This processing may be executed in sequence or in parallel.
- To unify or integrate the result of scale-specific processing to reconstruct the final image. The process of integration is a generic term and is used as per context.

Here, an important point to note is that the machine vision must take the effort of unifying the information extracted at different scales or resolutions before it can exploit the immense potentiality of multi-scale processing. The term 'unifying' or 'integrating' is a generic term and there may not exist a unique operation which may represent this operation.

2.1.2 Properties to be satisfied by multi-scale operators

The multi-scale operators must satisfy the following properties [123].

- Causality

The multi-scale operators must exhibit a monotonicity in terms of scale factor. An operator at any scale must not generate any spurious component which is not present in lower scales. This condition resembles the non-causal behavior of filters in signal processing.

- Edge localization

  The operator must not drift the edge features from their respective original positions.

- Directional or rotational invariance

  The kernel must treat the features based on their scales and not on their spatial orientation.

- Calibration of features with respect to scale

  The results are scale-calibrated. The feature image corresponding to a particular scale is supposed to contain all objects of that scale only and no object of any other scale.

- Scale invariance

  The same scale-space can be obtained by starting the multi-scale filtering at any scale.

2.1.3 Some standard multi-scale techniques

The importance of multi-scale signal decomposition scheme has been realized from the early days of image processing. Sometimes the term 'multi-resolution' is used to mean 'multi-scale' since the size of an object is a function of number of pixels and pixel-resolution. Some commonly used multi-scale signal decomposition schemes are

- Gaussian kernel convolution at different scales

- Pyramids
- Wavelets
- M- and N- sieves
- granulometries

In Gaussian scale-space filtering [21] the image is convolved with the Gaussian kernel at different scales (i.e. variance) as described below.

$$G(r, c, \sigma) = e^{-\frac{r^2+c^2}{2\sigma^2}} \tag{2.1}$$

$$F(r, c, \sigma) = f(r, c) * G(r, c, \sigma) \tag{2.2}$$

The description of image features at different scales obtained by the process of linear convolution of the image with Gaussian of varied width was first suggested by Witkin [167]. If the parameter σ of equation (2.2) is varied the family of images represented by $F(x, y, \sigma)$ is called the scale-space images. The Gaussian scale-space is equivalent to computing the solution of the linear diffusion process [74]

$$\partial_t u = \Sigma_i \partial_{x_i, x_i} u =: \Delta u \tag{2.3}$$

$$u(x, 0) = f(x) \tag{2.4}$$

The method being linear is straightforward and easy to implement. It has been found from neurophysiological experiments [94] that the operations performed by the ganglion cells in the retina of human eye resemble the $\nabla^2 G$ operation of the derivative of Gaussian filter.

In pyramid representation, the image is sampled at different resolution and the resulting images are stacked in a pyramid fashion [75]. Reducing an image $g_{n-1}(r, c)$ at the $(n-1)$-th stage to an image in n-th stage is performed using [138]

$$g_n(r, c) = \Sigma_{k=-2}^{k=2} \Sigma_{l=-2}^{l=2} \omega(k, l) g_{n-1}(2 * r + k, 2 * c + l) \tag{2.5}$$

where $\omega(k,l)$ represents a weight factor dependent on the purpose of the application. The reduced image at stage n may be expanded or interpolated to form a new image corresponding to stage $(n-1)$ using [138]

$$g_{n-1}(r,c) = 4\Sigma_{k=-2}^{k=2}\Sigma_{l=-2}^{l=2}\omega(k,l)g_n((r-k)/2,(c-l)/2) \tag{2.6}$$

Thus there is a hierarchy in the pyramid as far as the resolution and the size of the image are concerned. Therefore, the results of filtering operation on the image at coarser resolution are made more and more accurate as one proceeds gradually with the images at finer resolution. This helps in reducing computational cost. The pyramid techniques may employ linear convolution or non-linear morphological operations [58] while constructing the version images at different resolutions. Pyramids have extensive applications in multi-scale processing.

The wavelets methods also employ linear convolution of the image with the mother wavelet and its dilated versions corresponding to different scales. The wavelet transform of a function f at scale s is computed as [36, 85, 2]

$$Wf(u,s) = \int_{-\infty}^{\infty} f(t)\frac{1}{\sqrt{s}}\psi^{\star}(\frac{t-u}{s})dt \tag{2.7}$$

where $\psi^{\star}(\frac{t-u}{s})$ is the wavelet obtained by dilating the mother wavelet ψ with a scale factor s and translating that by u. The wavelet transform has the ability to detect and characterize the transients (analog to edge features) with a zooming procedure across scales. For instance, a high amplitude wavelet coefficient indicates the position of edges. Wavelets also have extensive applications in image processing and computer vision [85]. Signal decomposition using morphological wavelets is presented and extensively treated in [66].

Multi-scale tool employing order statistics [14] makes use of $M-$ and $N-$ sieves. Here the operations opening and closing are defined from the context of connectivity in graph theory as given below

$$\psi_r f(x) \;=\; max_{\xi \in C_r(G,x)} min_{u \in \xi} f(u) \tag{2.8}$$

$$\gamma_r f(x) = min_{\xi \in C_r(G,x)} max_{u \in \xi} f(u) \tag{2.9}$$

$$\mathcal{M}^r = \gamma_r \psi_r \tag{2.10}$$

$$\mathcal{N}^r = \psi_r \gamma_r \tag{2.11}$$

where $C_r(G)$ denotes the set of connected subsets of a graph G. Each subset has r elements and $C_r(G,x) = \{\xi \in C_r(G) | x \in \xi\}$. Thus r serves as the scale factor. This multi-scale non-linear decomposition method, namely sieve decomposition, decompose bounded function to a sequence of increasing scale granule functions that represent the information in a manner that is analogous to the pyramid of wavelets obtained by linear decomposition [13]. Secondly, $M-$ and $N-$ sieves satisfy the causality criterion [15], but does not take care of the shape of objects present in the image. Park and Lee [122] also have proved that the scale-space of an one-dimensional gray-scale signal based on morphological filtering satisfies causality.

Granulometry [96, 142] is an important tool of mathematical morphology and it has extensive applications in material science and biological science. It helps in the extraction of shape information from the image without *a priori* segmentation. The role of granulometry in morphology is identical with that of frequency analyser in signal processing. The family of transformation $\Psi = (\psi_\lambda),\ \lambda \geq 0$ constitute a granulometry if and only if the following conditions are satisfied by the function

$$\psi_\lambda \quad \text{is} \quad \text{increasing} \qquad \forall \lambda \geq 0 \tag{2.12}$$

$$\psi_\lambda \quad \text{is} \quad \text{anti} - \text{extensive} \tag{2.13}$$

$$\psi_\lambda \psi_\mu = \psi_\mu \psi_\lambda = \psi_{max(\lambda,\mu)} \qquad \forall \lambda \geq 0, \mu \geq 0 \tag{2.14}$$

An example of granulometry may be the family of openings [96, 161] with respect to the convex structuring element $\lambda B,\ \lambda \geq 0$. This leads to well-known size distribution and densities [86, 146].

The information extracted at different scales are generally embedded as stack of description in a space termed as *scale-space*. The scale-space meant for house-keeping

the scale-specific information may be linear or non-linear depending on the operators used in generating the scale-space.

2.1.4 Advantages of scale-space filtering

- The processing is more systematic and semantically nearer to that of human vision.
- The processing is inherently parallel. Feature extraction at different scales are normally performed in parallel. The processing of the feature images at all scales may be performed in parallel. The hardware implementation is generally faster.
- The scope for devising a scale-space suitable for some specific applications are widely open. Researchers working in the field of multi-scale processing have wide open scope to devise new scale-space techniques that might serve the purpose of different kind of processing on the image.
- For a given type of scale-space filtering, integrating the scale-specific extracted features in different ways helps in solving various types of problems. For example, in this thesis we have shown that combining the feature images in different ways we can achieve contrast enhancement, noise smoothing, and segmentation.
- Sometimes there may be hierarchy in the multi-scale processing which enables a top-down or bottom-up approach in computation. The solution to the problem at higher or coarse scale helps in finding solution to similar problem at lower scale or vice-versa. The problem of multi-scale segmentation could be an example. This hierarchy helps also in reducing computational costs in some cases.

2.1.5 Disadvantages of scale-space filtering

- The main disadvantage of scale-space filtering is that it has to deal with different scaled versions of the image which often leads to high computational cost.
- In case of multi-resolution pyramidal methods the overhead is to construct images at different resolution and any operation at cross-resolution needs a prior reconstruction. This may introduce error. In case of multi-scale methods (including the proposed one) the space and time complexity are higher because of housekeeping of large number of images at different scales.
- In case of multi-resolution methods there is general requirement that the height and width of the image should be an integer power of 2. Otherwise, the image needs padding which in turn increases space and time complexity.

2.2 Mathematical Morphology

Mathematical morphology is a very powerful technique for processing and analyzing shapes in digital images [142, 62, 147, 56]. The application of *mathematical morphology* to image processing and analysis has initiated a new approach for solving a number of problems in the related field. The concept of mathematical morphology and its application to image processing were introduced by researchers like Matheron [96], Serra [142]. Morphology is now used extensively in various problems of image processing and computer vision particularly where there is strong requirements of analysis of geometrical information contained in the image. In contrast to the linear operators conventionally used in signal processing (like convolution), mathematical morphology is based on non-linear operators. In many respects the morphological operators prove to perform better than other existing linear filters. Application of

morphological operations to image leads to its simplification preserving the main shape characteristics of objects. Since its inception mathematical morphology has observed a steady growth, and during last two decades various morphological operators and processing techniques have been proposed. These include area (size) morphology [158, 159], soft morphology [46, 125], regulated morphology [45], directional morphology [6], differential morphology [88] etc. Several machine vision hardware manufacturers have started including morphological processors. These machines include Golay logic processor [48], Leitz Texture Analysis System TAS [73], the CLIP processor arrays [40],and the Delft Image Processor DIP [80]. Morphological operations are interpreted as set-set processing, function-function processing, function-set processing [86, 90] etc. Morphological operations are extensively used in image processing and computer vision for (i) image preprocessing and enhancement (like noise smoothing, contrast enhancement) (ii) enhancing object structure which includes thinning, skeletonization etc. (iii) segmentation (iv) quantitative description of the geometry of the objects or features.

The foundation of mathematical morphology is based on set theory. The image under study is treated as a set. The objective of morphological operation is to design non-linear operators which can analyze the shape of objects present in the image by probing or exploring the image with relatively smaller geometrical templates. The geometrical templates are commonly termed as *structuring elements*, which are also viewed as point sets. Morphological operations are defined in terms of set-theoretic operations between the two sets representing the image and the structuring element. The treatment of shapes in an image bu human visual system is neither fully subjective nor fully objective but something intermediate [31]. In mathematical morphology we have the flexibility to select the structuring elements with different size and shape according to our purpose. This selection is subjective in nature; while the operation on the shapes with this SE is purely objective. Hence, the SE acts as an interface between objective and subjective perception.

Morphological operations were developed originally for the binary images consisting of black and white pixels only. Basic morphological operations are erosion and dilation. The morphological transformation dilation combines two point sets X and B representing the object and the structuring element respectively using *Minkowski* set addition [107]

$$X \oplus B = \{y \in \xi^2 : y = x + b, x \in X \text{ and } b \in B\} \tag{2.15}$$

Likewise the operation *erosion* combines the sets X and B using *Minkowski* set subtraction [107] as

$$X \ominus B = \{y \in \xi^2 : y + b \in X \text{ for every } b \in B\} \tag{2.16}$$

Other operations like *opening, closing* are cascaded combination of these two operations.

$$X \circ B = (X \ominus B) \oplus B \tag{2.17}$$

$$X \bullet B = (X \oplus B) \ominus B \tag{2.18}$$

The concepts and operations of binary morphology were extended to gray-level images [149], [63] for obvious reasons. Different researchers have adopted different approaches in extending the definitions of the operations dilation, erosion to gray-level images. For example, Goutsias and Heijmans [57, 56, 58, 66] have treated the gray level image as complete lattice as an appropriate algebraic framework for a general theory of mathematical morphology. An operator $\epsilon : \mathcal{L} \rightarrow \mathcal{M}$ is called an erosion if it has the property of distributivity over the infima, i.e., if $\epsilon(\bigwedge_i X_i) = \bigwedge_i \epsilon(X_i)$, for all $\{X_i\}$ in $\mathcal{L}$. Here, $\mathcal{L}$ and $\mathcal{M}$ are two complete lattices. Likewise, an operator $\delta : \mathcal{M} \rightarrow \mathcal{L}$ is called a dilation if it distributes over suprema, i.e., $\delta(\bigvee_i Y_i) = \bigvee_i \delta(Y_i)$, for all $\{Y_i\}$ in $\mathcal{M}$. These two operators form an *adjunction* between the lattices $\mathcal{L}$ and $\mathcal{M}$ if

$$\delta(Y) \leq X \Longleftrightarrow Y \leq \epsilon(X), \quad X \in \mathcal{L},\ Y \in \mathcal{M}$$

The *function- and set-processing* (FSP) system[86] is widely used in morphology. FSP dilation and erosion of a gray-level image $g(r,c)$ by a two dimensional point set B are defined respectively as

$$(g \oplus B)(r,c) = max\{g(r-k,c-l)|(k,l) \in B\} \quad (2.19)$$

$$(g \ominus B)(r,c) = min\{g(r+k,c+l)|(k,l) \in B\} \quad (2.20)$$

Morphological opening and closing operations are defined as cascaded combination of dilation and erosion as given below

$$(g \circ B)(r,c) = ((g \ominus B) \oplus B)(r,c) \quad (2.21)$$

$$(g \bullet B)(r,c) = ((g \oplus B) \ominus B)(r,c) \quad (2.22)$$

In this thesis we would use the definitions and notations of FSP. A gray-level image may be viewed as a surface topography. The application of morphological opening to the gray level image using a structuring element (SE) causes clipping or truncation of its peaks narrower than the SE. In a similar way, closing causes the filling up of valleys narrower than the SE.

The *top-hat transformation* originally proposed in [98] provides an excellent tool for extracting bright (respectively, dark) features smaller than a given size from an uneven background. It relies on the fact that by gray-scale opening, one can remove from an image the brighter areas, i.e. features, that cannot hold the structuring element. Subtracting the opened image from the original one yields [using the following equation]

$$g^{top}(r,c) = g(r,c) - (g \circ B)(r,c) \quad (2.23)$$

$$g^{bot}(r,c) = (g \bullet B)(r,c) - g(r,c) \quad (2.24)$$

an image where the features that are narrower than the SE clearly stand out. Similar thing is true for closing operation also. That means using a *closing* in stead of an

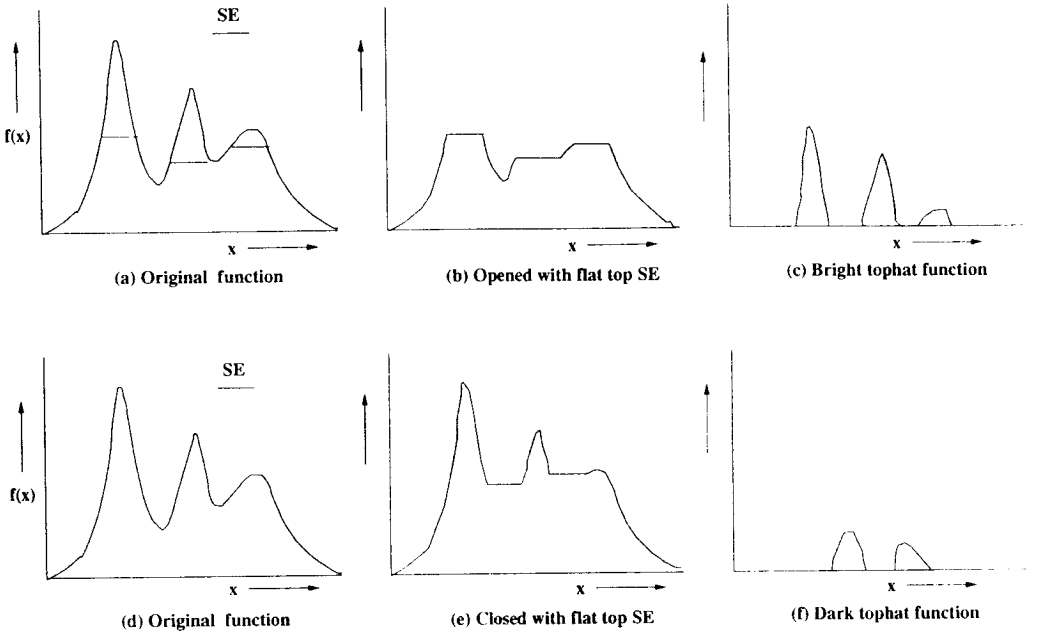

Figure 2.1: Illustrating bright and dark top-hat transformation through gray-level opening and closing with flat-top SE.

opening and subtracting the original image from the closed one helps us extract dark features from a brighter background. Let us call it a *dark top-hat* transformation as opposed to *bright top-hat* transformation in case of opening. Therefore, the bright top-hat transformation decomposes an image into two parts as given by

$$g(r,c) = \underbrace{(g \circ B)(r,c)}_{\text{part 1}} + \underbrace{[g(r,c) - (g \circ B)(r,c)]}_{\text{part 2}} \tag{2.25}$$

Fig 2.1 shows an example of bright top-hat transformation for an one-dimensional signal. Part 1 of equation (2.25) represents the *base image* with respect to $B(r,c)$ and the part 2 represents the *feature image* as it contains all the bright features of $g(r,c)$ that are smaller than B. This also holds good for dark top-hat transformation.

2.2.1 Multi-scale extension of morphological operations

Though the shape of the structuring element B plays important role in extracting and processing the shape-based features present in the image, it cannot however, treat objects of same shapes but of different sizes or scales. Thus, for a categorical processing of objects based on their shapes and sizes simultaneously we normally incorporate a second attribute to the structuring element that is its *scale*. A family of SE consisting of an SE and its higher order homothetics is capable of processing features based on shape as well as size. Such types of morphological operations where a structuring element of varying scale is utilized is termed as *multi-scale morphology* [142, 86]. Multi-scale opening and closing [155] are defined, respectively, as

$$(g \circ iB)(r,c) = ((g \ominus iB) \oplus iB)(r,c) \tag{2.26}$$

$$(g \bullet iB)(r,c) = ((g \oplus iB) \ominus iB)(r,c) \tag{2.27}$$

where B is a point set representing structuring element of a definite shape and i is an integer representing the scale factor of the convex structuring element. The ith homothetic of a convex SE B is obtained by dilating B recursively $i-1$ times with B itself as shown below.

$$iB = B \underbrace{\oplus B \oplus B \oplus \cdots \oplus B}_{i-1 \text{ times}} \tag{2.28}$$

Conventionally, $iB = \{(0,0)\}$ when $i = 0$. In a similar way, the multi-scale bright and dark top-hat transformations are defined as

$$g_i^{top}(r,c) = g(r,c) - (g \circ iB)(r,c) \tag{2.29}$$

$$g_i^{bot}(r,c) = (g \bullet iB)(r,c) - g(r,c) \tag{2.30}$$

2.2.2 Scale-space representation and multi-scale morphology

In [7] a complete classification is given of all image multi-scale transforms satisfying three categories of requirements: architectural requirement (i.e.,, locality, recursivity and causality), stability requirement (i.e., comparison principle) and morphological requirement (i.e., rotation and scale invariance). This classification yields a characterization of all models, which all are partial differential equation (PDE) [8]. This leads to underlying theory of level-set method and levelings [105]. Brockett and Maragos [24] also developed PDEs that model multi-scale morphological dilation, erosion, opening and closing by compact-support structuring elements. Boomgaard and Smeulders [22] have introduced a class of non-linear differential equations which are solved using morphological operations. There erosion and dilation act as morphological propagators propagating the original image into the "scale-space", much like the Gaussian convolution act as the propagator for the linear diffusion equation. The PDE formulation of a large class of morphological filters, the levelings and the openings/closings by reconstruction is given in [89]. Thus, multi-scale morphological operations distribute the entire image information among a set of filtered images. Now in doing so, the system of such operations should satisfy the properties like (i) *causality* and (ii) *edge localization* [82, 123, 14, 122]. By the term 'causality' we mean no regional extrema and, consequently, edge is introduced as the scale increases. The motive should be to distribute the total information and not to create new ones. The property 'edge localization' demands no drift of edge from its original position. The system is also expected to be *scale-calibrated*, i.e., the output image produced by an SE of a particular scale should strictly contain the features of that scale only. Apart from these, the directional or rotational invariance of the associated operation can be achieved using an isotropic SE.

The multi-scale opening produces flat regions by removing bright objects or its parts smaller than the SE. The properties: $g \circ B \leq g$ and $g \circ iB \geq g \circ jB$ for $i < j$ imply that

no new bright feature (or, in other words, regional maxima) is generated at higher scales due to opening. In case of multi-scale closing, no new dark feature (or, in other words, regional minima) is generated at higher scales. Secondly, SE leaves features wider than it unaffected. In one dimension, a translation invariant morphological operator preserves the slope of the signal [21]. In fact, a 'single-slope signal' - linear function - is left unchanged by any morphological operator with the exception of a translation of the function. However, in case of opening with a horizontal straight line segment, i.e. the SE, the edges are first drifted inward due to erosion which is followed by dilation that drifts the edges outward by the same amount. This avoids any displacement of edges. In the case of non-linear functions some peaks having width smaller than the length of the SE vanish completely. As a result, some edges may not be present in the opened image. However, other edges are present in their original positions. In the case of two or higher dimensions the situation is not, in general, so simple. Since we are dealing with image processing problems, our discussion is confined to two-dimensions only. The SE we use is a disk of certain radius. The edge localization problem does not arise only where the radius of curvature of the edges is not less than that of the SE or the features are not too narrow [31]. Otherwise, the features are either completely removed or pruned. In the latter case we see the edges are drifted inwards. A rectangle opened with a disk SE of diameter less than the smaller side of the rectangle is pruned at its corners [see fig 2.2(a) and (b)]. As a result, corner edges are drifted inward introducing an edge localization problem. Similar analysis holds for closing also in the complement sense.

Thus, we can at most say that conventional opening and closing satisfy the causality property partially. They also satisfy the property of scale-invariance. The main disadvantage of these conventional opening and closing is that they do not assure a perfect preservation of the edge information [135].

Bangham et. al. [14] suggested a scale-space operator, called M- and N-sieves, which

satisfies the properties mentioned above. However, this operator emphasizes on the size of the features only, and completely ignores its shape. However, it is possible to design morphological filters by reconstruction that satisfy these requirements and consider both shape and size of the features. Morphological multi-scale opening and closing by reconstruction [134, 77, 137] are two such filters.

2.2.3 Morphological opening and closing by reconstruction

The elementary geodesic dilation of size one (i.e. the smallest size in discrete domain) of the image g with respect to the reference image ρ is defined as the minimum between the dilation of the original function g with an SE X of size one and ρ, and is denoted by $\delta_X^1(g,\rho)$. Hence

$$\delta_X^1(g,\rho) = \min(g \oplus X, \rho) \tag{2.31}$$

Similarly, the elementary geodesic erosion of size one is defined as the maximum between the erosion of the original image g with a SE X of size one and a reference image ρ, and is denoted by $\epsilon_X^1(g,\rho)$. Hence

$$\epsilon_X^1(g,\rho) = \max(g \ominus X, \rho) \tag{2.32}$$

Now geodesic dilation and erosion of arbitrary size are obtained by iterating the elementary versions as defined below.

$$\delta_X^i(g,\rho) = \min(\delta_X^{(i-1)}(g,\rho) \oplus X, \rho) \tag{2.33}$$

$$\epsilon_X^i(g,\rho) = \max(\epsilon_X^{(i-1)}(g,\rho) \ominus X, \rho) \tag{2.34}$$

for $i = 1, 2, 3, \ldots$. Conceptually this may continue indefinitely, but for all practical purposes iteration is terminated at an integer n such that $\delta_X^n(g,\rho) = \delta_X^{(n-1)}(g,\rho)$ and, similarly, when $\epsilon_X^n(g,\rho) = \epsilon_X^{(n-1)}(g,\rho)$, because no change would occur after that. This

stable output is termed as *reconstruction by dilation* and is denoted by $\delta^{(rec)}(g, \rho)$, i.e.,

$$\delta^{(rec)}(g, \rho) = \delta_X^n(g, \rho)$$

Similarly we have *reconstruction by erosion* denoted by $\epsilon^{(rec)}(g, \rho)$, i.e.,

$$\epsilon^{(rec)}(g, \rho) = \epsilon_X^n(g, \rho)$$

Based on this operation, *opening by reconstruction of opening* or, simply, *opening by reconstruction* denoted by $g\bar{\circ}B$ may be defined as [160]

$$g\bar{\circ}B = \delta^{(rec)}(g \circ B, g) \tag{2.35}$$

Similarly, *closing by reconstruction* denoted by $g\bar{\bullet}B$ may be defined as

$$g\bar{\bullet}B = \epsilon^{(rec)}(g \bullet B, g) \tag{2.36}$$

Therefore, morphological opening by reconstruction in its first step eliminates bright features that do not fit within the SE B applying simple opening. However, in its second stage, it uses repetitive geodesic dilation to restore the contours of components that have not been completely removed by opening and a reconstruction is accomplished by the repetitive geodesic dilations using the original image g as a reference, i.e. choosing $\rho = g$. Similar analysis holds for 'closing by reconstruction' in case of dark features. As a result, problems like introduction of new edges and edge dis-localization do not arise in case of opening by reconstruction and closing by reconstruction. Hence, multi-scale system designed with these operators satisfy causality and edge localization properties. When these operators, i.e., open (close) by reconstruction, are used with multi-scale SEs, the output image should contain features of a scale as well as its higher scales. Difference between successive output will then contain features of a particular scale only. In essence, in the difference image the features which or, at least, a part of which contains the SE at that scale are

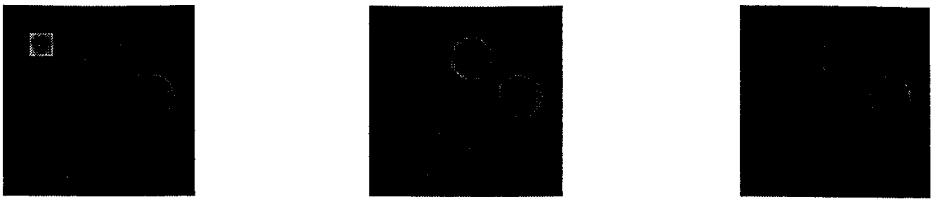

(a) (b) (c)

Figure 2.2: (a) Original image, (b) result of conventional opening of (a) using a disk SE, and (c) result of opening by reconstruction of (a) with same SE.

present completely and others are removed. Thus, the system can be termed as *scale calibrated.*

Therefore, the 'opening by reconstruction' can reconstruct the whole feature through geodesic dilation if at least a part of it can contain the SE. Thus the basic difference between conventional opening and opening by reconstruction is as follows: Conventional opening removes the parts of the bright features or objects that do not fit in the SE, whereas opening by reconstruction either removes the features completely or retains the whole of it. The situation is evident in the example shown in fig. 2.2 generated following Pizer [82]. Similar analysis holds for 'closing by reconstruction' in case of dark features. As a result, problems like introduction of new edges and edge displacement do not arise in case of opening by reconstruction and closing by reconstruction. Hence, a multi-scale system designed with these operators satisfies causality and edge localization properties. However, it should be noted that conventional opening and closing operations are far more efficient in removing noise than opening by reconstruction and closing by reconstruction respectively. Finally, it may be noted that a fast algorithm for opening (respectively closing) by reconstruction is available in [160].

2.2.4 Multi-scale morphological feature decomposition

The bright top-hat image resulting after filtering by a SE of size i contains all bright features of scale i and higher. The original image may be viewed as a combination of a base image and feature image obtained through top-hat transformation [98] as shown below.

$$g(r,c) = (g \circ iB)(r,c) + (g(r,c) - (g \circ iB)(r,c)) \tag{2.37}$$

Since the image contains bright features at different scales, the equation (2.37) may be extended as

$$\begin{aligned} g(r,c) &= (g \circ nB)(r,c) + ((g \circ (n-1)B)(r,c) - (g \circ nB)(r,c)) + \\ &\quad ((g \circ (n-2)B)(r,c) - (g \circ (n-1)B)(r,c)) + \ldots + \\ &\quad (g(r,c) - (g \circ B)(r,c)) \end{aligned} \tag{2.38}$$

$$\text{or, } \mathrm{g(r,c)} = (g \circ nB)(r,c) + F^o_B(r,c) + F^o_{2B}(r,c) + \ldots + F^o_{nB}(r,c) \tag{2.39}$$

where

$$F^o_{iB}(r,c) = (g \circ (i-1)B)(r,c) - (g \circ iB)(r,c) \tag{2.40}$$

The image also contains dark features at different scales, so that, we can write

$$g(r,c) = (g \bullet nB)(r,c) - F^c_B(r,c) - F^c_{2B}(r,c) - \ldots - F^c_{nB}(r,c) \tag{2.41}$$

where

$$F^c_{iB}(r,c) = (g \bullet iB)(r,c) - (g \bullet (i-1)B)(r,c) \tag{2.42}$$

Assigning equal priorities to both dark and bright features we combine equations (2.39) and (2.41) and get

$$g(r,c) = \frac{1}{2}\{(g \circ nB)(r,c) + (g \bullet nB)(r,c)\} + \underbrace{\frac{1}{2}\Sigma_1^n F^o_{iB}(r,c)}_{part1} - \underbrace{\frac{1}{2}\Sigma_1^n F^c_{iB}(r,c)}_{part2} \tag{2.43}$$

This is a multi-scale representation of the gray-level image in terms of its features at different scales. In a way this is a gray-scale morphology [149] version of discrete size transform and pattern spectrum [86].

2.2.5 Morphological Tower: An implementation of scale-space representation

The multi-scale representation of gray-level image adopted in this thesis for image processing and analysis is given in equation (2.43) obtained from [160], [98] and [86]. This is a special case of well-known granulometry using structural opening and closing by reconstruction with convex structuring elements of increasing scale. The said representation is implemented in this work as a stack of morphologically filtered images of same size and is referred in this work by *morphological tower* just to distinguish it from another well-known technique called *morphological pyramid* [97, 58]. A morphological tower may be constructed using different types of morphological operations like multi-scale opening, closing and top-hat transformation. This scale-space representation satisfies the criteria of multi-scale filtering. A morphological tower constructed by multi-scale opening (closing) is termed as *opening (closing) tower*. The scale parameter increases along the height of the tower. The i-th entry of an opening and a closing tower, are therefore, the images obtained by

$$(g \circ iB)(r,c) = ((g \ominus iB) \oplus iB)(r,c) \tag{2.44}$$

$$(g \bullet iB)(r,c) = ((g \oplus iB) \ominus iB)(r,c) \tag{2.45}$$

A morphological tower resembles an image pyramid in many aspects. A pyramid consists of a stack of images with progressively decreasing resolution and size of the image. A morphological tower on the other hand stacks the filtered images leaving the size of the image unchanged. Fig. 2.3 illustrates the structures of an image pyramid and a morphological tower. Morphological tower can be employed as a *tool* to solve some well known problems in image processing and computer vision. Some applications of morphological tower may be found in [117, 111, 113, 112, 116, 114, 30, 115, 118].

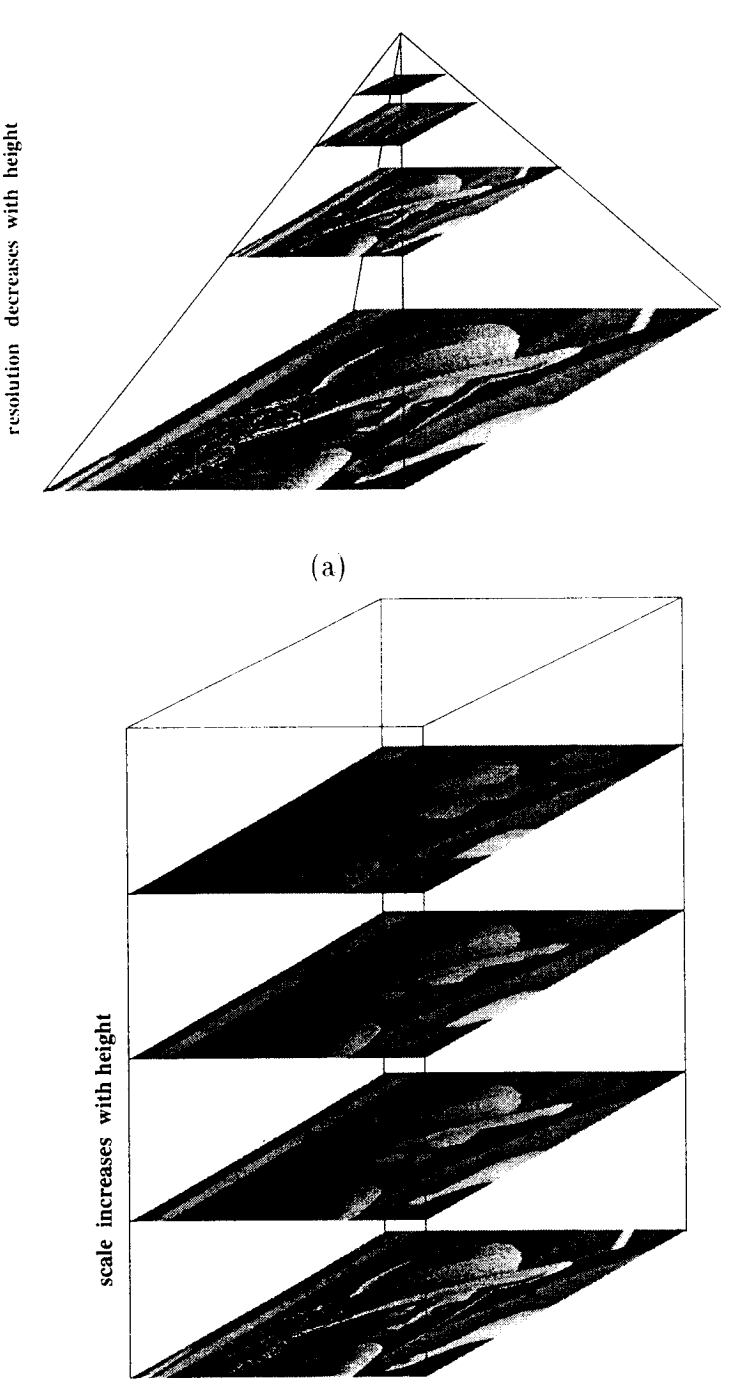

Figure 2.3: (a) image pyramid, (b) morphological tower corresponding to multi-scale opening

Morphological towers constructed with the images formed by taking the difference between two successive images in an opening tower or a closing tower are termed as *difference tower*. Thus the images in the difference towers corresponding to bright and dark features are obtained by

$$F^o_{iB}(r,c) = (g \circ (i-1)B)(r,c) - (g \circ iB)(r,c)$$
$$F^c_{iB}(r,c) = (g \circ (i-1)B)(r,c) - (g \circ iB)(r,c)$$

The images at two successive levels of an opening (resp. closing) tower correspond to two successive scales i and $i+1$. All features present in the i-th image of the opening (resp. closing) tower are smaller than or equal to the SE at scale i. The features of the $(i+1)$-th image of the opening (resp. closing) tower are similarly smaller than or equal to the SE at $(i+1)$. Therefore the i-th image in the difference tower contains all features which are of scale i. Thus a difference tower keeps the scale-specific bright and dark features in an increasing order of scale. In the applications employing morphological tower we will construct these difference towers wherever required.

All the applications employing morphological towers presented in this thesis comprise of three steps as described in fig. 2.4. In the first step we extract the scale-specific features (i.e., decomposition) and stack them in respective towers. In the next step the feature images at different scales are processed individually. However, this step is optional. In the third step the (processed) feature images of different scale are combined (i.e., recomposition) in a suitable way to meet the objectives of the processing. This basic philosophy or the general framework remains same for all the works performed and presented in this thesis.

It may be noted that the term *scale* should be defined in the context of the particular multi-scale filter used in the process. Here, in this thesis, we make use of isotropic flat top disk like structuring elements of increasing radii. The types of filtering used are opening, closing and top-hat transformation. The size of the SE (i.e., its radius)

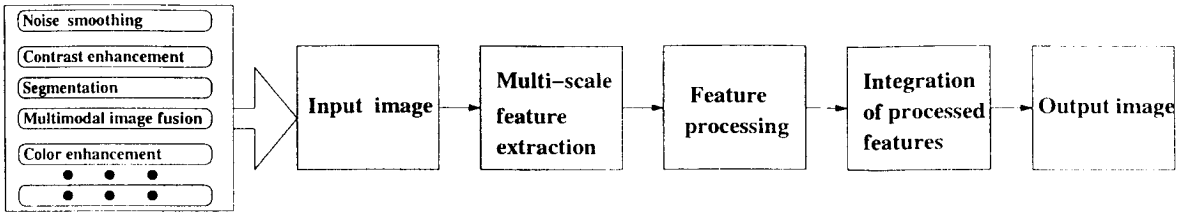

Figure 2.4: General scheme adopted in the thesis to solve the image processing problems employing the morphological tower.

is commensurate with scale. The image obtained using difference operation between the filtered images at two successive scales contains features of a particular scale.

As an example, in case of tower constructed employing opening, the *support* of all the objects in the image filtered at scale i are open with respect to binary opening with the disk of scale i. This is illustrated in fig 2.5. Fig. 2.5(a) shows a graylevel image of coins of different size. A set of circular disk structuring elements of increasing radii may be used to separate coins of different radii. Fig. 2.5(b-d) show the results of thresholding the image opened with disk SE at three successive scales. In fig 2.5(e-f) we have shown the difference between the images of fig. 2.5(b-d). The scale-specific features are detected in such a process.

All the image processing algorithms proposed in the subsequent chapters are based on the general strategy as described in fig. 2.4 employing the morphological tower.

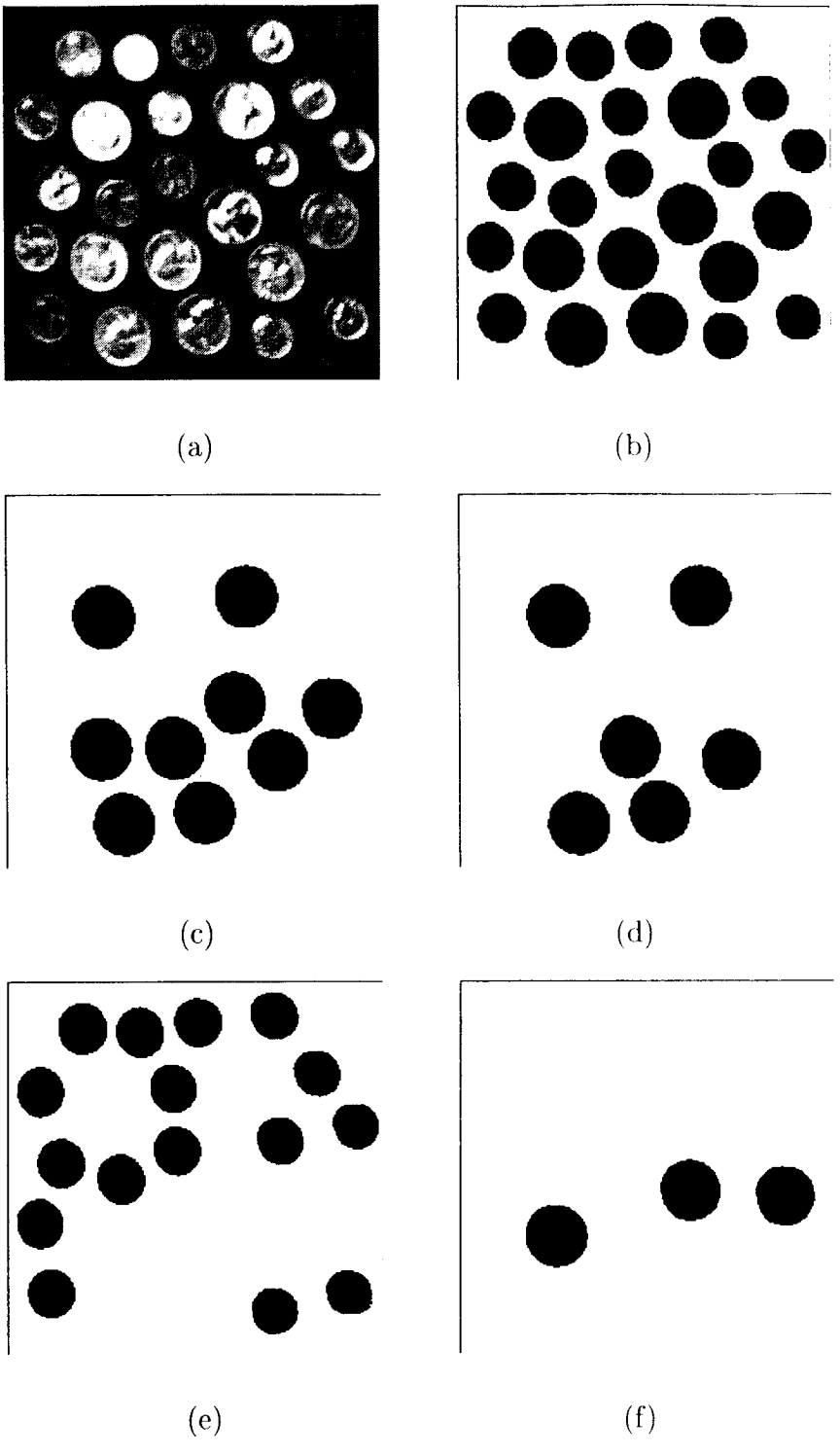

Figure 2.5: Features at different scales. (a) original image, (b) segmented image opened at scale i, (c) segmented image opened at scale $i + 1$, (d) segmented image opened at scale $i + 2$, (e) difference between images (b) and (c), and (f) difference between images (c) and (d).

Chapter 3

Graylevel image enhancement

3.1 Introduction

Image enhancement aims at improving the visual quality of the image and the enhanced image is generally more suitable than its original version for some specific applications. Here we consider only two types of enhancement techniques for gray-scale images: The noise smoothing and the contrast enhancement. As application of morphological tower, in the first part of this chapter we present an edge preserving noise smoothing technique for gray-scale images and a local contrast enhancement technique in the second part.

The presence of noise in an image is a common problem and irrespective of its type it degrades the quality of the image. Smoothing noise from the image may be assisted by *a priori* knowledge about the type of noise, the spatial location of occurrence and the extent of degradation. The result of executing a noise smoothing algorithm is generally accounted by the enhancement or visual clarity. The performance of the algorithm is measured by improvement in several performance metrics like *signal-to-noise* ratio,

mean busyness and *correct processing ratio*. Different methods of noise smoothing are cited in section 1.5.1. There exist different types of noise affecting the visual quality of images. In this work [117, 111] we have considered a few types of random noise which are known to degrade images in reality. For instance, the speckle noise is known to affect the satellite images. Also, different algorithms prove to be better in smoothing different types of noise. For example, the *mean filter* [131] performs better in smoothing additive and signal independent noise while *homomorphic filter* [72] performs better in smoothing multiplicative noise. In general, noise smoothing blurs the edge information and often removes the minute details. Hence, edge-preserving noise smoothing is the actual objective of this kind of enhancement. Poor contrast in gray-level images is quite a common problem. The clarity of such degraded images is improved using standard ad-hoc enhancement processes [131, 52, 72]. The aim of the local contrast enhancement is to improve the clarity of the image over its sub-regions. The works on the improvement of local contrast by different researchers are cited in section 1.5.2.

In this chapter, we present a multi-scale method which is able to smooth a wide variety of random noise leaving the desired edges undisturbed [117, 111] and extend the conventional theoretical concepts of local contrast enhancement in the light of multi-scale morphology [113, 112]. In case of noise smoothing we extract the bright and dark features of the noisy image at different scales using morphological filtering. The feature images so constructed are stacked in morphological towers. The construction of the smoothed image involves combining the feature images of the morphological towers with progressively less weights to small-scale features. The reason for assigning progressively less importance to feature images corresponding to smaller scales is due to the fact that the noise particles are predominant in smaller scales. In case of contrast enhancement our approach is almost identical, except the combination of feature images in the morphological tower assigns more weights to the small-scale features since the smaller features must look brighter or darker for better contrast.

That means in case of local contrast enhancement too the scale-specific bright and dark features are extracted in a similar way using multi-scale bright and dark top-hat transformation and are kept in respective morphological towers. The locally enhanced image is constructed by combining these scale-specific feature images with the original input image in a suitable way. The proposed schemes are first illustrated in one dimension for a better clarification. The proposed algorithm is executed on a set of raw images for testing its efficacy and the results are compared with those of other standard methods based on some standard performance measures for getting idea about its relative performance. A modification of the noise smoothing method considering noise statistics is also presented.

The organization of this chapter is as follows. In section 3.2 we have described the proposed method for noise smoothing. Section 3.2.1 describes the theoretical formulation of noise smoothing technique using multi-scale morphology under the framework of morphological tower. Section 3.2.2 gives a simplified illustration of the proposed formulation on one-dimensional function. Section 3.2.3 presents elaborately various steps of the implementation of the proposed algorithm. The experimental results and discussions are given in section 3.3. A modification of the proposed scheme considering the noise statistics is presented in section 3.4. The proposed method for contrast enhancement is presented in section 3.5. In section 3.5.1 we have presented the theoretical formulation of local contrast enhancement using multi-scale morphology. A simplified illustration of the proposed scheme is presented in section 3.5.2 by enhancing a function using the proposed scheme. Section 3.5.3 presents elaborately various steps of the implementational aspects of the proposed algorithm. Section 3.6 gives a discussion on the result and its comparison with that of other well-known techniques. Finally, concluding remarks for both the noise smoothing and the local contrast enhancement are given in section 3.7.

3.2 Proposed method for noise smoothing

3.2.1 Theoretical formulation

The noise smoothing technique using multi-scale morphology proposed here makes use of weighted averaging of a sequence of morphologically filtered images stacked in different morphological towers (see section 2.2.5) as depicted in fig. 3.3. In general, the presence of noise over a region in an image is manifested in terms of abrupt variation in the intensity as compared to the relatively smoother variation of the desired signal and consequently the edges. This key feature helps us discriminate noise from the image data. However, features of smaller size are affected more as compared to that of larger size. Hence, features of various sizes must be separated out prior to the application of any technique for reducing the noise.

Let us consider the multi-scale decomposition (using morphological filtering by reconstruction) of the image corrupted with noise in terms of its bright and dark feature leads to the following equation (please see section 2.2.4).

$$g(r,c) = \frac{1}{2}\{(g \circ nB)(r,c) + (g \bullet nB)(r,c)\} + \underbrace{\frac{1}{2}\Sigma_1^n F_{iB}^o(r,c)}_{part1} - \underbrace{\frac{1}{2}\Sigma_1^n F_{iB}^c(r,c)}_{part2} \quad (3.1)$$

Each $(F_{iB}^o)(r,c)$ in part1 of equation (3.1) represents the image consisting of bright features at scale i present in the input noisy image. Similarly, each $(F_{iB}^c)(r,c)$ in part2 represents the image consisting of dark features at scale i present in the input noisy image. In the reconstruction process equal emphasis is given to each of these feature images through equal weights (which is 1) as suggested by equation (3.1). However, according to our assumption the effect of noise is more in the lower scales. That means noise dominates in the feature images of equation (3.1). So, it is expected that the effect of noise in the reconstructed image gets reduced if we reconstruct the image by giving weights less than one to the feature images. With such views we can

modify equation (3.1) to obtain a smooth image as given below.

$$\tilde{g}(r,c) = \frac{1}{2}\{(g \circ nB)(r,c) + (g \bullet nB)(r,c)\} + \underbrace{\frac{1}{2}\Sigma_1^n k_i^o F_{iB}^o(r,c)}_{part1} - \underbrace{\frac{1}{2}\Sigma_1^n k_i^c F_{iB}^c(r,c)}_{part2} \quad (3.2)$$

where $0 \leq k_i^o < 1$ and $0 \leq k_i^c < 1$.

Now the problem is to estimate the values of the parameters k_i^os and k_i^cs. One simple way of estimating these parameters is to maximize some *goodness* criterion measured on the smooth image. The noise smoothing algorithm generally aims at reducing the abrupt changes and to maintain gradual changes (if any) in the intensity surface of the image. The abrupt changes in the intensity surface profile is manifested in terms of *edginess*. Based on this we consider the Euclidean norm of *Laplacian* of the smooth image as a suitable goodness criterion to be minimized. However, minimization of such type of objective function without any constraint usually leads to trivial solutions. So we need to incorporate certain constraint in the objective function to be minimized. Suppose, the image is corrupted by additive noise as given by

$$g(r,c) = f(r,c) + \eta(r,c)$$

In that case $\sum_r \sum_c (g(r,c) - \tilde{g}(r,c))^2 = \sum_r \sum_c \eta^2(r,c) = N(\mu_\eta^2 + \sigma_\eta^2)$ could be used as the constraint, where μ_η and σ_η are the mean and the variance of noise term, respectively and N is the number of pixels in the image. Thus the objective function to be minimized takes the form:

$$E(k_1^o, k_1^c, \ldots, k_n^o, k_n^c) = \sum_r \sum_c \{\nabla^2 \tilde{g}(r,c)\}^2 + \alpha\{\sum_r \sum_c (g(r,c) - \tilde{g}(r,c))^2 - N(\mu_\eta^2 + \sigma_\eta^2)\} \quad (3.3)$$

where, α is the *Lagrange multiplier*, and $0 \leq k_i^o < 1$ and $0 \leq k_i^c < 1$. Differentiating equation (3.3) with respect to the parameters k_1^o, k_1^c, ..., k_n^o and k_n^c and equating

them to zero, we get $2n$ number of simultaneous equations. Solving them we get

$$\begin{pmatrix} k_1^o \\ k_2^o \\ \cdots \\ \cdots \\ k_n^o \\ k_1^c \\ k_2^c \\ \cdots \\ \cdots \\ k_n^c \end{pmatrix} = 2\mathbf{X^{-1}} \begin{pmatrix} \alpha(\overline{gF_1^o}) - \alpha(\overline{AF_1^o}) - (\overline{L_A L_1^o}) \\ \alpha(\overline{gF_2^o}) - \alpha(\overline{AF_2^o}) - (\overline{L_A L_2^o}) \\ \cdots \\ \cdots \\ \alpha(\overline{gF_n^o}) - \alpha(\overline{AF_n^o}) - (\overline{L_A L_n^o}) \\ \alpha(\overline{gF_1^c}) - \alpha(\overline{AF_1^c}) - (\overline{L_A L_1^c}) \\ \alpha(\overline{gF_2^c}) - \alpha(\overline{AF_2^c}) - (\overline{L_A L_2^c}) \\ \cdots \\ \cdots \\ \alpha(\overline{gF_n^c}) - \alpha(\overline{AF_n^c}) - (\overline{L_A L_n^c}) \end{pmatrix} \tag{3.4}$$

where

$$\begin{pmatrix} (\overline{L_1^o L_1^o} + \alpha\overline{F_1^o F_1^o}) & (\overline{L_1^o L_2^o} + \alpha\overline{F_1^o F_2^o}) & \cdots & (\overline{L_1^o L_n^o} + \alpha\overline{F_1^o F_n^o}) & -(\overline{L_1^o L_1^c} + \alpha\overline{F_1^o F_1^c}) & -(\overline{L_1^o L_2^c} + \alpha\overline{F_1^o F_2^c}) & \cdots & -(\overline{L_1^o L_n^c} + \alpha\overline{F_1^o F_n^c}) \\ (\overline{L_2^o L_1^o} + \alpha\overline{F_2^o F_1^o}) & (\overline{L_2^o L_2^o} + \alpha\overline{F_2^o F_2^o}) & \cdots & (\overline{L_2^o L_n^o} + \alpha\overline{F_2^o F_n^o}) & -(\overline{L_2^o L_1^c} + \alpha\overline{F_2^o F_1^c}) & -(\overline{L_2^o L_2^c} + \alpha\overline{F_2^o F_2^c}) & \cdots & -(\overline{L_2^o L_n^c} + \alpha\overline{F_2^o F_n^c}) \\ \cdots & \cdots & \cdots & \cdots & \cdots & \cdots & \cdots & \cdots \\ \cdots & \cdots & \cdots & \cdots & \cdots & \cdots & \cdots & \cdots \\ (\overline{L_n^o L_1^o} + \alpha\overline{F_n^o F_1^o}) & (\overline{L_n^o L_2^o} + \alpha\overline{F_n^o F_2^o}) & \cdots & (\overline{L_n^o L_n^o} + \alpha\overline{F_n^o F_n^o}) & -(\overline{L_n^o L_1^c} + \alpha\overline{F_n^o F_1^c}) & -(\overline{L_n^o L_2^c} + \alpha\overline{F_n^o F_2^c}) & \cdots & -(\overline{L_n^o L_n^c} + \alpha\overline{F_n^o F_n^c}) \\ (\overline{L_1^c L_1^o} + \alpha\overline{F_1^c F_1^o}) & (\overline{L_1^c L_2^o} + \alpha\overline{F_1^c F_2^o}) & \cdots & (\overline{L_1^c L_n^o} + \alpha\overline{F_1^c F_n^o}) & -(\overline{L_1^c L_1^d} + \alpha\overline{F_1^c F_1^d}) & -(\overline{L_1^c L_2^d} + \alpha\overline{F_1^c F_2^c}) & \cdots & -(\overline{L_1^c L_n^c} + \alpha\overline{F_1^c F_n^c}) \\ (\overline{L_2^c L_1^o} + \alpha\overline{F_2^c F_1^o}) & (\overline{L_2^c L_2^o} + \alpha\overline{F_2^c F_2^o}) & \cdots & (\overline{L_2^c L_n^o} + \alpha\overline{F_2^c F_n^o}) & -(\overline{L_2^c L_1^c} + \alpha\overline{F_2^c F_1^c}) & -(\overline{L_2^c L_2^c} + \alpha\overline{F_2^c F_2^c}) & \cdots & -(\overline{L_2^c L_n^c} + \alpha\overline{F_2^c F_n^c}) \\ \cdots & \cdots & \cdots & \cdots & \cdots & \cdots & \cdots & \cdots \\ \cdots & \cdots & \cdots & \cdots & \cdots & \cdots & \cdots & \cdots \\ (\overline{L_n^c L_1^o} + \alpha\overline{F_n^c F_1^o}) & (\overline{L_n^c L_2^o} + \alpha\overline{F_n^c F_2^o}) & \cdots & (\overline{L_n^c L_n^o} + \alpha\overline{F_n^c F_n^o}) & -(\overline{L_n^c L_1^c} + \alpha\overline{F_n^c F_1^c}) & -(\overline{L_n^c L_2^c} + \alpha\overline{F_n^c F_2^c}) & \cdots & -(\overline{L_n^c L_n^c} + \alpha\overline{F_n^c F_n^c}) \end{pmatrix}$$

and

$$
\begin{aligned}
A(r,c) &= \tfrac{1}{2}\{(g \circ nB)(r,c) + (g \bullet nB)(r,c)\} \\
L_i^o(r,c) &= \bigtriangledown^2 F_i^o(r,c) \\
L_i^c(r,c) &= \bigtriangledown^2 F_i^c(r,c) \\
L_A(r,c) &= \bigtriangledown^2 A(r,c) \\
\overline{L_i^o L_j^c} &= \tfrac{1}{(ht*wd)} \Sigma_{r=1}^{ht} \Sigma_{c=1}^{wd} L_i^o(r,c) L_i^c(r,c) \\
\overline{F_i^o F_j^c} &= \tfrac{1}{(ht*wd)} \Sigma_{r=1}^{ht} \Sigma_{c=1}^{wd} F_i^o(r,c) F_i^c(r,c) \\
\overline{AF_j^o} &= \tfrac{1}{(ht*wd)} \Sigma_{r=1}^{ht} \Sigma_{c=1}^{wd} AF_i^o(r,c) \\
\overline{AF_j^c} &= \tfrac{1}{(ht*wd)} \Sigma_{r=1}^{ht} \Sigma_{c=1}^{wd} AF_i^c(r,c) \\
\overline{gF_j^o} &= \tfrac{1}{(ht*wd)} \Sigma_{r=1}^{ht} \Sigma_{c=1}^{wd} gF_i^o(r,c) \\
\overline{gF_j^c} &= \tfrac{1}{(ht*wd)} \Sigma_{r=1}^{ht} \Sigma_{c=1}^{wd} gF_i^c(r,c) \\
\overline{L_A L_j^o} &= \tfrac{1}{(ht*wd)} \Sigma_{r=1}^{ht} \Sigma_{c=1}^{wd} L_A(r,c) L_i^o(r,c) \quad \text{and} \\
\overline{L_A L_j^c} &= \tfrac{1}{(ht*wd)} \Sigma_{r=1}^{ht} \Sigma_{c=1}^{wd} L_A(r,c) L_i^c(r,c)
\end{aligned}
$$

Value of α is chosen iteratively so as to satisfy the given constraint [131, 53, 29]. The experiment has been carried out on quite a few images corrupted with various types of noise; however, for the sake of presentation, we have taken an example image along with its Gaussian noise corrupted version. Figure 3.1(a) shows the image corrupted with Gaussian noise and fig. 3.1(b-e) show the noise grains present in it at different scales. The values estimated are shown in Table 3.1. It is observed that the parameter values follow an increasing order, i.e., $k_1^o \leq k_2^o \leq k_3^o \ldots \leq k_n^o$ and $k_1^c \leq k_2^c \leq k_3^c \ldots \leq k_n^c$, which conform with the observation (please see table 3.1), that introduction of random noise, in general, generates perturbation at lower scales [155].

However, estimation of the parameters incurs a huge computational cost. To avoid such huge computational cost and also to use fixed point arithmetic operations (for further speed up of the algorithm), we have chosen $k_n^o = k_n^c = \frac{1}{2}$, $k_{i-1}^o = \frac{1}{2} k_i^o$ and $k_{i-1}^c = \frac{1}{2} k_i^c$ for $i = n, n-1, \ldots$. However, these weights are set heuristically guided by the experimental results. Therefore this algorithm is suitable for a class of images

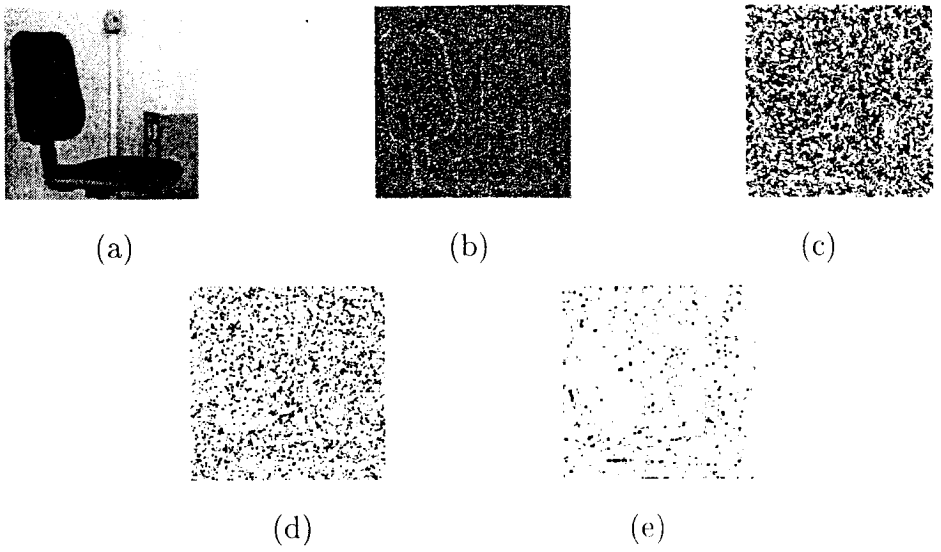

Figure 3.1: Illustrates Gaussian noise grains at different scales: (a) Noisy image (b) scale 1, (c) scale 2, (d) scale 3, and (e) scale 4.

that satisfy the monotonies of the noise contents with scale. The efficacy of this selection is established in section 3.3. This selection leads to

$$\begin{aligned}\tilde{g}(r,c) &= \frac{1}{2}\{(g \circ nB)(r,c) + (g \bullet nB)(r,c)\} \\ &\quad + \frac{1}{2}[\frac{1}{2^n}F_1^o(r,c) + \frac{1}{2^{n-1}}F_2^o(r,c) + \ldots \frac{1}{2}F_n^o(r,c)] \\ &\quad - \frac{1}{2}[\frac{1}{2^n}F_1^c(r,c) + \frac{1}{2^{n-1}}F_2^c(r,c) + \ldots \frac{1}{2}F_n^c(r,c)]\end{aligned} \tag{3.5}$$

$$\begin{aligned}&= \frac{1}{2}\{(g \circ nB)(r,c) + (g \bullet nB)(r,c)\} \\ &\quad + \frac{1}{2}\frac{\frac{\frac{\frac{1}{2}F_1^o(r,c)+F_2^o(r,c)}{2}+F_3^o(r,c)}{2}+F_4^o(r,c)}{2}+\ldots \\ &\quad\quad \vdots \\ &\quad\quad \frac{}{2} + F_n^o(r,c) \\ &\quad\quad \frac{}{2} \\ &\quad - \frac{1}{2}\frac{\frac{\frac{\frac{1}{2}F_1^c(r,c)+F_2^c(r,c)}{2}+F_3^c(r,c)}{2}+F_4^c(r,c)}{2}+\ldots \\ &\quad\quad \vdots \\ &\quad\quad \frac{}{2} + F_n^c(r,c) \\ &\quad\quad \frac{}{2}\end{aligned} \tag{3.6}$$

Table 3.1: An example of estimated values of the parameters.

Scale	Type of feature			
	bright feature		dark feature	
	parameter	value	parameter	value
1	k_1^b	0.003480940	k_1^d	0.007203650
2	k_2^b	0.012613741	k_2^d	0.018714545
3	k_3^b	0.065167400	k_3^d	0.039894422
4	k_4^b	0.072803162	k_4^d	0.058386658

Let us define

$$g^o_{av_1}(r,c) = \frac{1}{2}\{F^o_B(r,c)\} \tag{3.7}$$

$$g^o_{av_i}(r,c) = \frac{1}{2}\{g^o_{av_{(i-1)}}(r,c) + F^o_{iB}(r,c)\} \tag{3.8}$$

$$g^c_{av_1}(r,c) = \frac{1}{2}\{F^c_B(r,c)\} \tag{3.9}$$

$$g^c_{av_i}(r,c) = \frac{1}{2}\{g^c_{av_{(i-1)}}(r,c) + F^c_{iB}(r,c)\} \text{ and} \tag{3.10}$$

$$\bar{g}(r,c) = \frac{1}{2}\{(g \circ nB)(r,c) + (g \bullet nB)(r,c)\} \tag{3.11}$$

Then equation (3.6) can be rewritten as

$$\tilde{g}(r,c) = \bar{g}(r,c) + \frac{1}{2}g^o_{av_n}(r,c) - \frac{1}{2}g^c_{av_n}(r,c) \tag{3.12}$$

Equation (3.12) can be implemented on morphological towers as described elaborately in the next subsection.

In the proposed scheme the scale specific feature images are extracted using top-hat transformation based on multi-scale opening by reconstruction and closing by reconstruction. There exist other methods for extracting scale specific features from images which use median filter [12], stack filter [91], alternate sequential filter [158], [137].

M- and N-sieves [14], [64]. Second, we have reconstructed the image from the decomposed ones by their linear combination. However, non-linear combinations are also employed for the purpose; for example, Toet [155] used max operator to reconstruct the image from morphological tree.

3.2.2 A simple illustration in one-dimension

A simplified illustration of the proposed scheme applied to one-dimensional signal is shown in fig.3.2 for easy understanding. The function $f(t)$ has salient features manifested as *crests* and *troughs* of different height (or depth) and width located at different positions. The noise in the function is manifested in terms of the narrow peaks and troughs at different positions. Our objective is to smooth the noise of the function $g(t)$. The line segment L of unit length and its higher order dilates kL (where $k = 1, 2, 3$) are used as structuring elements (SE) for extracting the salient features at different scales from the function as described below.

- The opening operation with the SE kL removes the crests which are narrower than the width k while the closing operation fills up the troughs narrower than the width k .

- The function $F_k^o(t) = (g \circ (k-1)L)(t) - (g \circ kL)(t)$ contains only the crests of width smaller than k but larger than $(k-1)$ and the function $F_k^c(t) = (g \bullet kL)(t) - (g \bullet (k-1)L)(t)$ contains only the troughs of width smaller than k but larger than $(k-1)$. Proceeding in this way we construct the function $F_1^o(t), F_2^o(t), F_3^o(t)$ and $F_1^c(t), F_2^c(t), F_3^c(t)$ (see fig.3.2).

- We take recursive averaging of the functions obtained in the previous steps. We first construct the function $g_{av1}^o(t) = \frac{1}{2}[F_1^o(t)]$, then the functions $g_{av2}^o(t) =$

$\frac{1}{2}[g^o_{av1} + F^o_2(t)]$ and $g^o_{av3}(t) = \frac{1}{2}[g^o_{av2} + F^o_3(t)]$, respectively. In a similar way the function $g^c_{av3}(t)$ is constructed.

- The function $\bar{g}(t)$ is obtained by averaging $(g \circ 3L)(t)$ and $(g \bullet 3L)(t)$.
- The smoothed function is then formed by combining the functions $\bar{g}(t)$, $g^o_{av3}(t)$ and $g^c_{av3}(t)$ as shown below:

$$\tilde{g}(t) = \bar{g}(t) + \frac{1}{2}g^o_{av3}(t) - \frac{1}{2}g^c_{av3}(t) \tag{3.13}$$

Comparing $\tilde{g}(t)$ with $f(t)$ at each sample point t it is readily seen that the height (depth) of the crests (troughs) have decreased but disproportionately. The change in height is more for crests of narrower width. This is true for crests also. This would not be possible using mean filtering. The smooth function is found to be less affected by noise spikes without any noticeable change in sharpness and location of valid edges. The scheme explained for this one-dimensional case may as well be extended to two-dimension as described below.

3.2.3 Implementation

The implementation of equation (3.12) describing feature based noise smoothing scheme involves construction of a number of morphological towers.

Construction of Morphological Towers

The noisy image to be smoothed is made to undergo a sequence of gray-scale morphological opening by reconstruction with a disc structuring element and its higher order homothetics. The resulting sequence of images is kept in a stack called the *opening* tower as shown in fig 3.3. An identical tower, called *closing* tower, is constructed with

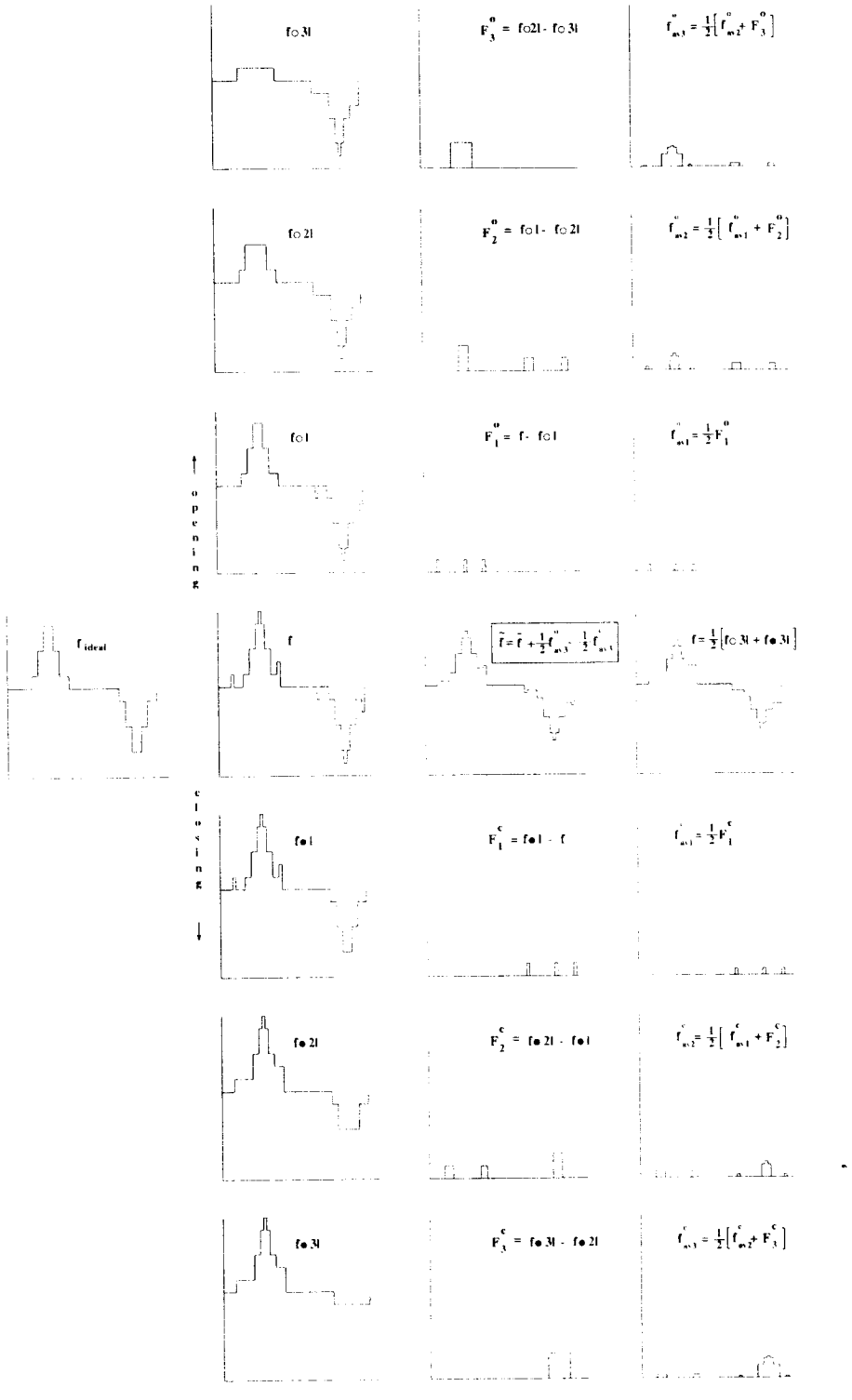

Figure 3.2: Multi-scale morphological noise smoothing of a function

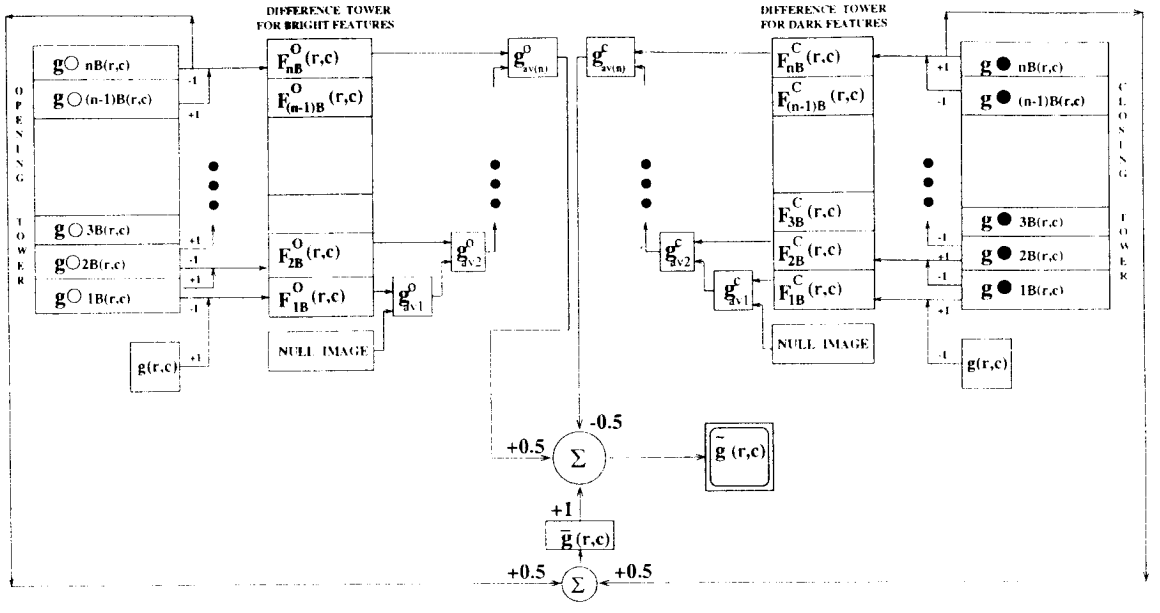

Figure 3.3: Noise smoothing scheme using morphological towers

the sequence of the images resulting from multi-scale closing by reconstruction of the input noisy image. Therefore, the i-th entry in the opening (closing) tower contains the image opened(closed) with the structuring element iB as given below.

$$(g \circ iB)(r,c) = ((g \ominus iB) \oplus iB)(r,c) \tag{3.14}$$

$$(g \bullet iB)(r,c) = ((g \oplus iB) \ominus iB)(r,c) \tag{3.15}$$

for $i = 1, 2, \ldots, n$.

Construction of Difference towers

We construct two difference towers for opening and closing are constructed by carrying out difference operations between all successive pairs of images resulting after morphological opening (closing) operations. Fig. 3.3 shows two such *difference towers*. Thus the $i-th$ layer of the difference tower corresponding to bright and dark

features contain the images obtained by following operations.

$$F^o_{iB}(r,c) = (g \circ (i-1)B)(r,c) - (g \circ iB)(r,c) \quad (3.16)$$

$$F^c_{iB}(r,c) = (g \bullet iB)(r,c) - (g \bullet (i-1)B)(r,c) \quad (3.17)$$

for $i = 1, 2, \ldots, n$.

Construction of smooth image

- A recursive averaging of the images stacked in difference tower corresponding to opening (closing) is carried out. We start with a null image and select the image at the lowest layer of the difference tower and form another image by averaging them. Then we construct another image by taking the average of the resulting image and the image in the next higher layer of the corresponding difference tower. This is continued until the top of the tower is reached. This is described mathematically by equations (3.7-3.10).

- The average of the images resulting after opening and closing of the input image by the largest homothetic of the SE is also computed as described by equation (3.11). Note that the average, everywhere, denotes pixel-wise average of images.

- Finally, the smooth image is obtained by combining three images as given by

$$\tilde{g}(r,c) = \bar{g}(r,c) + \frac{1}{2} g^o_{av_n}(r,c) - \frac{1}{2} g^c_{av_n}(r,c) \quad (3.18)$$

  The '+' and '-' operations are applied on corresponding pixels of three different images.

The algorithm for multi-scale feature extraction is as given below.

Pass-1 : Multi-scale feature extraction

Procedure *Extract_multi-scale_features()*

input: $g_{in}[][]$; /* the input noisy image */

output: open_tower, close_tower,bright_top_tower, dark_top_tower;

/* towers of filtered images */

output: bright_top_tower, dark_top_tower: /* towers of filtered images */

constant: $MAXSCALE$; /* upper bound of scale factor */

var: $g_{op}[][]$, $g_{cl}[][]$, $g_{temp1}[][]$, $g_{temp2}[][]$, $g_{temp3}[][]$; /* intermediate images */

integer: i;

$i \leftarrow 1$;

begin

repeat

$g_{op} \leftarrow open(g_{in}, iB)$;

$g_{cl} \leftarrow close(g_{in}, iB)$;

$insert\_in\_tower(g_{op}, open\_tower, i)$;

$insert\_in\_tower(g_{cl}, close\_tower, i)$;

$increase\ i$;

until $i > MAXSCALE$;

end begin

$i \leftarrow 1$;

begin

repeat

$g_{temp1} \leftarrow get\_image\_from(open\_tower, i)$;

$g_{temp2} \leftarrow get\_image\_from(open\_tower, i + 1)$;

$g_{temp3} \leftarrow g_{temp1}$ - g_{temp2};

$insert\_in\_tower(g_{temp3}, bright\_top\_tower)$;

$g_{temp1} \leftarrow get\_image\_from(close\_tower, i)$;

if($i == MAXSCALE$) then

$g_{temp1} \leftarrow get\_image(open\_tower, i)$;

$g_{temp2} \leftarrow get\_image(open\_tower, i)$;

$g^{op}_{min} \leftarrow min(g_{temp1}, g_{temp2}$;

$g_{temp1} \leftarrow get\_image(close\_tower, i)$;

$g_{temp2} \leftarrow get\_image(close\_tower, i)$;

$g^{cl}_{max} \leftarrow max(g_{temp1}, g_{temp2})$;

$g_{baseimg} \leftarrow avg(g^{op}_{min}, g^{cl}_{max})$;

endif

$increase\ i$;

until $i > MAXSCALE$;

end begin

$g_{smooth} \leftarrow g_{baseimg} + 0.5 * g_{temp2} - 0.5 * g_{temp4}$;

end Procedure

3.3 Experimental results and Discussion

The proposed algorithm has been tested on several images. However, the results are shown here for a single image corrupted with different kinds of noise as shown in fig. (3.4 [1(a)-7(a)]). Various kinds of noise considered in the experiment include *exponential, Gaussian, Poisson, Rayleigh, shot, uniform* and *speckle* noise - the details of which are listed in table 3.2. For generating noise we made use of image processing software *Khoros*. The results of proposed algorithm are shown in fig. 3.4[1(b)-7(b)]. We have compared our results with those of *median filter*(see fig. 3.4[1(c)-7(c)]), *Crimmins filter* [35] (see fig. 3.4[1(d)-7(d)]), and *Anisotropic diffusion smoothing* [123, 164] (see fig. 3.4[1(e)-7(e)]). In the experiment we have chosen $n = 6$ for our proposed

if($i == MAXSCALE$) then

$g_{temp1} \leftarrow get\_image(open\_tower, i)$;

$g_{temp2} \leftarrow get\_image(open\_tower, i)$;

$g^{op}_{min} \leftarrow min(g_{temp1}, g_{temp2}$;

$g_{temp1} \leftarrow get\_image(close\_tower, i)$;

$g_{temp2} \leftarrow get\_image(close\_tower, i)$;

$g^{cl}_{max} \leftarrow max(g_{temp1}, g_{temp2})$;

$g_{baseimg} \leftarrow avg(g^{op}_{min}, g^{cl}_{max})$;

endif

$increase\ i$;

until $i > MAXSCALE$;

end begin

$g_{smooth} \leftarrow g_{baseimg} + 0.5 * g_{temp2} - 0.5 * g_{temp4}$;

end Procedure

3.3 Experimental results and Discussion

The proposed algorithm has been tested on several images. However, the results are shown here for a single image corrupted with different kinds of noise as shown in fig. (3.4 [1(a)-7(a)]). Various kinds of noise considered in the experiment include *exponential, Gaussian, Poisson, Rayleigh, shot, uniform* and *speckle* noise - the details of which are listed in table 3.2. For generating noise we made use of image processing software *Khoros*. The results of proposed algorithm are shown in fig. 3.4[1(b)-7(b)]. We have compared our results with those of *median filter*(see fig. 3.4[1(c)-7(c)]), *Crimmins filter* [35] (see fig. 3.4[1(d)-7(d)]), and *Anisotropic diffusion smoothing* [123, 164] (see fig. 3.4[1(e)-7(e)]). In the experiment we have chosen $n = 6$ for our proposed

Table 3.2: Different types of noise and their parameters used in the experiment

Fig. No.	Type of noise	Parameter attributes	Values of the parameters	Whether additive or multiplicative
1a	Exponential	Variance	255.0	Additive
2a	Gaussian	Mean	0.0	Additive
		Variance	255.0	
3a	Poisson	Amount of time	2000	Additive
		Variance	75.0	
4a	Rayleigh	Variance	255.0	Additive
5a	Shot	Percentage of spikes	70	Additive
		Real value of spike	255.0	
		Imaginary value of spike	0.0	
6a	Uniform	Minimum value	-50.0	Additive
		Maximum value	+50.0	
7a	Speckle	Mean	1.0	Multiplicative
		Standard deviation	+0.28	

method. For median filter and Crimmins filter the mask size used is 7×7. For anisotropic diffusion smoothing the value of δt, λ and number of iterations are taken as 0.5, 1.0 and 20 respectively. The values of all these parameters are chosen to obtain visually optimum results.

Qualitative evaluation (by human observer) reveals that median filter has more or less blurred the thin features of the image. Results of Crimmins filter are better than those of median filter and it has proved to be the best for smoothing speckle noise. Results of the proposed method show relatively less blurring of thin features

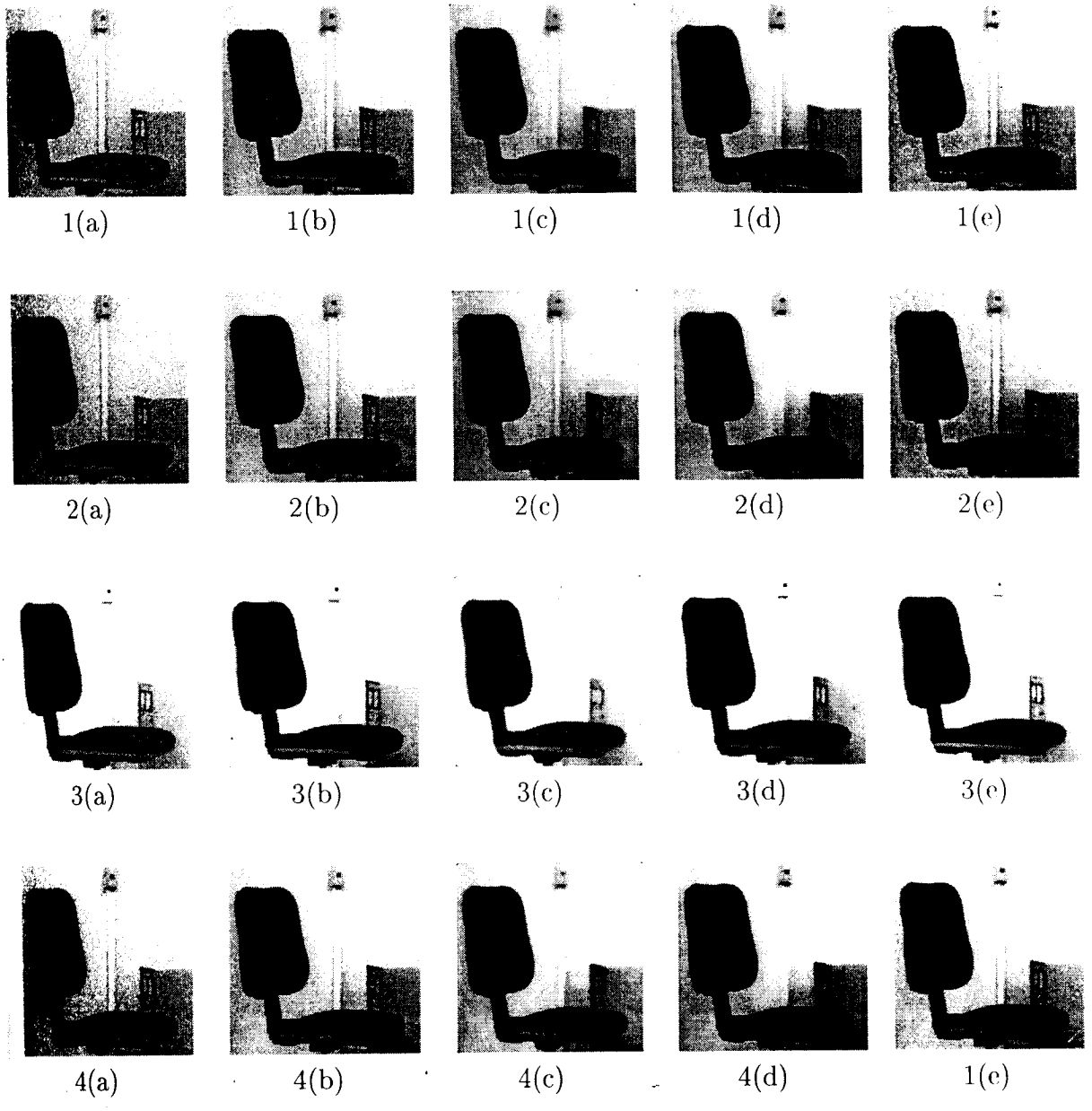

Figure 3.4: (a) Original noisy image, (b) result of proposed multi-scale morphological noise removal filtering, (c) result of median filtering, (d) result of *Crimmins* algorithm, and (e) results of anisotropic diffusion smoothing for (1) *exponential* noise, (2) *Gaussian* noise, (3) *Poisson* noise, (4) *Rayleigh* noise, (5) *shot* noise, (6) *uniform* noise, and (7) *speckle* noise.

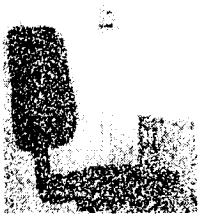

5(a)

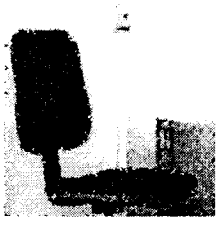

5(b)

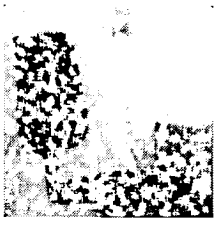

5(c)

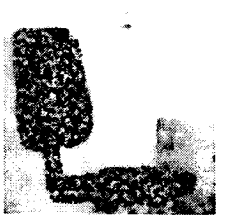

5(d)

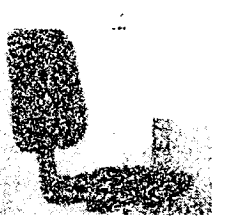

5(e)

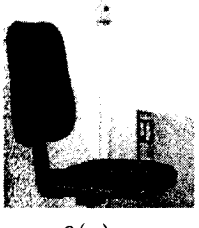

6(a)

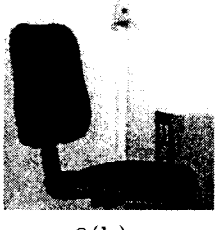

6(b)

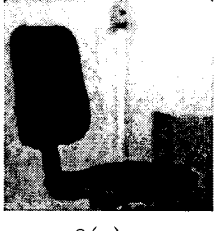

6(c)

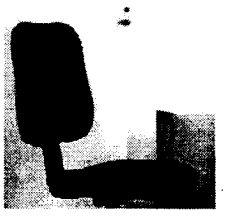

6(d)

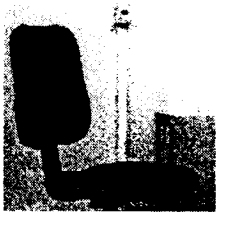

6(e)

7(a)

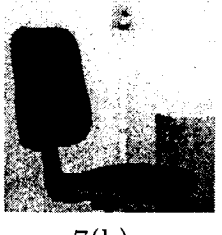

7(b)

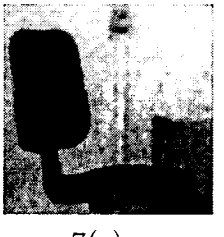

7(c)

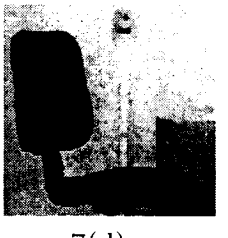

7(d)

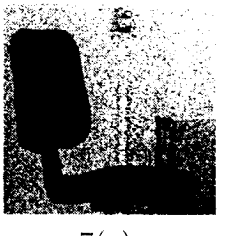

7(e)

Figure 3.4: Continued

with appreciable noise cleaning and it has greatly outperformed other methods in smoothing shot noise. However, the proposed method has higher space complexity as compared to others. Considering overall performance it can be said in essence, that the proposed multi-scale morphological technique is a good edge-preserving smoothing technique.

3.3.1 Performance analysis

For quantitative comparison of performances of the methods referred here we have studied the followings measures.

Signal-to-Noise Ratio

Suppose $I(r,c)$ and $I_n(r,c)$ denote noise-free and noisy image of the same scene. Signal-to-noise ratio (SNR) is defined as the ratio of signal power to the noise power as given below.

$$SNR = \frac{\Sigma_r \Sigma_c I^2(r,c)}{\Sigma_r \Sigma_c \{I(r,c) - I_n(r,c)\}^2} \tag{3.19}$$

The more the value of SNR the better is the noise smoothing method. It may be measured as ratio or in terms of dB. In table 3.3 we have presented SNR values (as ratio) of the smooth images resulting from various methods. We also have ranked the methods depending on the SNR values. Higher relative score is assigned to better method. From the table 3.3 it is evident that the total score of our proposed method is the second highest among all other methods. In most of the cases the SNR value is either the highest or the second highest.

Table 3.3: Signal-to-noise ratio (SNR) for different noise removal schemes

ise	Input	Signal-to-noise ratio and scores							
e	SNR	MMS		MF		CA		ADS	
		SNR	score	SNR	score	SNR	score	SNR	score
p	60.695696	107.092369	3	128.374554	4	84.032957	1	101.385678	2
	110.967612	521.394035	2	359.873484	1	554.378836	3	664.503600	4
	6.323838	12.321112	1	13.584419	2	14.199405	4	13.864437	3
	25.231925	30.637288	3	29.966759	2	26.847579	1	30.924575	4
	2.597885	5.025113	4	2.479764	1	3.920223	3	3.184999	2
	35.734041	249.829078	3	178.546900	2	390.640388	4	131.178951	1
	17.507818	101.459861	3	89.792234	2	106.833882	4	30.123955	1
TAL			19		14		20		17

Noise type: Exp: Exponential noise. Gus: Gaussian noise, Pos: Poisson noise, Ral: Rayleigh noise, Sht: Shot noise, Uni: Uniform noise, Spk: Speckle noise MMS: Multi-scale Morphological Smoothing, MF: Median Filtering, CA: Crimmins Algorithm, ADS: Anisotropic Diffusion Smoothing

Table 3.4: Deviation in mean busyness value (DMB) for different noise removal schemes

Type of Noise	Deviation in mean busyness value and score of the scheme								
	NI	MMS		MF		CA		ADS	
	DMB	DMB	score	DMB	score	DMB	score	DMB	score
Exp	10.921769	1.776302	1	0.061684	4	-0.663406	3	1.085721	2
Gus	14.009873	2.513388	1	0.228851	4	-0.670080	3	1.416486	2
Pos	3.561615	0.076848	4	-0.519846	2	-0.869204	1	-0.343052	3
Ral	12.423284	1.810181	1	0.213318	4	-0.672295	3	1.106729	2
Sht	56.100977	-0.485336	4	2.166444	3	15.512188	2	35.877724	1
Uni	26.590066	3.531104	2	1.396079	3	-0.540330	4	7.273403	1
Spk	31.357986	5.062269	2	1.696948	3	0.053672	4	14.632311	1
TOTAL			15		23		20		12

Type of Noise: Exp: Exponential noise, Gus: Gaussian noise, Pos: Poisson noise, Ral: Rayleigh noise Sht: Shot noise, Uni: Uniform noise, Spk: Speckle noise NI : Noisy Image, MMS: Multi-scale Morphological Smoothing, MF: Median Filtering, CA: Crimmins Algorithm, ADS: Anisotropic Diffusion Smoothing

score of the proposed method falls behind those of MF and CA. However, in almost all cases CA has performed over-smoothing.

Correct Processing Ratio

A pixel in a smooth image is said to be *noisy* if its gray value is not same as that of the ideal noise-free image. This difference in gray value can be due to some amount of noise still present or due to degradation of feature. The basic purpose of a noise smoothing algorithm should be to modify the gray value of the noisy pixels keeping

those of the noise-free pixels unaltered as far as possible. In this context the *correct processing ratio* CPR is defined as [169]

$$CPR = \frac{1}{N}\Sigma_r\Sigma_c\{I_B(r,c) + I_C(r,c)\} \tag{3.22}$$

where N is the total number of pixels in the image, and $I_B(r,c)$ and $I_C(r,c)$ are defined as

$$I_B(r,c) = \begin{cases} 1, & \text{if } g(r,c) = f(r,c) \text{ and } \tilde{g}(r,c) = g(r,c) \\ 0, & \text{otherwise} \end{cases} \tag{3.23}$$

and

$$I_C(r,c) = \begin{cases} 1, & \text{if } g(r,c) \neq f(r,c) \text{ and } \tilde{g}(r,c) \neq g(r,c) \\ 0, & \text{otherwise} \end{cases} \tag{3.24}$$

where $f(r,c)$, $g(r,c)$ and $\tilde{g}(r,c)$ are, respectively, the ideal noise-free, noisy and the smooth image. A good smoothing algorithm should have CPR value very close to unity. Accordingly, we have given scores to the methods. From the table 3.5 it is evident that our proposed method has the second highest ranking in terms of its overall score.

We have also studied the variation of the performance metrics SNR, DMB and CPR with the largest scale factor n (i.e. the height of the towers). The variation of the SNR with the largest scale factor n is shown in fig. 3.5 The signal-to-noise ratio should increase with the largest scale factor. As the largest scale factor is increased, the features at the lower scales get progressively smaller weights in the reconstruction of the smoothed image. The noise predominates at the lower scales. Therefore the SNR values should increase with the largest scale factor. This trend is observed in almost all cases except the *Gaussian* and *Speckle* noise.

The variation of the DMB with the largest scale factor n is shown in fig. 3.6. As we proceed with higher scale the effect of noise is expected to die out. The DMB, is therefore, expected to decrease with the largest scale factor. This trend is observed in the figure. A negative trailing indicates over-smoothing.

Table 3.5: Correct processing ratio value CPR for different noise removal schemes

Type of Noise	Correct processing ratio value and score of the scheme							
	MMS		MF		CA		ADS	
	CPR	score	CPR	score	CPR	score	CPR	score
Exp	0.894104	3	0.912628	4	0.883774	2	0.882538	1
Gus	0.922318	3	0.930511	4	0.920120	2	0.902786	1
Pos	0.550140	2	0.636810	3	0.542679	1	0.755737	4
Ral	0.962555	3	0.973022	4	0.908737	1	0.941376	2
Sht	0.509003	4	0.503113	3	0.268234	1	0.501587	2
Uni	0.964340	3	0.970032	4	0.951797	2	0.933578	1
Spk	0.950699	3	0.957886	4	0.939911	2	0.921738	1
TOTAL		21		26		11		12

Type of Noise: Exp: Exponential noise, Gus: Gaussian noise, Pos: Poisson noise, Ral: Rayleigh noise Sht: Shot noise, Uni: Uniform noise, Spk: Speckle noise NI : Noisy Image, MMS: Multi-scale Morphological Smoothing, MF: Median Filtering, CA: Crimmins Algorithm, ADS: Anisotropic Diffusion Smoothing

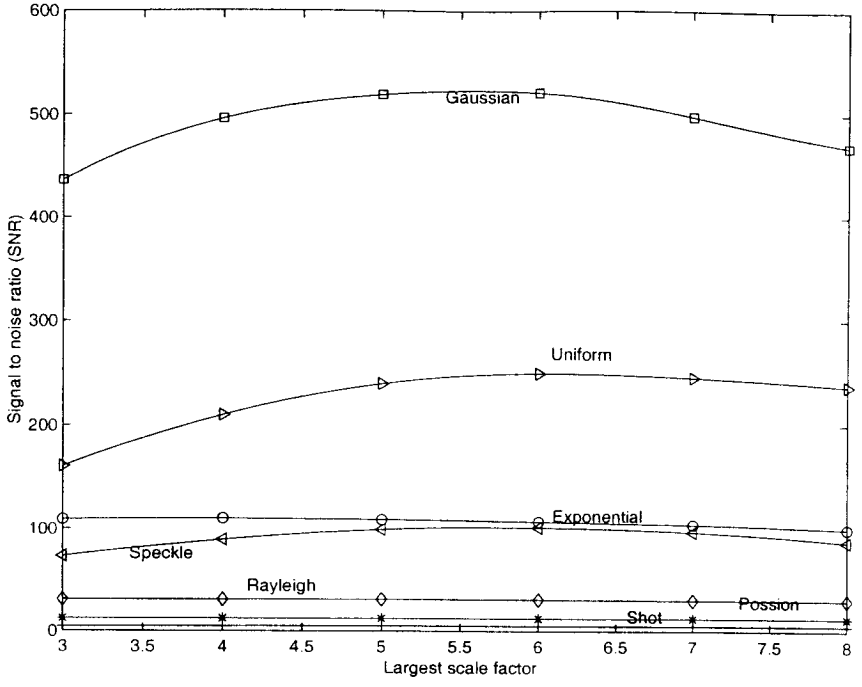

Figure 3.5: Variation of SNR with the largest scale factor

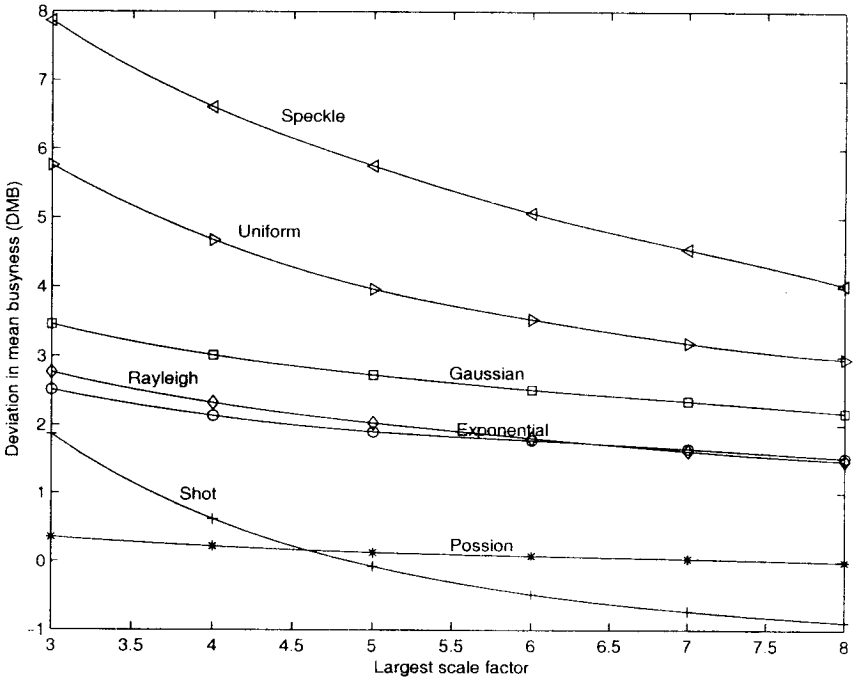

Figure 3.6: Variation of DMB with the largest scale factor

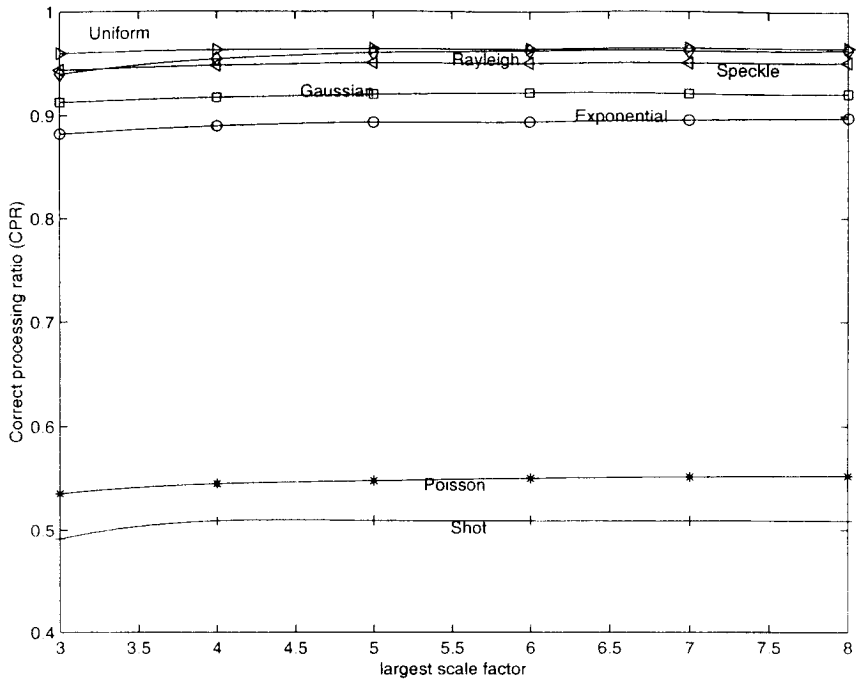

Figure 3.7: Variation of CPR with the largest scale factor

The variation of the CPR with the largest scale factor (i.e. the height of the tower) is shown in fig. 3.7. The CPR values are found to improve with the largest scale factor.

3.4 Modification of the proposed scheme (MMS-1) considering noise statistics: MMS-2

As mentioned earlier that the noise grains are expected to predominate in the lower range of scale. With such view we have assigned progressively lower weightages to the feature images of low scale. However, though it is agreed upon by many researchers (e.g., Toet [155], Bangham et. al. [14]) that random unstructured noise dominate at the lower scale, the way we assign weightages to the feature images

during reconstruction is purely *ad-hoc* in nature. On the other hand, estimating the weights through optimization of goodness criterion as suggested in equation (3.4) incurs a huge computational cost for each image. A compromise between these two approaches might be assigning weightage depending on the amount of noise present at a scale. Since we have no *a priori* knowledge of noise statistics at individual scale, we suggest an empirical formula for computing weightages for bright and dark feature images at scale i respectively as

$$k_i^o = \frac{\eta_i^o}{\sum_{i=0}^{n} \eta_i^o} \tag{3.25}$$

$$k_i^c = \frac{\eta_i^c}{\sum_{i=0}^{n} \eta_i^c} \tag{3.26}$$

where

$$\eta_i^o = \frac{(\text{image size})(\text{size of } iB)}{\sum_r \sum_c F_{iB}^o(r,c)} \tag{3.27}$$

$$\eta_i^c = \frac{(\text{image size})(\text{size of } iB)}{\sum_r \sum_c F_{iB}^c(r,c)} \tag{3.28}$$

for $i = 1, 2, 3, \ldots, n$. However, if the denominators of equations (3.27) and (3.28) are zero, we assign zero value to k_i^o and k_i^c. Finally, smooth image is reconstructed using equation (3.2). Let us call this scheme MMS-2 and the previous one MMS-1.

We have reconstructed new sets of results following this method and compared these with that of MMS-1 obtained previously. The images resulting after executing MMS-2 on the same set of input noisy images are shown in fig. 3.8.

3.4.1 Comparison between MMS-1 and MMS-2

Qualitative comparison by human observer reveals that the performance of MMS-1 and MMS-2 are almost same. Apart from visual judgment we have compared the *SNR*, *DMB* and *CPR* values of the images resulting from MMS-1 and MMS-2 for

during reconstruction is purely *ad-hoc* in nature. On the other hand, estimating the weights through optimization of goodness criterion as suggested in equation (3.4) incurs a huge computational cost for each image. A compromise between these two approaches might be assigning weightage depending on the amount of noise present at a scale. Since we have no *a priori* knowledge of noise statistics at individual scale, we suggest an empirical formula for computing weightages for bright and dark feature images at scale i respectively as

$$k_i^o = \frac{\eta_i^o}{\sum_{i=0}^{n} \eta_i^o} \tag{3.25}$$

$$k_i^c = \frac{\eta_i^c}{\sum_{i=0}^{n} \eta_i^c} \tag{3.26}$$

where

$$\eta_i^o = \frac{(\text{image size})(\text{size of } iB)}{\sum_r \sum_c F_{iB}^o(r,c)} \tag{3.27}$$

$$\eta_i^c = \frac{(\text{image size})(\text{size of } iB)}{\sum_r \sum_c F_{iB}^c(r,c)} \tag{3.28}$$

for $i = 1, 2, 3, \ldots, n$. However, if the denominators of equations (3.27) and (3.28) are zero, we assign zero value to k_i^o and k_i^c. Finally, smooth image is reconstructed using equation (3.2). Let us call this scheme MMS-2 and the previous one MMS-1.

We have reconstructed new sets of results following this method and compared these with that of MMS-1 obtained previously. The images resulting after executing MMS-2 on the same set of input noisy images are shown in fig. 3.8.

3.4.1 Comparison between MMS-1 and MMS-2

Qualitative comparison by human observer reveals that the performance of MMS-1 and MMS-2 are almost same. Apart from visual judgment we have compared the *SNR*, *DMB* and *CPR* values of the images resulting from MMS-1 and MMS-2 for

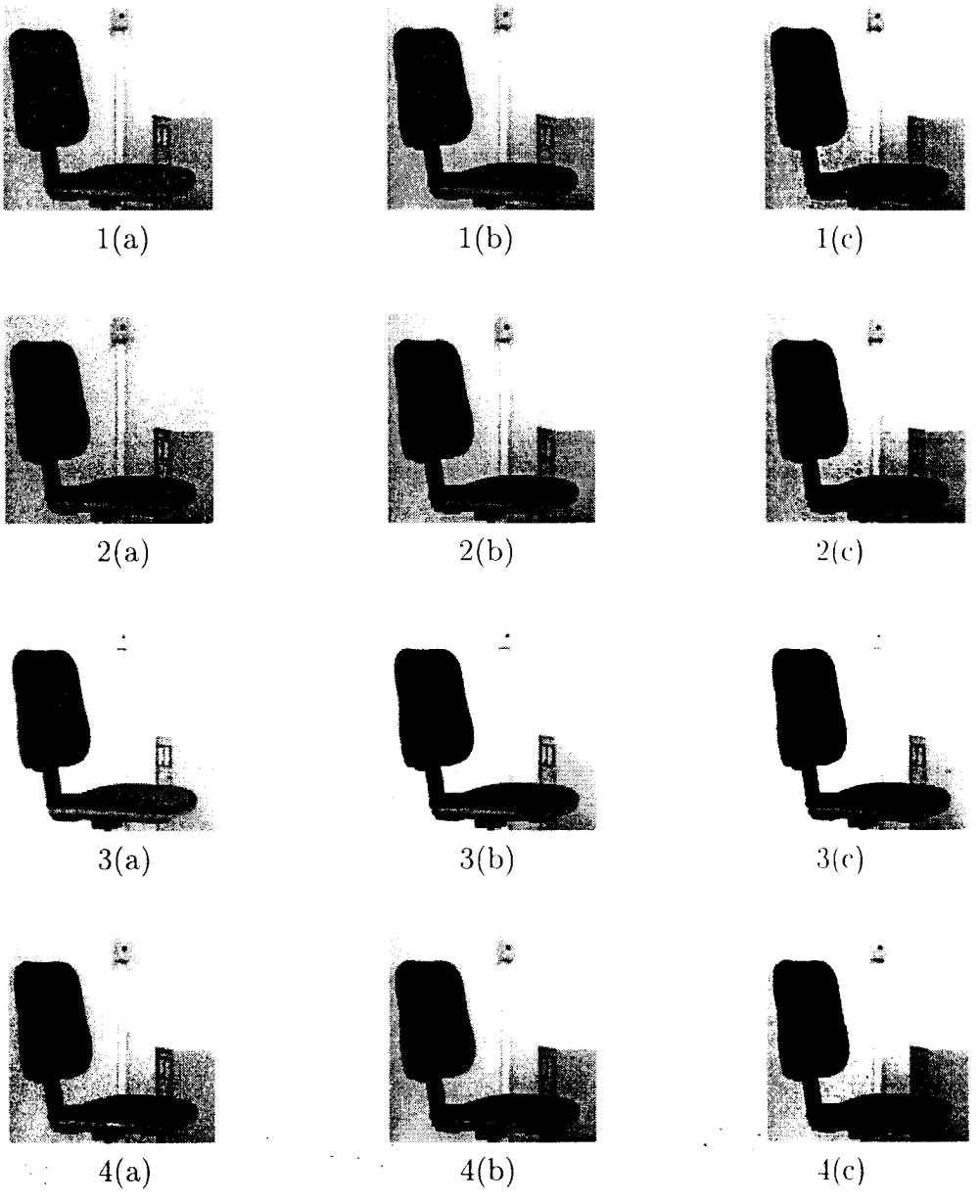

Figure 3.8: (a) Original noisy image, (b) result of proposed multi-scale morphological noise removal filtering (MMS-1) and (c) result of proposed multi-scale morphological noise removal filtering using noise statistics (MMS-2) for (1) *exponential* noise, (2) *Gaussian* noise, (3) *Poisson* noise, (4) *Rayleigh* noise, (5) *shot* noise, (6) *uniform* noise and (7) *speckle* noise.

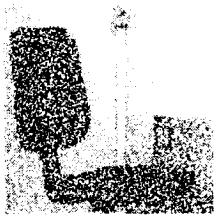

5(a)

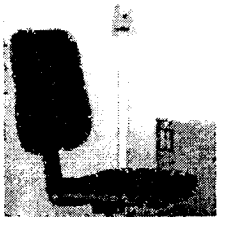

5(b)

5(c)

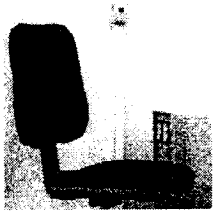

6(a)

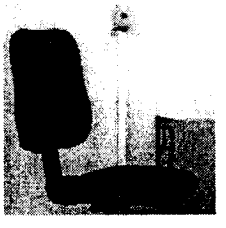

6(b)

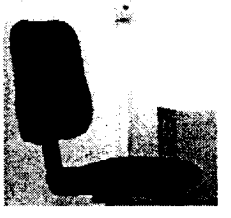

6(c)

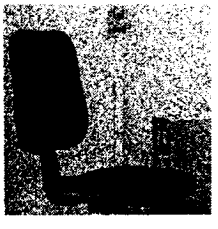

7(a)

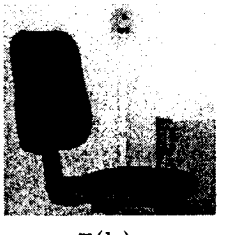

7(b)

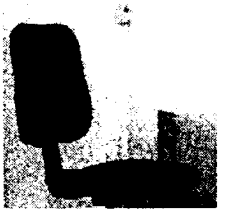

7(c)

Figure 3.8: Continued

each type of noise. The same convention of ranking a method is followed. The measures are summarized in tables [3.6 - 3.8] as follows.

Table 3.6 shows the SNR values of the images resulting from MMS-1 and MMS-2 along with the ranks. The SNR values in most cases are found to improve when noise statistics is considered. Table 3.7 shows the DMB values of the images resulting from MMS-1 and MMS-2 along with the ranks. From the table it is evident that the performances of MMS-1 and MMS-2 in terms of deviation in mean business value are almost same. However, very precisely speaking the overall performance of MMS-1 is slightly better. Again as before, we have computed the CPR values of the images resulting from MMS-1 and MMS-2 and compared them assigning ranks. Table 3.8 shows the CPR values of the images resulting from MMS-1 and MMS-2 along with the scores. The overall correct processing of MMS-2 is found to be slightly better than that of MMS-1.

Table 3.7: Deviation in mean busyness values (DMB) for MMS-1 and MMS-2

Type of Noise	Deviation in mean busyness value and score of the scheme				
	NI	MMS-1		MMS-2	
	DMB	DMB	score	DMB	score
Exp	10.921769	1.776302	1	1.760339	2
Gus	14.009873	2.513388	2	2.580885	1
Pos	3.561615	0.076848	2	0.079354	1
Ral	12.423284	1.810181	2	1.898009	1
Sht	56.100977	-0.485336	2	-0.600246	1
Uni	26.590066	3.531104	1	3.470512	2
Spk	31.357986	5.062269	2	5.118432	1
TOTAL			12		9

Type of Noise: Exp: Exponential noise, Gus: Gaussian noise, Pos: Poisson noise, Ral: Rayleigh noise Sht: Shot noise, Uni: Uniform noise, Spk: Speckle noise

NI : Noisy Image, MMS-1: Multi-scale Morphological Smoothing, MMS-2:Multi-scale Morphological Smoothing using noise statistics

Table 3.8: Correct processing ratio value (CPR) for MMS-1 and MMS-2

Type of Noise	Correct processing ratio value and score of the scheme			
	MMS-1		MMS-2	
	CPR	score	CPR	score
Exp	0.894104	1	0.894684	2
Gus	0.922318	2	0.921860	1
Pos	0.550140	2	0.549713	1
Ral	0.962555	2	0.961853	1
Sht	0.509003	1	0.509415	2
Uni	0.964340	1	0.964981	2
Spk	0.950699	1	0.950806	2
TOTAL		10		11

Type of Noise: Exp: Exponential noise, Gus: Gaussian noise, Pos: Poisson noise, Ral: Rayleigh noise Sht: Shot noise, Uni: Uniform noise, Spk: Speckle noise

MMS-1: Multi-scale Morphological Smoothing, MMS-2:Multi-scale Morphological Smoothing using noise statistics

Table 3.8: Correct processing ratio value (CPR) for MMS-1 and MMS-2

Type of Noise	Correct processing ratio value and score of the scheme			
	MMS-1		MMS-2	
	CPR	score	CPR	score
Exp	0.894104	1	0.894684	2
Gus	0.922318	2	0.921860	1
Pos	0.550140	2	0.549713	1
Ral	0.962555	2	0.961853	1
Sht	0.509003	1	0.509415	2
Uni	0.964340	1	0.964981	2
Spk	0.950699	1	0.950806	2
TOTAL		10		11

Type of Noise: Exp: Exponential noise, Gus: Gaussian noise, Pos: Poisson noise, Ral: Rayleigh noise Sht: Shot noise, Uni: Uniform noise, Spk: Speckle noise MMS-1: Multi-scale Morphological Smoothing, MMS-2:Multi-scale Morphological Smoothing using noise statistics

We have seen how morphological towers can be employed in smoothing random noise of different types from graylevel images preserving the edge features. Now, we will consider the problem of local contrast enhancement of graylevel images and try to solve the problem using morphological tower.

3.5 Proposed method for contrast enhancement

3.5.1 Theoretical formulation

A good ambience of light illuminating the object or scene to be imaged may give rise to exhaustive utilization of the entire dynamic range of gray-scale in the image, but the contrast over small regions of the image may be very poor. Second, a relatively smaller number of pixels in such areas are insufficient to have any significant influence on the computation of global transformation. So the conventional histogram stretching or histogram equalization technique fail to serve the purpose. Such images need local enhancement and the technique by which this can be achieved is called *local contrast stretching*.

A local contrast stretching method using local statistics suggested by Lee [78, 79] amplifies the difference between gray-level $g(r,c)$ and mean gray-level $\overline{g}(r,c)$ over a predefined neighborhood surrounding the pixel (r,c). Thus the modified gray-level $\tilde{g}(r,c)$ is given by

$$\tilde{g}(r,c) = \overline{g}(r,c) + k[g(r,c) - \overline{g}(r,c)] \tag{3.29}$$

where k is a global amplification factor and is greater than one. In another approach Narendra and Fitch [119] have considered the amplification factor also be a function of (r,c) based on the local gray-level statistics over the same neighborhood as is used to define the mean gray-level $\overline{g}(r,c)$. Suppose gray-level variance over that neighborhood

is $\sigma^2(r,c)$. Then the factor $k(r,c)$ is defined as

$$k(r,c) = \gamma \frac{\overline{g}}{\sigma^2(r,c)}, \qquad 0 < \gamma \leq 1$$

where $\overline{g}$ is the global mean of image gray-level and γ is a user defined parameter.

The histogram equalization technique may be adopted to enhance the local contrast of the image. In this method the intensity of each pixel is modified through a local histogram equalization over a small region of the image around that pixel [109, 119, 121, 124].

However, this kind of transformation using only local gray-level statistics cannot distinguish between consistent variation in intensity over a region and the variation in intensity due to presence of a feature (bright or dark) within a region. So it may stretch contrast evenly in both the cases. As a result, undesired contrast intensification (in supposedly smooth region) takes place at some regions of the image, which may require further processing such as *de-enhancement* [109]. On the other hand, if local contrast is stretched based on the presence of spatial features, then this problem can be avoided completely. As mathematical morphology is an appropriate tool for dealing with spatial features or shapes, we intend to modify equation (3.29) in terms of mathematical morphological operators.

As mentioned in section 2.2, the bright top-hat transformation decomposes an image into two parts, the baseimage and the feature image

$$g(r,c) = \underbrace{(g \circ B)(r,c)}_{\text{part 1}} + \underbrace{[g(r,c) - (g \circ B)(r,c)]}_{\text{part 2}} \tag{3.30}$$

The feature image [i.e., part 2 of equation (3.30)] gives a measure of local contrast in the original image due to presence of bright features. Hence, combining equations (3.29) and (3.30) we suggest the following transformation for local contrast stretching

$$\tilde{g}(r,c) = (g \circ B)(r,c) + k[g(r,c) - (g \circ B)(r,c)] \tag{3.31}$$

where k is again a global amplification factor and is greater than one. So this transformation makes bright features brighter and, thus, improves the local contrast. Now suppose $k = 2$. The equation (3.31) becomes

$$\tilde{g}(r,c) = g(r,c) + [g(r,c) - (g \circ B)(r,c)] \tag{3.32}$$

Let us denote $[g(r,c) - (g \circ B)(r,c)]$ by $F^o_B(r,c)$, i.e, features of size less than that of B obtained by opening (more specifically, by bright top-hat transformation). Accordingly, we can rewrite equation (3.32) as

$$\tilde{g}(r,c) = g(r,c) + F^o_B(r,c) \tag{3.33}$$

Similarly we denote the bright-feature image at scale n by $F^o_{nB}(r,c)$ as it contains all the features of $g(r,c)$ that are smaller than nB. Hence, the value $F^o_{nB}(r,c)$ of bright-feature image at (r,c) gives a measure of local contrast in the original image due to presence of bright features at scale n. Note that $F^o_{0B}(r,c)$ is an all-zero image. Now, let us define

$$\delta^o_n(r,c) = F^o_{nB}(r,c) - F^o_{(n-1)B}(r,c) \tag{3.34}$$

It is evident that $\delta^o_n(r,c)$ contains bright features of $g(r,c)$ that are larger than scale $(n-1)$, but smaller than scale n. Therefore, we obtain, using multi-scale approach, local contrast stretching of bright features as

$$\tilde{g}(r,c) = g(r,c) + k_1\delta^o_1(r,c) + k_2\delta^o_2(r,c) + k_3\delta^o_3(r,c) + \cdots \tag{3.35}$$

where $k_1 > k_2 > k_3 > \ldots$, since we know that smaller the size of a bright feature, more should be its intensity for detectability. Suppose the features upto the scale m are needed to be enhanced then

$$\tilde{g}(r,c) = g(r,c) + \sum_{i=1}^{m} k_i\delta^o_i(r,c) \tag{3.36}$$

Theoretically, m may correspond to SE as large as the entire image; however, for all practical purpose m is small. This is because large features, in general, contribute

heavily to global histogram and thus can influence global contrast stretching in their favour. Secondly, the probability that $\delta_i^o(r,c)$ being null image is more as i increases. So we ignore $\delta_i^o(r,c)$ for $i > m$. Now taking $k_{i-1} = k_i + 1$ for all i and choosing $k_m = 1$ we finally have local contrast stretching of bright features as

$$\tilde{g}(r,c) = g(r,c) + \sum_{i=1}^{m} F_{iB}^o(r,c) \tag{3.37}$$

Selecting $k_m = 1$ we can avoid multiplication operation to compute enhanced image and, thus, the computational cost is reduced to some extent.

Proceeding in a similar way based on multi-scale dark top-hat transformations we achieve local contrast stretching of dark features as

$$\tilde{g}(r,c) = g(r,c) - \sum_{i=1}^{m} F_{iB}^c(r,c) \tag{3.38}$$

Hence, to obtain the modified image, in which contrast of both (bright and dark) types of features are stretched locally, we add equations (3.37) and (3.38) and divide the result by 2 to get

$$\tilde{g}(r,c) = g(r,c) + 0.5\sum_{i=1}^{m} F_{iB}^o(r,c) - 0.5\sum_{i=1}^{m} F_{iB}^c(r,c) \tag{3.39}$$

The constant multiplier 0.5 is used for assigning equal or impartial weightages to both dark and bright features. For the sake of generalization, we modify equation (3.39) as

$$\tilde{g}(r,c) = g(r,c) + 0.5\sum_{i=n}^{m} F_{iB}^o(r,c) - 0.5\sum_{i=n}^{m} F_{iB}^c(r,c) \tag{3.40}$$

where all the features, either dark of bright, smaller than scale n are assumed to be noise in the image. This equation resembles equation (2.43) for multi-scale morphological feature decomposition of an image. However, the difference is, here, we add the top-hat images at different scale with the original image. In equation (2.43) we add the scale-specific feature images (difference of top-hat images at successive scale) with the base image.

From equation (3.40) it is evident that adding multi-scale bright and dark top-hat images is identical with adding scale-specific feature images with more weightages to the features of smaller scales. The normal reconstruction of an image from its multi-scale decomposition according to equation (2.43) suggests use of equal weightages to scale-specific feature images. Assigning more weights to features of small scales surely implies contrast enhancement. The order of the assigned weights in case of contrast is just the reverse of that in case of noise smoothing [see section 3.2.1]

3.5.2 A simple illustration in one-dimension

For a better understanding of the local contrast enhancement scheme we first elaborate it in the context of one-dimensional function as shown in fig. 3.9. Here we intend to enhance a function $g(t)$ locally. The function $g(t)$ has salient features manifested as *crests* and *troughs* of different height (*or depth*) and width located at different positions. A line segment L of unit length and its higher order dilates kL (where $k = 1, 2, 3..$) are used as structuring elements (SE) for extracting the features from the function as described below:

- The opening operation with the SE kL removes the crests narrower than the length k from the function while the closing operation fills up the troughs narrower than the length k .
- The function $top_k(t) = (g(t) - g(t) \circ kL)$ contains only the crests narrower than k and the function $bot_k(t) = (g(t) \bullet kL - g(t))$ contains only the troughs narrower than k.
- The functions $S_{op}(t) = 0.5\Sigma top_k(t)$ and $S_{cl}(t) = 0.5\Sigma bot_k(t)$ are constructed by summing up the $top_k(t)$ and $bot_k(t)$ respectively followed by a scaling in

magnitude to avoid probable clippings. In doing so the crests and troughs of narrower widths are made to have more contribution to $S_{op}(t)$ and $S_{cl}(t)$.

- The locally enhanced function is then formed by combining the functions $S_{op}(t)$ and $S_{cl}(t)$ with the original function as shown below:

$$g_{enh}(t) = g(t) + S_{op}(t) - S_{cl}(t) \tag{3.41}$$

Comparing $g_{enh}(t)$ with $g(t)$ at each sample point t it can be found that height (depth) of the crests (troughs) have increased but disproportionately. The change in height (or depth) is more for crest (or trough) of narrower width which would have not been possible using simple linear stretching of the function. The scheme explained for this one-dimensional case may as well be extended in two-dimension.

3.5.3 Implementation

The implementation of equation (3.40) describing feature based local contrast enhancement involves construction of a number of morphological towers as elaborated below.

Construction of Morphological Towers

The image to be enhanced is made to undergo a sequence of gray-scale morphological opening operations with a disc structuring element and its higher order homothetics. The resulting sequence of images are kept in a stack called the *opening tower* as shown in the fig 3.10. An identical tower, called closing tower, is constructed with the sequence of the images resulting from multi-scale closing of the input image. Therefore the i-th entry in the opening (closing) tower contains the image opened(closed) with the structuring element iB. This part is same as that of noise smoothing.

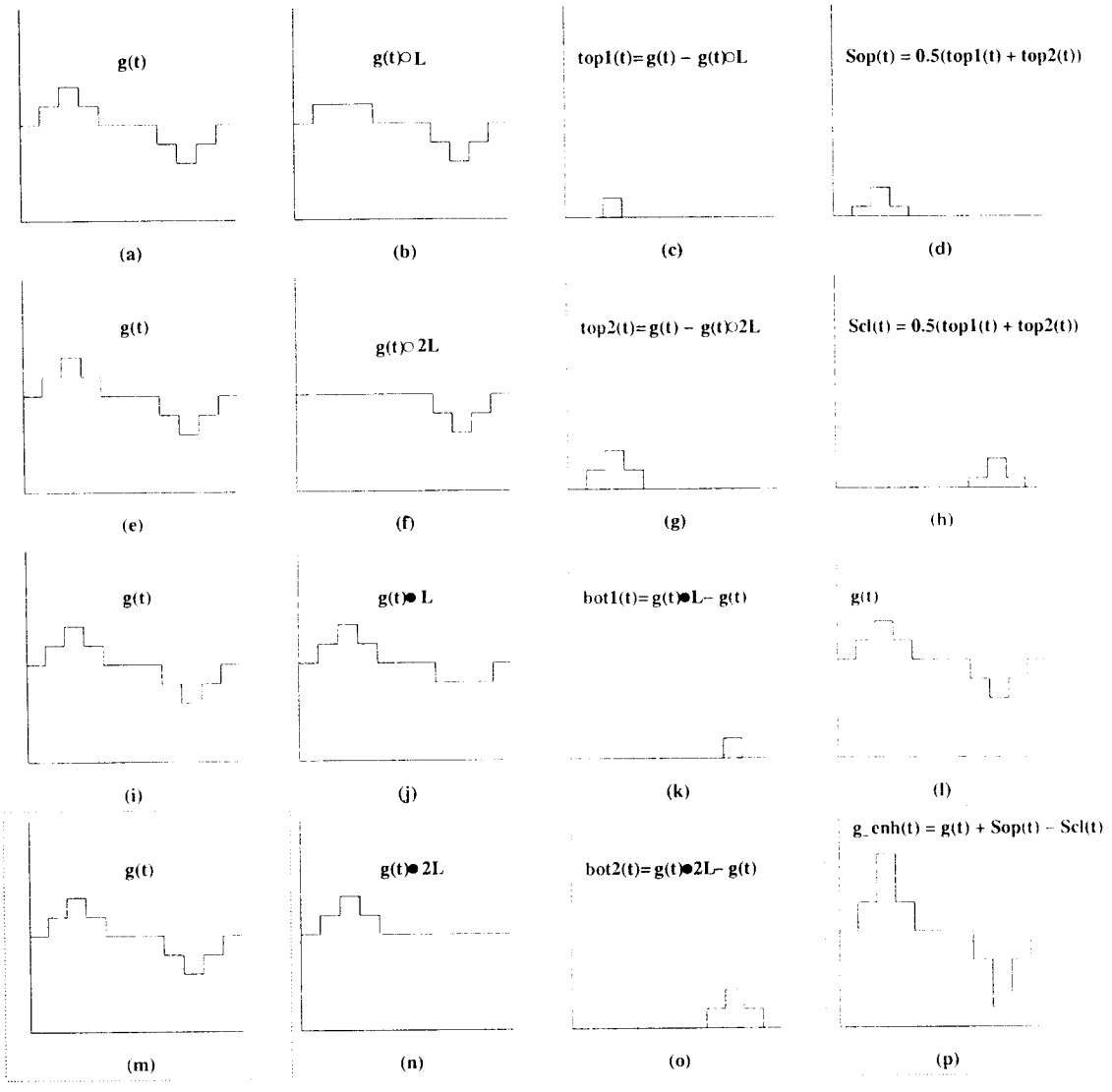

Figure 3.9: Local contrast enhancement of a function: (a),(e),(i),(m)and (l) original function, (b), (f) function opened with line SE, (j),(n) function closed with line SE, (c),(g) bright top-hat functions (k),(o) dark top-hat functions, (d) scaled sum of bright top-hat functions, (h) scaled sum of dark top-hat functions and (p) the output function after local contrast enhancement.

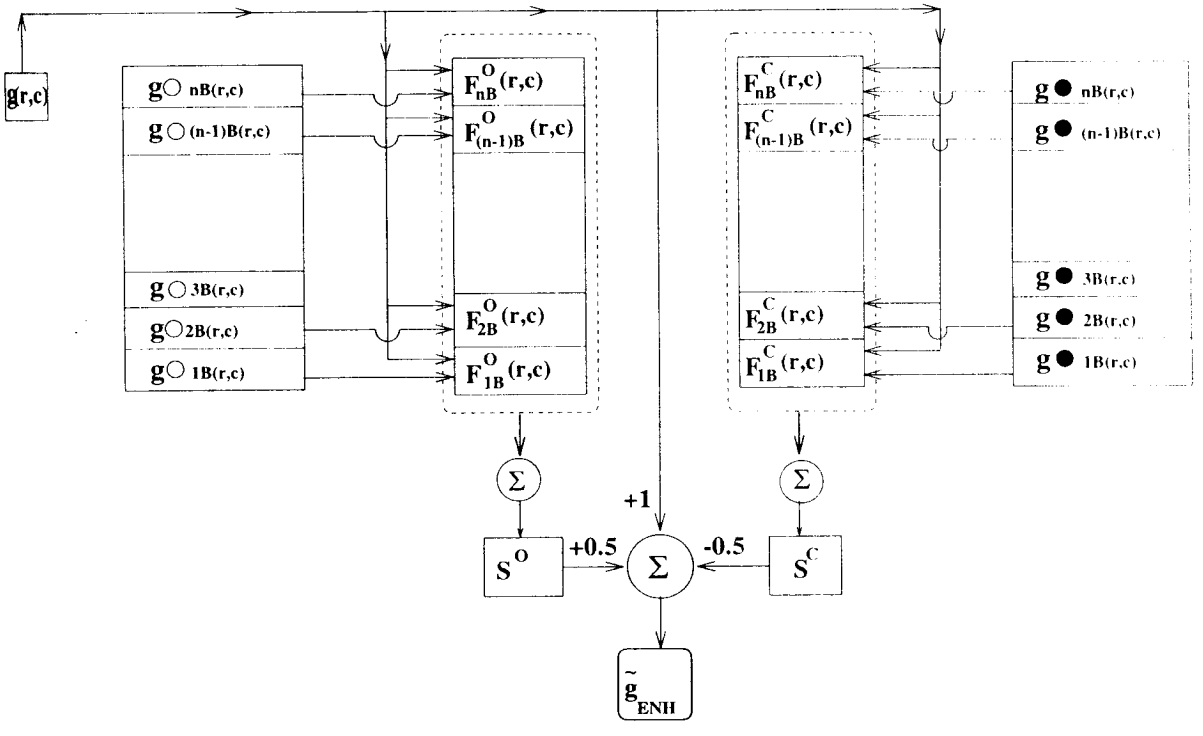

Figure 3.10: Schematic diagram for local contrast enhancement using morphological towers

Construction of difference Towers

Each entry of the opening tower is subtracted individually from the original image and the resulting bright feature images are then kept in corresponding entries in another tower called the *difference tower*. An identical difference tower is constructed for the dark feature images obtained by subtracting the original image from each entry of the closing tower. Therefore the i-th entry in the difference tower for opening (closing) contains an image consisting of bright (dark) features which are smaller than or equal to iB as given below.

$$F^o_{iB}(r,c) = g(r,c) - (g \circ iB)(r,c) \tag{3.42}$$

$$F^c_{iB}(r,c) = (g \bullet iB)(r,c) - g(r,c) \tag{3.43}$$

for $i = 1, 2, \ldots, n$.

Construction of the enhanced image

For reconstructing the final image we do the following :

- We construct an image by combining all the feature images in the difference tower corresponding to the opening operation. This results in an image consisting of bright features of all possible scales of interest that are present in the original image.

$$S^o(r,c) = \sum_{i=1}^{n} F^o_{iB}(r,c) \tag{3.44}$$

  The summation, here, denotes pixel-wise sum of n images.

- We perform the same operation on the difference tower corresponding to the closing operation. This results in an image consisting of dark features of all

scales of interest that are present in the original image.

$$S^c(r,c) = \sum_{i=1}^{n} F_{iB}^c(r,c) \tag{3.45}$$

Finally, the locally enhanced image is constructed by combining three images using

$$\tilde{g}(r,c) = g(r,c) + 0.5S^{op}(r,c) - 0.5S^{cl}(r,c) \tag{3.46}$$

The '+' and '-' operations are applied between corresponding pixels of three different images. However, it should be noted that at some pixels the value of $\tilde{g}(r,c)$ computed using equation (3.46) may exceed the allowed gray-level range. In that case the weights 0.5 may be replaced by α such that not more than 1% of total pixels are clipped. The value of α can be selected between 0 and 0.5 using binary search technique.

The algorithms for multi-scale contrast enhancement are given below. In the first pass the algorithm collects the features at various scales and stack them in different morphological towers

Extraction of multi-scale features

Procedure *Extract_multi-scale_features()*

input: $g[][]$; /* the original input image */

output: bright_feature_tower, dark_feature_tower; /* towers of filtered images */

constant: $MAXSCALE$; /* upper bound of scale factor */

var: $g_{op}[][]$, $g_{cl}[][]$; /* intermediate images */

var: $g_i^{top}[][]$, $g_i^{bot}[][]$; /* intermediate images */

integer: i;

$i \leftarrow 1$;

begin

repeat

$g_{op} \leftarrow morph\_open(g, iB)$;

$g_i^{top} \leftarrow g$ - g_{op};

$insert\_in\_tower(g_i^{top}, bright\_feature\_tower, i)$;

$g_{cl} \leftarrow morph\_close(g, iB)$;

$g_i^{bot} \leftarrow g_{cl}$ - g_{in};

$insert\_in\_tower(g_i^{bot}, dark\_feature\_tower, i)$;

$increase\ i$;

until $i > MAXSCALE$;

end begin

end Procedure

In the second pass the scale-specific feature images stacked in the towers are combined with the original input image using the following algorithm

Formation of enhanced image

Procedure *Combine_multi-scale_feature_images()*

input: bright_feature_tower, dark_feature_tower; /* towers of filtered images */

input: $g[][]$ /* the input image */

output: $g_{enh}[][]$; /* the output enhanced image */

var: $g_{temp}, g_{btemp}[][], g_{dtemp}[][]$; /* intermediate images */

constant: $MAXSCALE$; /* upper bound of scale factor */

integer: i;

$i \leftarrow 1$;

$g_{enh}[][] \leftarrow g[][]$;

begin

repeat

$g_{temp} \leftarrow get\_image\_from(bright\_feature\_tower, i)$;

$g_{btemp} \leftarrow g_{btemp} + g_{temp}$;

$g_{temp} \leftarrow get\_image\_from(dark\_feature\_tower, i)$;

$g_{dtemp} \leftarrow g_{dtemp} + g_{temp}$;

increase i;

until $i > MAXSCALE$;

end begin

$g_{enh}[][] \leftarrow g[][] + 0.5 * g_{btemp} - 0.5 * g_{dtemp}$

end Procedure

3.6 Experimental results and discussion

The proposed algorithm has been tested on a set of biomedical images and the results have been compared with that of other methods [see figs. (3.11-3.14)]. Here we present detailed study with three example images. The images contain MR scan of human brain. Fig 3.11 shows the original image along with its gray-level histogram and the results of global enhancement techniques like linear contrast stretching and histogram equalization of it. It is observed from the examples that the global techniques cannot improve the contrast of the image satisfactorily. Results of the proposed algorithm are shown in figs [3.12-3.14](b) where $n = 1$ (as the images are assumed to be noise-free), $m = 6$ and B is a circle of unit radius. The value of m can be made larger depending on demand or precision. However, it should be noted that very large value of m will not give noticeable improvement in the output since the feature images of progressively larger scales have gradually smaller weightages in enhancing the image. Moreover, very large value of m, in spite of incorporating generality in the scheme, increases the computational time unnecessarily. The resulting image is seen to have more contrast than its original version. Results of other local contrast enhancement algorithms such as local histogram stretching [39], contrast amplification based on local statistics [119] and the local histogram equalization [109] are shown in fig. 3.12[c-e] respectively so

as to get some idea about their relative performance. In each case the size of the local window has been fixed at 13×13. The amplification factor in the algorithm due to Dorst has been fixed at 3. For local contrast enhancement using local statistics due to Narendra et. al., the values for the minimum standard deviation and the scale factor chosen are 0.05 and 1 respectively. For local histogram equalization the threshold for the ratio of *global mean* to *local variance* is fixed at 0.5. However, from the results, the enhancement of noise is found to be the least in case of morphological enhancement proposed by the authors. The significant local enhancement of the image without appreciable enhancement of noise proves the efficacy of the proposed method.

3.6.1 Performance analysis

For comparing the performance of the enhancement schemes quantitatively we define the degree of enhancement in terms of *overall contrast* by computing the average value of the difference of the maximum and minimum graylevel (i.e. local contrast) over a 3×3 mask surrounding each pixel location of the enhanced image.

$$\begin{aligned} d(r,c) &= \Sigma_{p=r-1}^{r+1}\Sigma_{q=c-1}^{c+1}[\tilde{g}_{max} - \tilde{g}_{min}] \\ Cont &= \frac{1}{MN}\Sigma_{r=0}^{M-1}\Sigma_{c=0}^{N-1}d(r,c) \end{aligned}$$

The overall contrast is computed for the original image and the enhanced images resulting from all the enhancement schemes. From table 3.9 it is evident that the overall contrast is the best for the proposed method. he proposed scheme emphasizes equally on the bright and dark features and therefore makes use of both bright and dark top-hat transformation for enhancing the features. However, for the sake of comparison we have executed the proposed algorithm on the same set of images using bright and dark top-hat transformation separately. The results are shown in fig. 3.15. The results are found to be better in case of the method employing only bright top-

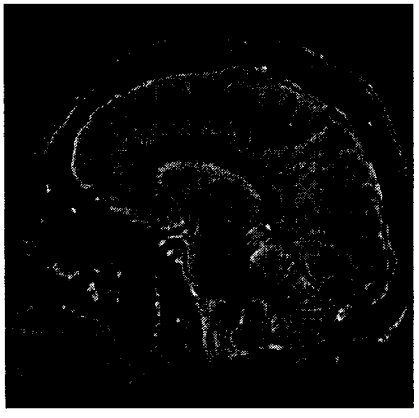

(a)

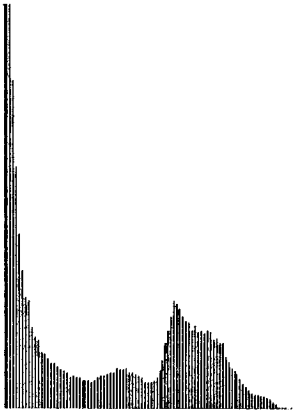

(b)

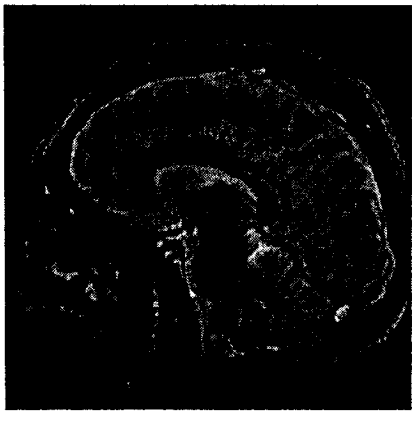

(c)

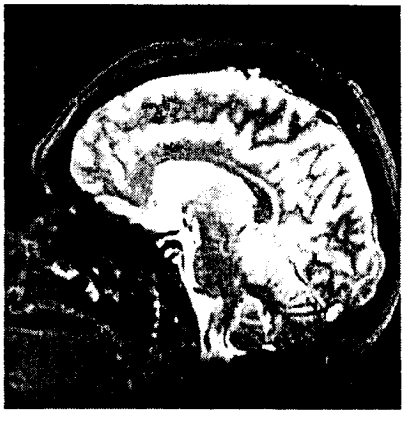

(d)

Figure 3.11: (a) Original image, (b) histogram of the original image, (c) result of linear global contrast stretching and (d) result of global histogram equalization

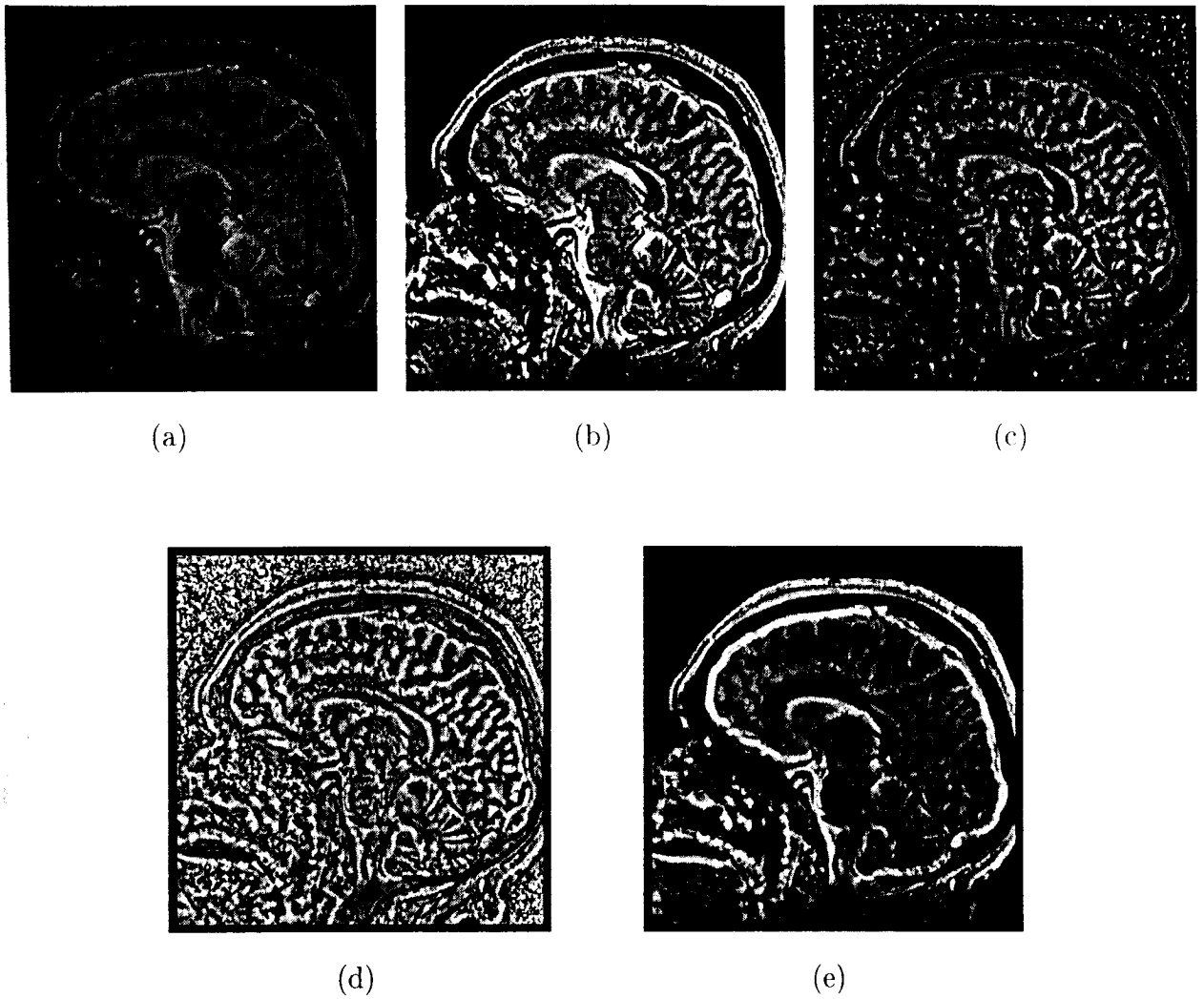

Figure 3.12: (a) Original image, (b) result of local contrast stretching using multi-scale morphology, (c) result of local contrast stretching based on local statistics(Narendra et. al.), (d) result of local histogram equalization and (e) result of local contrast stretching following the algorithm due to Dorst.

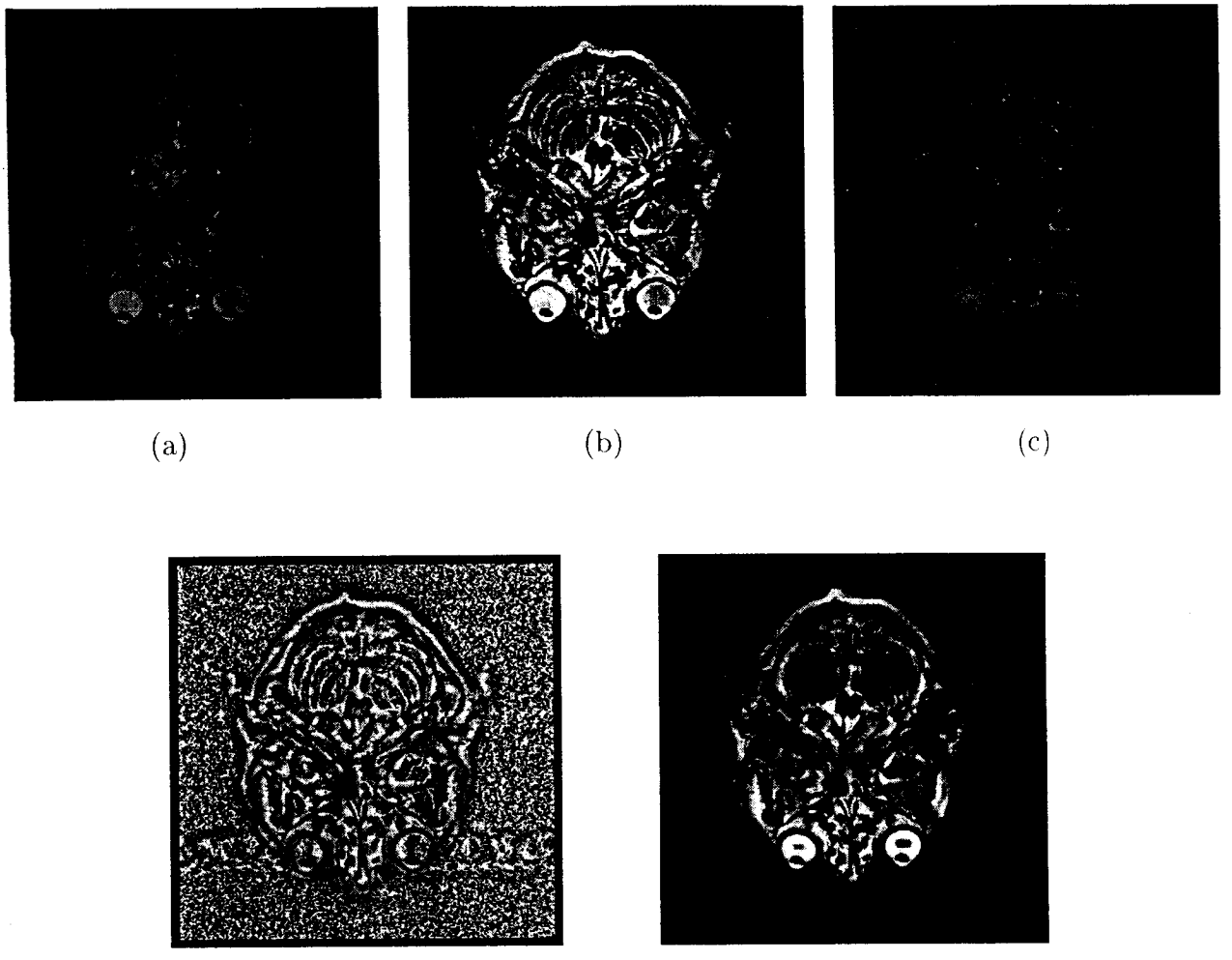

(a) (b) (c)

(d) (e)

Figure 3.13: (a) Original image, (b) result of local contrast stretching using multi-scale morphology, (c) result of local contrast stretching based on local statistics(Narendra et. al.), (d) result of local histogram equalization and (e) result of local contrast stretching following the algorithm due to Dorst.

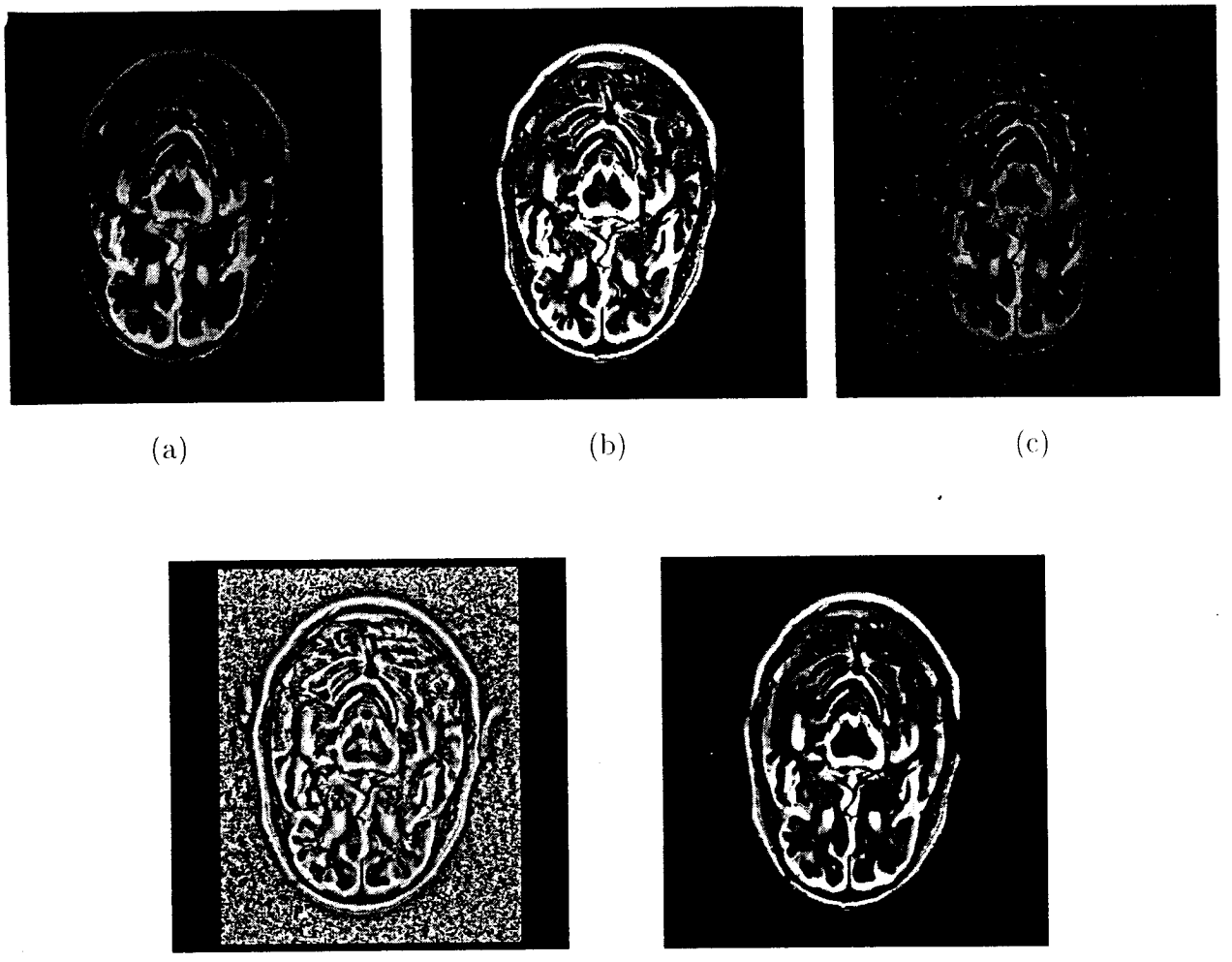

Figure 3.14: (a) Original image, (b) result of local contrast stretching using multi-scale morphology, (c) result of local contrast stretching based on local statistics(Narendra et. al.), (d) result of local histogram equalization and (e) result of local contrast stretching following the algorithm due to Dorst.

(a)(i)

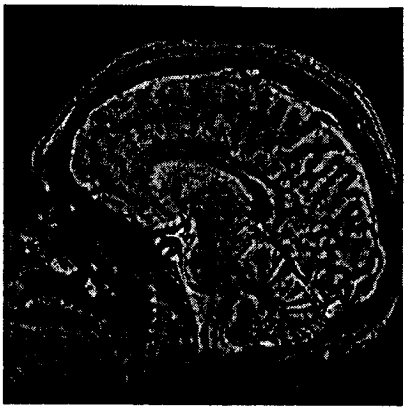

(a)(ii)

(a)(iii)

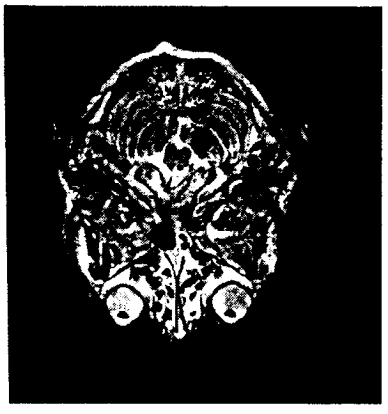

(b)(i)

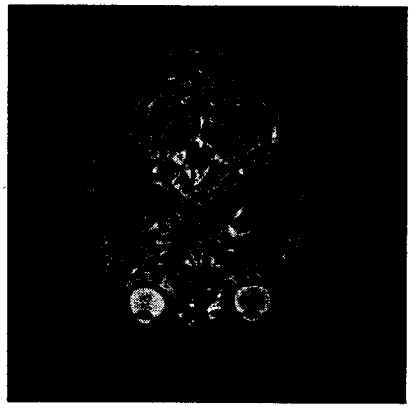

(b)(ii)

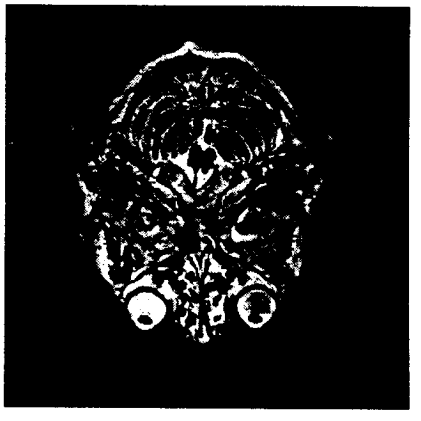

(b)(iii)

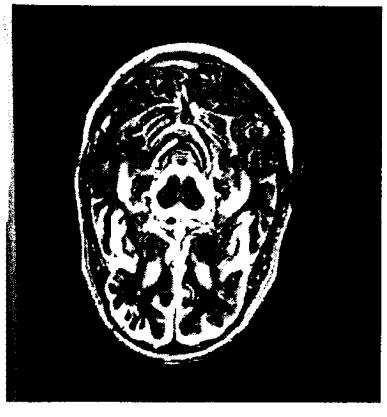

(c)(i)

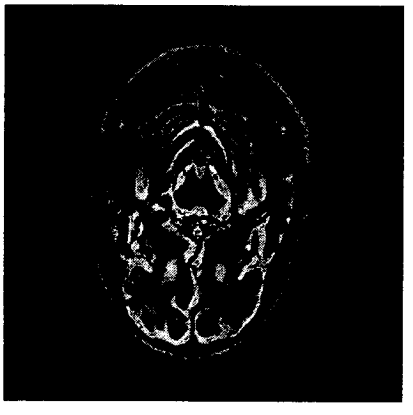

(c)(ii)

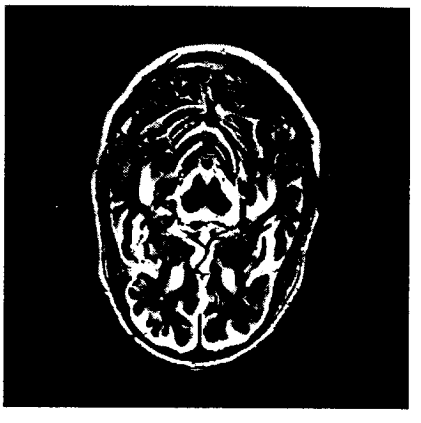

(c)(iii)

Figure 3.15: Results of contrast enhancement employing (i) multi-scale bright top-hat transformation, (ii) multi-scale dark top-hat transformation and (iii) both multi-scale bright and dark top-hat transformations (proposed method).

Table 3.9: Relative performance of the contrast enhancement schemes for gray-scale images

Image	Enhancement scheme						
	Original image	Local histogram equalization	Dorst's method	Narendra and Fitch's method	MMS-OPCL	MMS-OP	MMS-CL
Brain1	24.6340	120.3354	64.2656	69.7678	87.2719	85.5077	48.6729
Brain2	13.9994	158.4137	38.3279	29.6017	50.9438	54.7554	21.1697
Brain3	16.6238	110.0108	41.6203	32.4240	52.5211	48.1995	28.7884

MMS-OPCL: Multi-scale morphological scheme i.e. the proposed scheme. MMS-OP: multi-scale morphological scheme employing only opening. MMS-CL: multi-scale morphological scheme employing only closing.

hat transformation as compared to that employing only dark top-hat transformation. However, both the methods are biased to the type of feature. Therefore, combination of both bright and dark top-hat transformation would give better result in general which is also reflected in table 3.9.

3.7 Conclusion

In this chapter we have considered two basic enhancement problems: The noise smoothing and the local contrast enhancement. First, we propose a method for edge preserving smoothing of gray-scale images using multi-scale morphology. The method is based on modifying the intensity of scale-specific features present in the noisy image. The algorithm has been tested on sample images corrupted with var-

ious kinds of noise. The results have been compared with those of other standard methods. A comparative study of performance of various methods have been carried out through some standard performance metrics, like signal-to-noise ratio, deviation in mean busyness and correct processing ratio. It is found that the performance of the proposed method is satisfactory and in some cases superior to other methods referred in this chapter. The proposed method is then modified considering the noise. Then we have presented a scheme for local contrast enhancement of gray-level images using scale-space representation. The approach is exactly same as that of the noise smoothing except emphasis to features of various scale is given in reverse order to maintain conformity with the response of human visual system. Weights assigned to the different scale are chosen to avoid floating point operation during reconstruction. Here also, the results have been compared with those of few standard methods. The results due to the proposed method have been found reasonably satisfactory. However, the computational time and space required are high compared to other methods which the authors would like to improve subsequently.

The reasonably good performance of the proposed image enhancement schemes for graylevel images suggest the possibility of extending the scheme for enhancing the contrast of color images. In the next chapter we will see how this scheme may be extended to enhance the contrast of color images employing morphological tower.

Chapter 4

Local contrast enhancement of color image

4.1 Introduction

In this chapter we present a local contrast enhancement technique for color images employing morphological tower. Enhancing contrast of color images, is however, more difficult than enhancing the same for graylevel images. Unlike the gray-level images, each pixel of a color image is a 3-tuple consisting of red, green and blue components. The color enhancement requires enhancement of all three components. However, these three components can not be enhanced independent of each other. Therefore, the problem of color enhancement is to be tackled bit cleverly. In this work [115, 118], we have proposed a multi-scale approach employing morphological tower to enhance the contrast of a color image keeping the *hue* and *saturation* preserved.

The color vector at each pixel location of the image is used to compute the intensity. The intensity image so constructed is subjected to multi-scale enhancement. Prior

to this enhancement the direction cosines of the color vector at pixel location is preserved. Enhancement of the intensity image is performed employing morphological tower in the same way as described in chapter 3. The enhanced red, green and blue components are then obtained by combining the enhanced intensity image with the old direction cosines. The algorithm is tested on several color images and the results are compared with those of two other standard techniques. A performance measure based on the degree of contrast enhancement is also presented. A graphical plot showing the variation of this measure with the largest scale factor (i.e. the height of the tower) is also presented. The proposed morphological method preserves shape of the color-features, and their color attributes like hue and saturation. Like the previous problems, color enhancement also plays important roles in image processing. Several researchers have proposed methods for color enhancement and the works are cited in section 1.5.3.

Similar to the contrast enhancement of gray-scale images (chapter 3), here also, the image is made to undergo filtering for small number of low-valued scale factors . Hence, the issues like causality, edge localization, are not so stringent and hence the conventional opening and closing may be used instead of opening and closing by reconstruction respectively.

Rest of this chapter is as follows. Section 4.2 presents the proposed method in details. The underlying theory of the proposed color image enhancement is discussed in section 4.2.1. The discussion leads to a transformation of a hue preserving color enhancement using the intensity image. Section 4.2.2 presents the theoretical formulation of the proposed enhancement using multi-scale morphology. The effect of the proposed enhancement scheme on the color properties like hue, saturation and lightness is also presented here. Section 4.2.3 presents elaborately various steps of the implementational aspects of the proposed algorithm. Section 4.3 presents the experimental results of the proposed scheme. The experimental results also include

the outputs of other standard color enhancement schemes. A quantitative performance analysis is also provided to rate the efficacy of the proposed method. Finally, concluding remarks are cited in section 4.4.

4.2 Proposed method

The structure of a color image is first analysed from the point of view of optics. In the next subsection we propose a transformation which serves the purpose of color enhancement preserving the hue.

4.2.1 The Color Model

The intensity of reflected light following Phong's model [42] is given by

$$C^x(\lambda_n) = \{E_a(\lambda_n)T_aS_x(\lambda_n) + f_{attn}E_p(\lambda_n)[T_dS^x(\lambda_n)cos(\theta) + T_scos^m(\alpha)]\} \quad (4.1)$$

where

λ_n	$n-$ th sample of wavelength range
x	a location on the surface
$C^x(\lambda_n)$	intensity of emitting light in the direction of the viewer
$S^x(\lambda_n)$	surface reflectance at location x
$E_a(\lambda_n)$	intensity of ambient light
$E_p(\lambda_n)$	intensity of a point light source
T_p	ambient reflection coefficient
T_d	diffuse reflection coefficient
T_s	specular reflection coefficient

θ angle of incidence. Assumed to be constant for all x as the point is practically at infinity

α angle of viewer with respect to angle of specular reflection

m constant ≥ 1

In case of multi-sensor or multi-channel image acquisition system, if $R_k(\lambda_n)$ be the spectral sensitivity of the k-th receptor and ρ_k^x be the intensity recorded by the k-th receptor from the location x then

$$\begin{aligned}
\rho_k^x &= \Sigma_{n=1}^N \{E_a(\lambda_n)T_a S_x(\lambda_n)R_k(\lambda_n) + f_{attn}E_p(\lambda_n)[T_d S^x(\lambda_n)cos(\theta) + T_s cos^m(\alpha)]R_k(\lambda_n)\} \\
&= \Sigma_{n=1}^N E_a(\lambda_n)T_a S_x(\lambda_n)R_k(\lambda_n) + \Sigma_{n=1}^N f_{attn}E_p(\lambda_n)[T_d S^x(\lambda_n)cos(\theta)R_k(\lambda_n) + \\
&\quad \Sigma_{n=1}^N f_{attn}T_s cos^m(\alpha)]R_k(\lambda_n)\} \\
&= \rho_{a_k}^x + \rho_{d_k}^x + \rho_{s_k}^x \qquad (4.2)
\end{aligned}$$

The terms involving the wavelength λ_n may be expressed as combinations of orthogonal basis functions like *Fourier* or *Lagrange* basis of suitable dimensionality so that we may write

$$E_a(\lambda_n) = \Sigma_{i=1}^{D(E_a)} \epsilon_{a_i} \xi_i(\lambda_n) \qquad (4.3)$$

$$E_p(\lambda_n) = \Sigma_{i=1}^{D(E_p)} \epsilon_{p_i} \xi_i(\lambda_n) \qquad (4.4)$$

$$S^x(\lambda_n) = \Sigma_{i=1}^{D(S)} \sigma_i^x S_i(\lambda_n) \qquad (4.5)$$

For notational simplicity we may assume $D(E_a) = D(E_p) = D(S) = N$ where N is also equal to the number of wavelength sample points. The equations given above may be written in terms of product of matrices corresponding to N sample points of

λ as follows

$$\hat{E}_a = \begin{pmatrix} E_a(\lambda_1) \\ E_a(\lambda_2) \\ E_a(\lambda_3) \\ \dots \\ E_a(\lambda_i) \\ \dots \\ E_a(\lambda_N) \end{pmatrix} = \begin{pmatrix} \xi_1(\lambda_1) & \xi_2(\lambda_1) & \dots & \xi_N(\lambda_1) \\ \xi_1(\lambda_2) & \xi_2(\lambda_2) & \dots & \xi_N(\lambda_2) \\ \xi_1(\lambda_3) & \xi_2(\lambda_3) & \dots & \xi_N(\lambda_3) \\ \dots & \dots & \dots & \\ \xi_1(\lambda_i) & \xi_2(\lambda_i) & \dots & \xi_N(\lambda_i) \\ \dots & \dots & \dots & \\ \xi_1(\lambda_N) & \xi_2(\lambda_N) & \dots & \xi_N(\lambda_N) \end{pmatrix} \begin{pmatrix} \epsilon_{a1} \\ \epsilon_{a2} \\ \epsilon_{a3} \\ \dots \\ \epsilon_{ai} \\ \dots \\ \epsilon_{aN} \end{pmatrix} \tag{4.6}$$

$$\hat{E}_p = \begin{pmatrix} E_p(\lambda_1) \\ E_p(\lambda_2) \\ E_p(\lambda_3) \\ \dots \\ E_p(\lambda_i) \\ \dots \\ E_p(\lambda_N) \end{pmatrix} = \begin{pmatrix} \xi_1(\lambda_1) & \xi_2(\lambda_1) & \dots & \xi_N(\lambda_1) \\ \xi_1(\lambda_2) & \xi_2(\lambda_2) & \dots & \xi_N(\lambda_2) \\ \xi_1(\lambda_3) & \xi_2(\lambda_3) & \dots & \xi_N(\lambda_3) \\ \dots & \dots & \dots & \\ \xi_1(\lambda_i) & \xi_2(\lambda_i) & \dots & \xi_N(\lambda_i) \\ \dots & \dots & \dots & \\ \xi_1(\lambda_N) & \xi_2(\lambda_N) & \dots & \xi_N(\lambda_N) \end{pmatrix} \begin{pmatrix} \epsilon_{p1} \\ \epsilon_{p2} \\ \epsilon_{p3} \\ \dots \\ \epsilon_{pi} \\ \dots \\ \epsilon_{pN} \end{pmatrix} \tag{4.7}$$

$$\hat{S}_x = \begin{pmatrix} S^x(\lambda_1) \\ S^x(\lambda_2) \\ S^x(\lambda_3) \\ \dots \\ S^x(\lambda_i) \\ \dots \\ S^x(\lambda_N) \end{pmatrix} = \begin{pmatrix} s_1(\lambda_1) & s_2(\lambda_1) & \dots & s_N(\lambda_1) \\ s_1(\lambda_2) & s_2(\lambda_2) & \dots & s_N(\lambda_2) \\ s_1(\lambda_3) & s_2(\lambda_3) & \dots & s_N(\lambda_3) \\ \dots & \dots & \dots & \\ s_1(\lambda_i) & s_2(\lambda_i) & \dots & s_N(\lambda_i) \\ \dots & \dots & \dots & \\ s_1(\lambda_N) & s_2(\lambda_N) & \dots & s_N(\lambda_N) \end{pmatrix} \begin{pmatrix} \sigma_{a1} \\ \sigma_{a2} \\ \sigma_{a3} \\ \dots \\ \sigma_{ai} \\ \dots \\ \sigma_{aN} \end{pmatrix} \tag{4.8}$$

The spectral sensitivity of the k-th receptor at the point x is then given by

$$\begin{aligned} \rho^x_{a_k} &= \Sigma^N_{n=1} E_a(\lambda_n) T_a S^x(\lambda_n) R_k(\lambda_n) \\ &= T_a [E_a(\lambda_1) S^x(\lambda_1) R_k(\lambda_1) + E_a(\lambda_2) S^x(\lambda_2) R_k(\lambda_2) + \dots + \end{aligned}$$

$$
\begin{aligned}
& E_a(\lambda_n) S^x(\lambda_n) R_k(\lambda_n) \\
= \; & \hat{E}_a^T [R_k] \hat{S}^x
\end{aligned}
\tag{4.9}
$$

where

$$
[R_k] = \begin{pmatrix}
R_k(\lambda_1) & 0 & \dots & 0 & 0 \\
0 & R_k(\lambda_2) & \dots & 0 & 0 \\
0 & 0 & R_k(\lambda_3) & \dots & 0 \\
\dots & \dots & \dots & \dots & \dots \\
0 & 0 & \dots & R_k(\lambda_i) & 0 \\
\dots & \dots & \dots & \dots & \dots \\
0 & 0 & \dots & \dots & R_k(\lambda_N)
\end{pmatrix}
\tag{4.10}
$$

Thus, for a 3−receptor system the above equation may be written as

$$
\begin{pmatrix} \rho_{a_1}^x \\ \rho_{a_2}^x \\ \rho_{a_3}^x \end{pmatrix} = T_a \begin{pmatrix}
E_{a_1}(\lambda_1) R_1(\lambda_1) & E_{a_1}(\lambda_2) R_1(\lambda_2) & \dots & E_{a_1}(\lambda_N) R_1(\lambda_N) \\
E_{a_2}(\lambda_1) R_2(\lambda_1) & E_{a_2}(\lambda_2) R_2(\lambda_2) & \dots & E_{a_2}(\lambda_N) R_2(\lambda_N) \\
E_{a_3}(\lambda_1) R_3(\lambda_1) & E_{a_3}(\lambda_2) R_3(\lambda_2) & \dots & E_{a_3}(\lambda_N) R_3(\lambda_N)
\end{pmatrix} \begin{pmatrix} S^x(\lambda_1) \\ S^x(\lambda_2) \\ S^x(\lambda_3) \end{pmatrix}
\tag{4.11}
$$

Combining equations (4.8) and (4.11) we have,

$$
\hat{\rho}_a^x = T_a . \Lambda_{E_a} \hat{\sigma}^x \tag{4.12}
$$

where Λ_{E_a} is matrix obtained by multiplying the $3 \times N$ matrix of equation (4.11) with the $N \times N$ matrix of equation (4.8). Likewise for other components we have

$$
\hat{\rho}_d^x = T_d \Lambda_{E_p} \hat{\sigma}^x \tag{4.13}
$$

$$
\hat{\rho}_s^x = T_s \Lambda_{E_p} \hat{u} \tag{4.14}
$$

where $\hat{u}$ is a vector whose all elements are 1.

Let us assume that ambient light is generated mainly by repeated reflection of electromagnetic energy from the point light source. Then $\Lambda_{E_a} = \delta \Lambda_{E_p}$, where δ is a

constant. As a result the total response becomes

$$\begin{aligned}
\hat{\rho}^x &= \hat{\rho}_a^x + \hat{\rho}_d^x + \hat{\rho}_s^x \\
&= T\delta\Lambda_{E_p}\hat{\sigma}^x + \nu_2\Lambda_{E_p}\hat{\sigma}^x + \nu_3\Lambda_{E_p}\hat{u} \\
&= \nu_1\Lambda_{E_p}\hat{\sigma}^x + \nu_2\Lambda_{E_p}\hat{\sigma}^x + \nu_3\Lambda_{E_p}\hat{u} \\
&= (\nu_1 + \nu_2)\Lambda_{E_p}\hat{\sigma}^x + \nu_3\Lambda_{E_p}\hat{u} \\
&= \nu\Lambda_{E_p}\hat{\sigma}^x + \nu_3\Lambda_{E_p}\hat{u} \qquad (4.15)
\end{aligned}$$

Now, for a color image, we may look at the vector $\hat{\rho}$ as representing the intensity values corresponding to the *red, green* and *blue* colors at each pixel location as given below.

$$\hat{\rho}^x = \begin{pmatrix} R^x \\ G^x \\ B^x \end{pmatrix} \qquad (4.16)$$

From the above equation one may write

$$\begin{pmatrix} R^x \\ G^x \\ B^x \end{pmatrix} = \Lambda_E \left(\underbrace{\nu \begin{pmatrix} \sigma_1^x \\ \sigma_2^x \\ \sigma_3^x \end{pmatrix}}_{part1} \underbrace{+\nu_3 \begin{pmatrix} 1 \\ 1 \\ 1 \end{pmatrix}}_{part2} \right) \qquad (4.17)$$

Thus each response vector consists of two parts. First part depends on the property of object surface, hence is the main contributor to the hue information. Second part is a constant term and contributes to the saturation component of color. However, they together along-with the matrix multiplier determine the total intensity. The color image may be enhanced keeping its hue and saturation unaltered by multiplying the

right hand side of equation (4.17) as shown below.

$$\begin{pmatrix} \tilde{R}^x \\ \tilde{G}^x \\ \tilde{B}^x \end{pmatrix} = K^x \Lambda_E \left(\underbrace{\nu \begin{pmatrix} \sigma_1^x \\ \sigma_2^x \\ \sigma_3^x \end{pmatrix}}_{part1} \underbrace{+\nu_3 \begin{pmatrix} 1 \\ 1 \\ 1 \end{pmatrix}}_{part2} \right) \tag{4.18}$$

where $\tilde{R}^x$, $\tilde{G}^x$ and $\tilde{B}^x$ are the enhanced red, green and blue color component at location x and K^x is an amplification factor.

If x represents the actual location and $N(x)$ represents a predefined neighborhood of the location then the aim of the local contrast enhancement is to stretch the difference in the intensity values corresponding to x and $N(x)$. Let $\hat{\rho}^x$, $\tilde{\hat{\rho}}^x$ and $\hat{\rho}^{N(x)}$ represent the intensity vector at location x before and after contrast stretching, and the intensity vector in the neighborhood of location x respectively. The contrast may be improved by multiplying a function of intensity at a location with itself, where the function depends on the intensity at the location and that of its immediate neighborhood. Hence, the modified intensity would be

$$\tilde{\hat{\rho}}^x = f(\hat{\rho}^x, \hat{\rho}^{N(x)})\hat{\rho}^x \tag{4.19}$$

where $f(.)$ is a monotonic function such that

- $\|\hat{\rho}^x\| < \|\hat{\rho}^{N(x)}\|$ implies $\|\tilde{\hat{\rho}}^x\| \leq \|\hat{\rho}^{\tilde{N}(x)}\|$
- $\|\hat{\rho}^x\| > \|\hat{\rho}^{N(x)}\|$ implies $\|\tilde{\hat{\rho}}^x\| \geq \|\hat{\rho}^{\tilde{N}(x)}\|$
- $\|\tilde{\hat{\rho}}^x - \hat{\rho}^{\tilde{N}(x)}\| \geq \|\hat{\rho}^x - \hat{\rho}^{N(x)}\|$

In the next section we have developed a multi-scale morphological scheme for selecting a suitable function $f(.)$.

The red, green and the blue components at a pixel location x combine to yield the overall color sensation. In the rgb space this color is represented by a vector. The magnitude of this vector is given by

$$g^x = \|\rho^x\| = \sqrt{(R^x)^2 + (G^x)^2 + (B^x)^2} \tag{4.20}$$

The gray-level image constructed from its components is termed as *magnitude* or *intensity* image. In the next section the theory of the morphological multi-scale enhancement is developed starting with this magnitude image.

4.2.2 Theoretical formulation

The concept is already discussed in context to local contrast enhancement of gray-scale images. A major part of that concept is also utilized here.

The magnitude or the intensity image $g(r, c)$ is basically a gray-level image. The image may be looked upon as a combination of its scale-specific bright and dark features as suggested by equation 2.43 in chapter 2. The modified magnitude image after local contrast enhancement (see section 3.5) is expressed as

$$\tilde{g}(r,c) = \underbrace{g(r,c)}_{part1} + \underbrace{0.5\sum_{i=n}^{m} F_{iB}^{o}(r,c) - 0.5\sum_{i=n}^{m} F_{iB}^{c}(r,c)}_{part2} \tag{4.21}$$

where all the features, either dark of bright, smaller than scale n are assumed to be noise in the image.

Let us compare the equations (4.21) and (4.19). The part1 of equation (4.21) corresponds to the magnitude of the original color image at the location (r, c) (*i.e.* x) and is analogous to $\|\hat{\rho}^x\|$ of equation (4.19). The second part corresponds to the component $\|\hat{\rho}^{N(x)}\|$ of equation (4.19), where the neighborhood $N(x)$ is chosen in a multi-scale sense. Therefore, the contrast stretching function $f(.)$ of equation (4.19)

may be expressed as

$$f(\hat{\rho}^x, \hat{\rho}^{N(x)}) = \frac{\|\hat{\rho}^x + \hat{\rho}^{N(x)}\|}{\|\hat{\rho}^x\|} \tag{4.22}$$

The numerator $\|\hat{\rho}^x + \hat{\rho}^{N(x)}\|$ is now identical with $\tilde{g}(r,c)$ of equation (4.21). Therefore, the final stretched color image is given by

$$\begin{pmatrix} \tilde{R}^x \\ \tilde{G}^x \\ \tilde{B}^x \end{pmatrix} = \frac{\tilde{g}^x}{g^x} \begin{pmatrix} R^x \\ G^x \\ B^x \end{pmatrix} \tag{4.23}$$

The proposed multi-scale enhancement scheme, presented above preserves the color properties like hue and saturation of the image. Prior to proving this proposition, the color parameters hue, saturation and the lightness need to be defined.

We define h^x as

$$h^x = \begin{cases} 60 * \{\frac{G^x - B^x}{R^x - Min^x}\} & \text{if } R^x = Max^x \\ 60 * \{2 + \frac{B^x - R^x}{G^x - Min^x}\} & \text{if } G^x = Max^x \\ 60 * \{4 + \frac{R^x - G^x}{B^x - Min^x}\} & \text{if } B^x = Max^x \end{cases}$$

where

$$Min^x = minimum(R^x, G^x, B^x) \quad \text{and} \tag{4.24}$$

$$Max^x = maximum(R^x, G^x, B^x) \tag{4.25}$$

Finally, hue H is defined as

$$H^x = \begin{cases} h^x & \text{if } h^x \geq 0 \\ h^x + 360 & \text{if } h^x < 0 \end{cases}$$

The saturation and lightness are defined (respectively) as

$$Sat^x = \frac{Max^x - Min^x}{Max^x + Min^x} \tag{4.26}$$

$$Lit^x = Max^x \tag{4.27}$$

The object is to study the change in these parameters as a result of the execution of the proposed algorithm on the color image. Now, the hue of the enhanced image is obtained by replacing the red, green and blue components by their respective enhanced values as given by equation (4.23). The modified hue $\tilde{h}^x$ is given by

$$\tilde{h}^x = \begin{cases} 60 * \{\frac{\tilde{G}^x - \tilde{B}^x}{\tilde{R}^x - \tilde{Min}^x}\} & \text{if } \tilde{R}^x = \tilde{Max}^x \\ 60 * \{2 + \frac{\tilde{B}^x - \tilde{R}^x}{\tilde{G}^x - \tilde{Min}^x}\} & \text{if } \tilde{G}^x = \tilde{Max}^x \\ 60 * \{4 + \frac{\tilde{R}^x - \tilde{G}^x}{\tilde{B}^x - \tilde{Min}^x}\} & \text{if } \tilde{B}^x = \tilde{Max}^x \end{cases}$$

Now substituting $\tilde{R}^x = \alpha R^x$, $\tilde{G}^x = \alpha G^x$ and $\tilde{B}^x = \alpha B^x$, where $\alpha = \frac{\tilde{g}^x}{g^x}$, we get

$$\tilde{h}^x = \begin{cases} 60 * \{\frac{\alpha G^x - \alpha B^x}{\alpha R^x - \alpha Min^x}\} & \text{if } \tilde{R}^x = \tilde{Max}^x \\ 60 * \{2 + \frac{\alpha B^x - \alpha R^x}{\alpha G^x - \alpha Min^x}\} & \text{if } \tilde{G}^x = \tilde{Max}^x \\ 60 * \{4 + \frac{\alpha R^x - \alpha G^x}{\alpha B^x - \alpha Min^x}\} & \text{if } \tilde{B}^x = \tilde{Max}^x \end{cases}$$

Dividing both the numerator and the denominator by α we get $\tilde{h}^x = h^x$ i.e. the hue is preserved after enhancement. Proceeding in the same way it may be shown that

$$\begin{aligned} \tilde{Sat}^x &= Sat^x \text{ and} \\ \tilde{Lit}^x &= \alpha Lit^x \end{aligned}$$

In this contrast enhancement technique, the color vector at each pixel location is either stretched or contracted along its own direction depending on whether it is found to contribute as bright or dark feature. This is illustrated in fig. (4.2).

4.2.3 Implementation

The implementation of equation (4.21) describing feature based local contrast enhancement involves construction of a number of morphological towers as elaborated below.

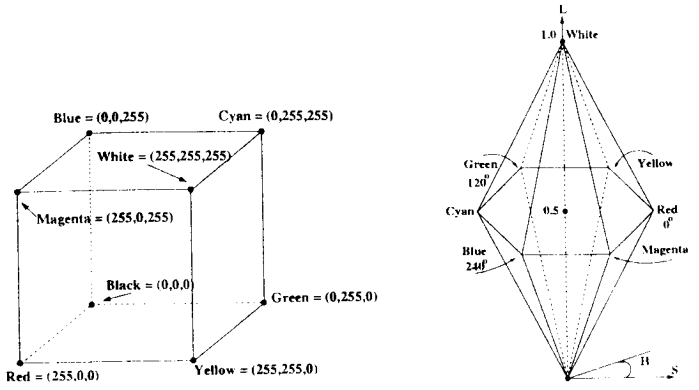

(a) (b)

Figure 4.1: Two widely used color models (a) RGB and (b) HLS model

- **Construction of the magnitude image**

  The color image to be enhanced is used to construct the magnitude image for use in the subsequent steps. The magnitude image is constructed by taking the square root of the sum of the squares of the red, green and blue intensity values at each pixel location. The angles or the direction cosines of the three color components at each pixel location are saved for future use.

  The following three steps are same as in case of contrast enhancement of graylevel images (section 3.5.3 in chapter 3).

- **Construction of Morphological Towers**

  The image to be enhanced is subjected to a sequence of gray-scale morphological opening operations with a disk structuring element and its higher order homothetics. The resulting sequence of images are kept in a stack called the *opening tower* as shown in the fig. (4.3). An identical tower, called closing tower, is constructed with the sequence of the images resulting from multi-scale closing of the input image. Thus the i-th entry in the opening (closing) tower contains the image opened(closed) with the structuring element iB.

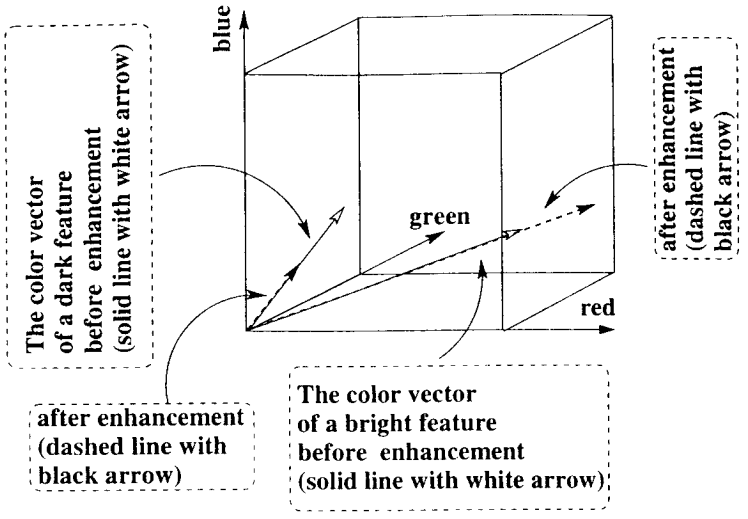

Figure 4.2: Color contrast enhancement in rgb space

- **Construction of difference Towers**

  Each image of the opening tower is subtracted individually from the original image and the resulting bright feature images are then kept in another tower called the *difference tower*. An identical difference tower is constructed for the dark feature images obtained by subtracting the original image from each entry of the closing tower. Therefore the i-th image in the difference tower for opening (closing) consists of bright (dark) features which are smaller than or equal to iB.

- **Construction of the enhanced magnitude image**

  For reconstructing the final image we do the following :

  - We sum up all the entries in the difference tower corresponding to the opening operation. This results in an image consisting of bright features of all possible scales of interest that are present in the original image.

$$S^o(r,c) = \sum_{i=1}^{n} F^o_{iB}(r,c) \tag{4.28}$$

  The summation, here, denotes pixel-wise sum of n images.

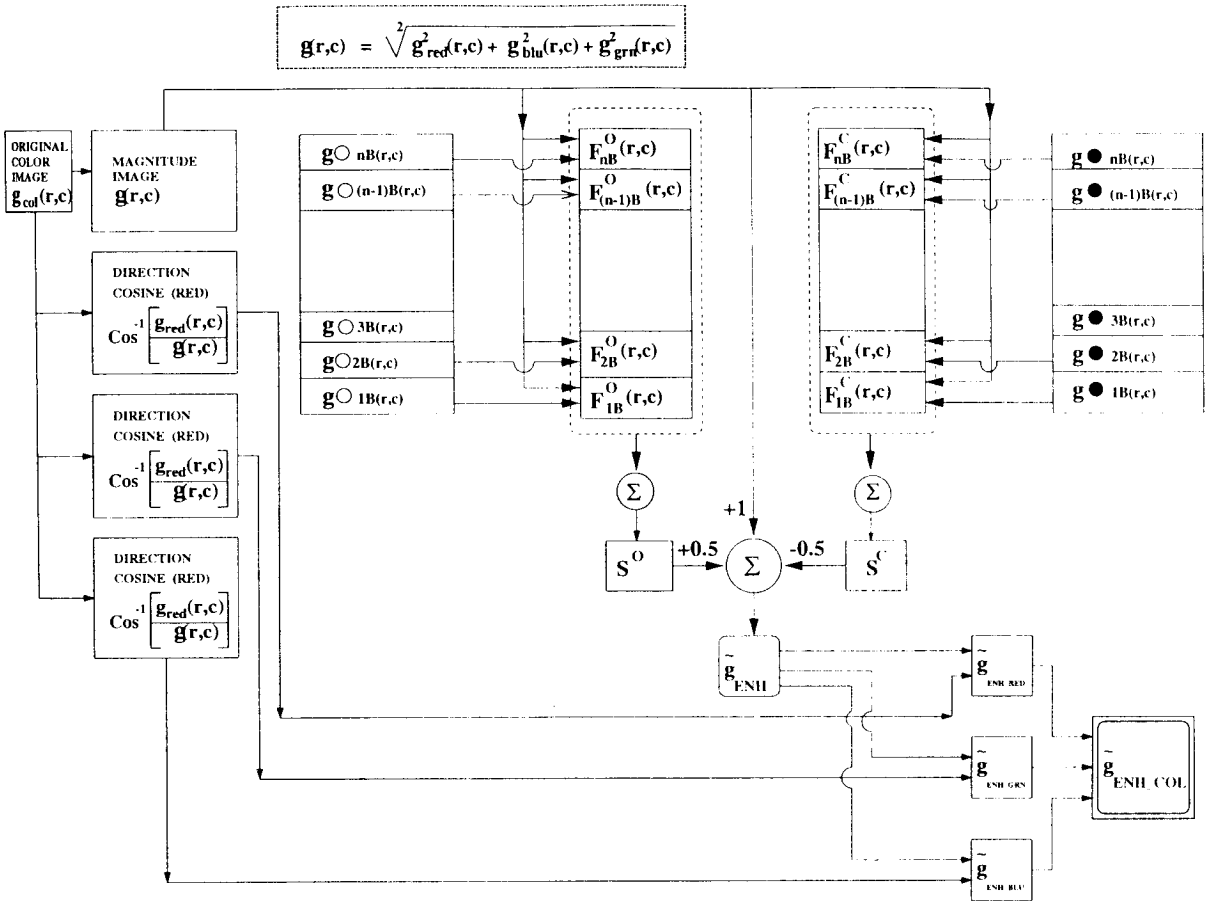

Figure 4.3: Scheme for color image enhancement using morphological towers

– We perform the same operation on the difference tower corresponding to the closing operation. This results in an image consisting of dark features of all scales of interest that are present in the original image.

$$S^c(r,c) = \sum_{i=1}^{n} F_{iB}^c(r,c) \tag{4.29}$$

Finally, the locally enhanced magnitude image is obtained by combining three images as given by

$$\tilde{g}(r,c) = g(r,c) + 0.5S^{op}(r,c) - 0.5S^{cl}(r,c) \tag{4.30}$$

The '+' and '-' operations are applied between corresponding pixels of three different images.

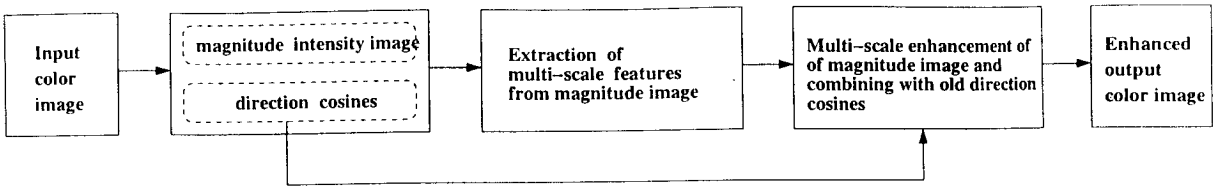

Figure 4.4: Passes of the local contrast enhancement algorithm

- **Construction of the enhanced color image**

  The enhanced magnitude image obtained in the previous step and the direction cosine information about the red, green and blue preserved in the first step are used to construct the enhanced red, green and blue components by taking the projections on respective axes. The final enhanced color image is obtained by combining these enhanced red, green and blue components. This follows from equation (4.23) as given below.

$$\begin{pmatrix} \tilde{R}^x \\ \tilde{G}^x \\ \tilde{B}^x \end{pmatrix} = \tilde{g}^x \begin{pmatrix} \frac{R^x}{g^x} \\ \frac{G^x}{g^x} \\ \frac{B^x}{g^x} \end{pmatrix} \tag{4.31}$$

  Now the ratio $\frac{R^x}{g^x}$ is basically the *direction cosine* of the color vector at location x with respect to the *red* axis and may be written as $\cos(\theta_r^x)$. Thus equation (4.31) may be written as

$$\begin{pmatrix} \tilde{R}^x \\ \tilde{G}^x \\ \tilde{B}^x \end{pmatrix} = \tilde{g}^x \begin{pmatrix} \cos(\theta_r^x) \\ \cos(\theta_g^x) \\ \cos(\theta_b^x) \end{pmatrix} \tag{4.32}$$

The algorithm for multi-scale color image enhancement consisting of three parts as shown in fig. 4.4 are given below.

Formation of magnitude image

Procedure *Extract_rgb_components()*

input: $g_{in}[][]$; /* the original input rgb image */

output: $g_{red}^{dc}[][]$, $g_{grn}^{dc}[][]$, $g_{blu}^{dc}[][]$, $g_{mag}[][]$ /* matrices to record the direction cosines and the magnitude of the color vector */

var: $g_{red}[][]$, $g_{grn}[][]$, $g_{blu}[][]$; /* intermediate images */

begin

$g_{red}[][] \leftarrow Red\_component(g_{in})$;

$g_{grn}[][] \leftarrow Green\_component(g_{in})$;

$g_{blu}[][] \leftarrow Blu\_component(g_{in})$;

$g_{mag}[][] \leftarrow Square\_root((g_{red}[][]*g_{red}[][]) + (g_{grn}[][]*g_{grn}[][]) + (g_{blu}[][]*g_{blu}[][]))$;

$g_{red}^{dc}[][] \leftarrow g_{red}[][]/g_{mag}[][]$;

$g_{grn}^{dc}[][] \leftarrow g_{red}[][]/g_{mag}[][]$;

$g_{blu}^{dc}[][] \leftarrow g_{red}[][]/g_{mag}[][]$;

end begin

end Procedure

Extraction of multi-scale features

Procedure *Extract_multi-scale_features()*

input: $g_{mag}[][]$; /* the original input magnitude image */

output: bright_feature_tower, dark_feature_tower; /* towers of filtered images */

constant: $MAXSCALE$; /* upper bound of scale factor */

var: $g_{op}[][]$, $g_{cl}[][]$; /* intermediate images */

var: $g_i^{top}[][]$, $g_i^{bot}[][]$; /* intermediate images */

integer: i;

$i \leftarrow 1$;

begin

repeat

$g_{op} \leftarrow morph\_open\_with\_circular\_se(g_{mag}, iB)$;

$g_i^{top} \leftarrow g_{mag} - g_{op}$;

$insert\_in\_tower(g_i^{top}, bright\_feature\_tower, i)$;

$g_{cl} \leftarrow morph\_close\_with\_circular\_se(g_{mag}, iB)$;

$g_i^{bot} \leftarrow g_{cl}$ - g_{in};

$insert\_in\_tower(g_i^{bot}, dark\_feature\_tower, i)$;

$increase\ i$;

until $i > MAXSCALE$;

end begin

end Procedure

Formation of enhanced color image

Procedure *Combine_multi-scale_feature_images()*

input: bright_feature_tower, dark_feature_tower; /* towers of filtered images */

input: $g_{red}^{dc}[][], g_{grn}^{dc}[][], g_{blu}^{dc}[][]$ /* the input direction-cosines matrices */

input: $g_{mag}[][]$ /* the input magnitude image */

output: $g_{rgb\_enh}[][]$; /* the output enhanced rgb image */

var: $g_{mag\_enh}[][], g_{temp}, g_{btemp}[][], g_{dtemp}[][]$; /* intermediate images */

constant: $MAXSCALE$; /* upper bound of scale factor */

integer: i;

$i \leftarrow 1$;

$g_{mag\_enh}[][] \leftarrow g_{mag}[][]$;

begin

repeat

$g_{temp} \leftarrow get\_image\_from(bright\_feature\_tower, i)$;

$g_{btemp} \leftarrow g_{btemp} + g_{temp}$;

$g_{temp} \leftarrow get\_image\_from(dark\_feature\_tower, i)$;

$g_{dtemp} \leftarrow g_{dtemp} + g_{temp}$;

$increase\ i$;

until $i > MAXSCALE$;

end begin

$g_{mag\_enh}[][] \leftarrow g_{mag}[][] + 0.5 * g_{btemp}$ - $0.5 * g_{dtemp}$

$g_{rgb\_enh}[][] \leftarrow Construct\_rgb(g_{mag\_enh}[][], g^{dc}_{red}[][], g^{dc}_{grn}[][], g^{dc}_{blu}[][])$;

end Procedure

4.3 Experimental results and discussion

The proposed algorithm has been tested on a set of color images and the results have been compared with that of other methods [see figs. (4.6-4.9)]. Here we present the results with four real images shown in figs. [(4.6-4.9)](i). Fig 4.5(a) shows a color image which is enhanced using conventional histogram equalization. The result [see fig. 4.5(b)] reflects the in-applicability of the enhancement technique due to change of hue. Results of the proposed algorithm are shown in figs. [(4.6-4.9)](iv). In the experiment we have used $n = 1$ (as the images are assumed to be noise-free), $m = 5$ and B is a circular disk of radius 1 so as to get visually optimum results. That means largest SE used is disk of radius 5. The value of m can be made larger depending on demand or precision. However, it should be noted that very large value of m will not give noticeable improvement in the output since the feature images of progressively larger scales have gradually smaller weightages in enhancing the image. Moreover, very large value of m, in spite of incorporating generality in the scheme, increases the computational time unnecessarily.

The resulting images are seen to have more contrast than the respective original versions without any effect on the color content. The results of the proposed scheme are compared with those of two other methods namely (i) the multi-scale pyramidal approach of Toet [see figs. (4.6-4.9)(ii)] and (ii) the method employing genetic algo-

rithm [see figs. (4.6-4.9)(iii)] due to [144]. Brief descriptions of these two methods are given below.

Multi-scale color image enhancement due to Toet [156]

In this work, the color image is first converted from its RGB to HLS [fig. 4.1] representation. The luminance and the saturation images are employed for the contrast enhancement of the color image. The luminance and saturation contrast primitives at each scale are examined by constructing pyramids at each scale. A new set of multi-scale luminance contrast primitives is constructed by modulating the original luminance contrast primitives at each scale using the saturation contrast primitives at that scale. The method involves construction of pyramids of luminance and saturation images for both down and up-sampling, and, for the implementation, the rectangular input rgb images were padded by "0" pixel values to make the image height and width same and equal to the nearest integral power of 2. The parameter used in the experiment are chosen according to the specifications given in the article. For a greater detail [156] may be referred. Finally enhanced version of the luminance component along-with its original version are used to construct the enhanced rgb version of the image.

Color image enhancement employing genetic algorithm due to Shyu et. al. [144]

In this work too, the color image is first converted from its RGB to HLS representation. The luminance component is intended to undergo four types of contrast enhancement and the contribution of each component is realized in terms of normalized multiplier constants $\omega_1, \omega_2, \omega_3$ and ω_4. The four types of contrast stretching methods for the luminance image are also characterized by five parameters $p_1, p_2 \ldots p_5$ as expressed by the following equations. The saturation component is made to undergo a transformation involving incomplete beta-gamma function characterized by

two more parameters α and β.

$$T_1(l_{x,y}) = \frac{1}{p_1} ln[1 + \exp^{(p_1-1)} l_{xy}] \tag{4.33}$$

$$T_2(l_{x,y}) = \frac{1}{p_2}[(1+p_2)^{l_{xy}} - 1] \tag{4.34}$$

$$T_3(l_{x,y}) = \frac{1}{1 + [\frac{(l_{max} - l_{xy})}{p_3}]^{p_4}} \tag{4.35}$$

$$T_4(l_{x,y}) = \frac{p_3}{l_{max}} \frac{1}{(\frac{l_{max}}{l_{xy}} + p_5 - 1)^{p_4}} \tag{4.36}$$

The luminance and the saturation images are modified using the following equations

$$l'_{x,y} = \omega_1 T_1(l_{x,y}) + \omega_2 T_2(l_{x,y}) + \omega_3 T_3(l_{x,y}) + \omega_4 T_4(l_{x,y}) \tag{4.37}$$

$$s'_{x,y} = \int_0^{s_{xy}} \frac{t^{\alpha-1}(1-t)^{\beta-1}}{B(\alpha,\beta)} dt \tag{4.38}$$

The eleven parameters are estimated using genetic algorithms. In this experiment, the total length of each chromosome has been taken as 88 while the number of iterations are limited to 50. The details of the original work is available in [144]. Finally the luminance and the saturation component corresponding to the best-fit parameters are used to construct the *rgb* version of the enhanced image. The standard algorithms for inter-conversion of *rgb* and *hls* formats are available in [42]

4.3.1 Performance analysis

For a quantitative assessment of the degree of enhancement performed by the methods we have defined the *overall contrast* as follows. First, we compute the average value of the difference of the maximum and minimum pixel value (i.e. local contrast) over a 3×3 mask for the individual color components.

$$d\_red(r,c) = \Sigma_{p=r-1}^{r+1} \Sigma_{q=c-1}^{c+1} [max\_red - min\_red]$$

$$avg\_red = \frac{1}{MN} \Sigma_{r=0}^{M-1} \Sigma_{c=0}^{N-1} d\_red(r,c)$$

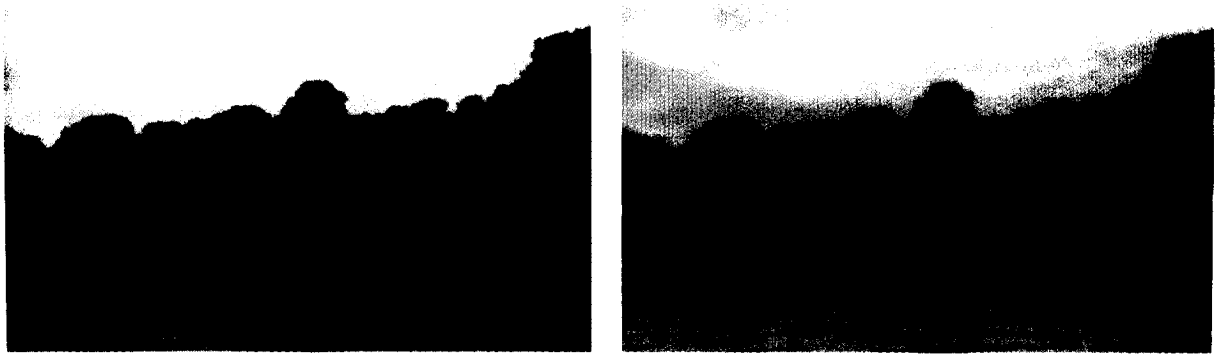

(a) (b)

Figure 4.5: (a) Original color image (b) histogram stretching of the original color image

$$
\begin{aligned}
d\_grn(r,c) &= \Sigma_{p=r-1}^{r+1}\Sigma_{q=c-1}^{c+1}[max\_grn - min\_grn] \\
avg\_grn &= \frac{1}{MN}\Sigma_{r=0}^{M-1}\Sigma_{c=0}^{N-1}d\_grn(r,c) \\
d\_blu(r,c) &= \Sigma_{p=r-1}^{r+1}\Sigma_{q=c-1}^{c+1}[max\_blu - min\_blu] \\
avg\_blu &= \frac{1}{MN}\Sigma_{r=0}^{M-1}\Sigma_{c=0}^{N-1}d\_blu(r,c)
\end{aligned}
$$

The overall contrast is defined as the minimum of the average contrasts of the three color components as given below.

$$Cont = min(avg\_red, avg\_grn, avg\_blu) \tag{4.39}$$

The overall contrast is computed for the original color image and the enhanced images resulting from all the enhancement schemes. From the table it is evident that the overall contrast is the best for the proposed method.

The variation of the overall contrast with the largest scale factor n (i.e. the height of the towers) for all four test images are shown in fig. (4.10). The overall contrast in each case is found to increase with scale, attain a saturation. As we for higher and higher scale we add more and more top-hat images of increasing scale. The proportion of the

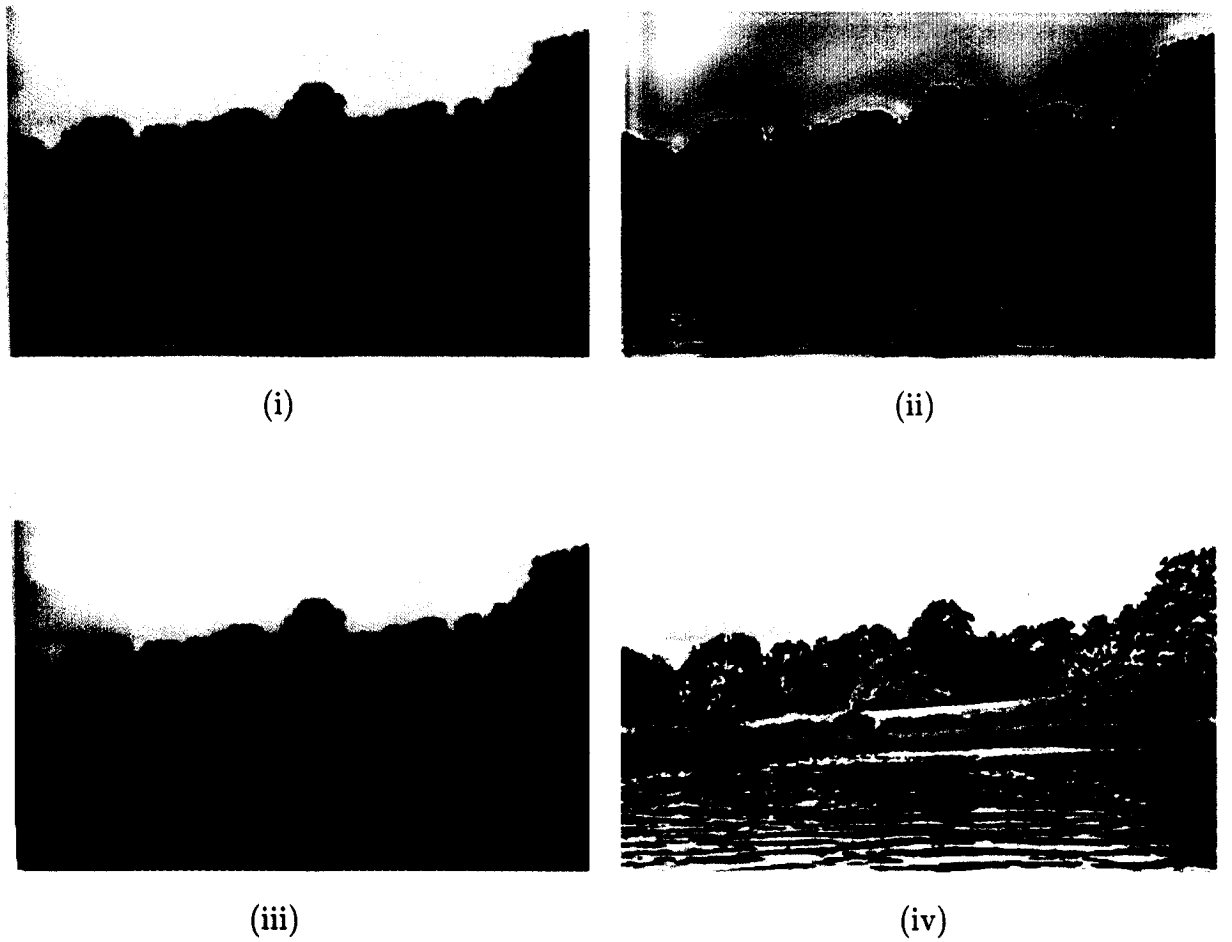

Figure 4.6: Results (i) Original image (ii) local contrast stretching using multi-scale pyramid(Toet) (iii) local contrast stretching based on genetic algorithm (iv) local contrast stretching using multi-scale morphology

(i)

(ii)

(iii)

(iv)

Figure 4.7: Results (i) Original image (ii) local contrast stretching using multi-scale pyramid(Toet) (iii) local contrast stretching based on genetic algorithm (iv) local contrast stretching using multi-scale morphology

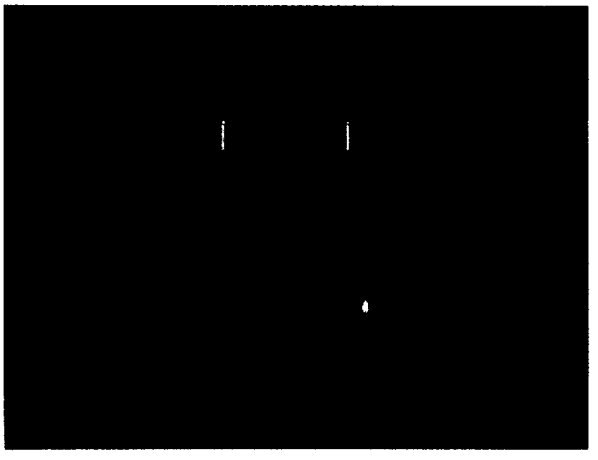

(i)

(ii)

(iii)

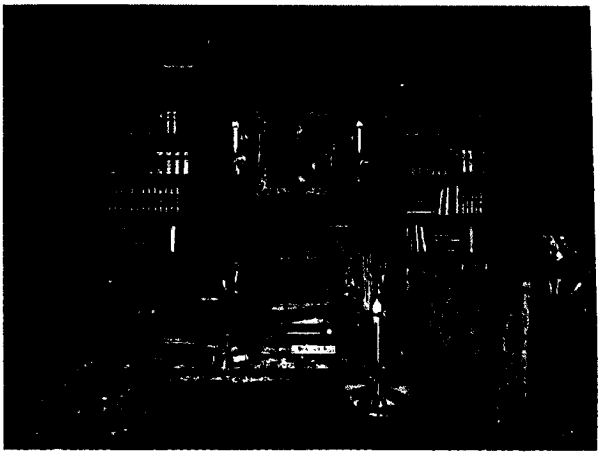

(iv)

Figure 4.8: Results (i) Original image (ii) local contrast stretching using multi-scale pyramid(Toet) (iii) local contrast stretching based on genetic algorithm (iv) local contrast stretching using multi-scale morphology

(i)

(ii)

(iii)

(iv)

Figure 4.9: Results: (i) Original image (ii) local contrast stretching using multi-scale pyramid(Toet) (iii) local contrast stretching based on genetic algorithm due to Shyu et. al. (iv) local contrast stretching using multi-scale morphology

Table 4.1: Relative performance of the contrast enhancement schemes for color images

Image	Enhancement scheme			
	Original image	Toet's pyramidal scheme	Shyu's Genetic algorithm	MMS
Garden	17.772835	36.173661	18.657312	72.822688
Flowers	30.241696	40.886359	30.110354	84.185133
Library	21.473958	69.872317	46.413833	74.809492
Pond	43.782650	62.703967	48.497008	113.058342

MMS: Multi-scale morphological scheme

features of smaller scale increases gradually. Hence the overall contrast increases. The dynamic range of the intensity is however, limited to the range of $0 - 255$. Therefore, executing the proposed algorithm for a very large scale factor does not give rise to appreciable improvement in the contrast. The curve is even found to fall down at large scale factor for the image of fig. 4.8(i). Pixel values at some localities in such cases go beyond the minimum or maximum value and hence clipped to the minimum or maximum value. As a result the intensity pattern at those localities become flat like a plateau. Hence there is a gross demotion in the overall contrast value.

4.4 Conclusion

In this chapter we have proposed a scheme for local contrast enhancement of color images. The red, green and blue color components of the image under study are used to construct the magnitude (i.e. the intensity) image. For each pixel, the direction cosines corresponding to the primary colors in the rgb space are preserved for future use. The method employs multi-scale morphological filtering in extracting

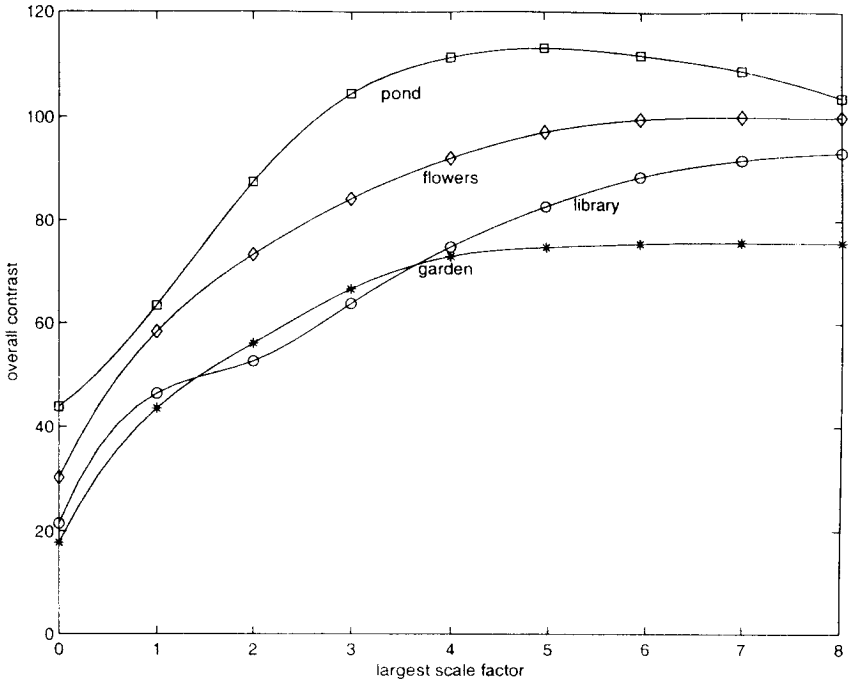

Figure 4.10: Variation of the overall contrast with the largest scale factor

the scale specific dark and bright features from the input magnitude image through the implementation of a number of *towers*. The recombination of all such features at the time of reconstruction emphasizes on the basic requirement of local contrast enhancement which demands that features of progressively smaller scales should get more weights. The enhanced red, green and blue components are obtained by combining the enhanced magnitude image with the original direction cosine information preserved previously. A simple example in one dimension is provided to clarify the functionality of the algorithm. The scheme has been implemented and executed on a set of color images. The results have been compared with those of two standard methods. The results due to the proposed method have been found to be reasonably satisfactory. The proposed method while performing enhancement preserves the color attributes namely hue and saturation. The proposed multi-scale method takes care of color, shape and scale simultaneously and it is inherently parallel.

So far, we have presented the works related to the applications of morphological towers in low level pixel processing like image enhancement (noise smoothing and contrast enhancement) on graylevel and color images. The schemes are found reasonably successful. In the next two chapters we will present two more works related to higher level image processing. In the next chapter we present a multi-scale feature-based fusion scheme for multimodal images employing morphological tower.

Chapter 5

Multimodal image fusion

5.1 Introduction

Another important application of morphological tower discussed in this chapter is multimodal image fusion. As discussed in chapter 1, fusion is a process of integrating salient features from a number of modalities into a single synthesized image. Fusion is also a very widely used technique in image processing and there exists several methods for image fusion (see section 1.5.4). The information content in the synthesized or fused image is expected to more than that contained in respective modalities. In this chapter we have presented a technique of multimodal image fusion for $2D$ images [114, 30]. The images participating in the process of fusion are first mutually registered. The registration employed in this work is landmark point based supervised method based on *affine* transformation. After the registration the multimodal images are subjected to a multi-scale feature extraction operation. In this feature-based multi-scale fusion scheme, the scale-specific bright and dark features extracted from the individual modality are stacked in morphological towers. Finally, the construction of

the fused image involves integrating the scale-specific features from all the modalities. In this process we select that particular feature which is best represented in at least one of the modalities. The developed scheme is applied to fuse MR and CT images of brain and the result is compared with fused images generated by other existing fusion schemes. Quantitative performance measures are also provided for comparison among the methods.

The chapter is organized as follows. Section 5.2 discusses a point-based method of image registration adopted as a preprocessing step prior to fusion. The theoretical aspects of the proposed multi-scale morphological scheme for fusing multimodal images and its implemenational details using morphological towers are presented in section 5.3. This is followed by section 5.4 containing the experimental results and discussions. Concluding remarks are cited in section 5.5.

5.2 Registration

Any kind of image fusion method involves registration as a first and foremost step. In general, different sensors respond to scene characteristics in different and, partially, complementary ways. In a multi-sensor image acquisition system, the size, orientation and location of an object relative to its own background may not be identical in all the images of different modalities. Integration or fusion of multi-sensor information is possible only if the images are registered or positioned with respect to a common coordinate system [143]. Image registration (in case of fusing two images) is the process of determining correspondence between all points in two images of the same scene or object. There are various techniques for registering multimodal images [25]. Some of which are area based while some are point based. Point based methods [11, 34] are simpler and more common. These points, i.e. GCPs, are basically spatial

features (e.g., corners, junctions, centroid of blobs, etc.) present in the image. The GCPs can be made available by applying standard feature extraction algorithms [108]. Brown [25] made a good survey on image registration.

In a point based registration scheme a set of GCPs is selected from the images, correspondence is established between them, and from that point correspondence a transformation function is determined. Linear methods use either the affine transformation or the geometric transformation like translation, rotation and scaling so as to minimize the distance measure or to maximize the similarity between these points [55]. Finally, this transformation function is used to map points in one image to points in the other. Considering fusion of two images, if (u, v) represents the coordinate of GCP in the first image on which the second image is intended to be mapped using affine transformation, the following set of equations may be used

$$x = au + bv + c \tag{5.1}$$

$$y = du + ev + f \tag{5.2}$$

where a, b, c, d, e and f are the characteristic parameters of the transformation The values of the parameters are estimated using knowledge of coordinates of a set of GCPs. At least three pairs of such points are required for estimating the parameters, but for enhancing accuracy we make use of n pairs ($n > 3$) of GCPs. The parameters a, b, c, d, e and f are then estimated by the method of least squares.

Note that in this approach more emphasis is given to one of the images in reconfiguring the position of the object(s), and hence it is biased. In this work we have adopted a point based method for registering the multimodal images in which we have given equal emphasis to both the images. Two sets of ground control points from two images are selected. The target image coordinate system is assumed to be intermediate between the given images. Both the images are rotated, scaled and translated in opposite sense so that the corresponding GCPs come closer. We use two affine trans-

formations determined based on these GCPs and following the treatment suggested by Mardia et. al. [93, 92] are applied on corresponding images. Thus the adopted method is unbiased to both the images. The parameters of the transformation(s) are determined through exhaustive search for the minimum error.

5.3 Proposed method

5.3.1 Theoretical formulation

We propose a multi-scale morphological method of fusing two images of same objects obtained through two different modalities. As pointed out earlier, the individual images in a multi-sensor image acquisition system do not contain each and every feature with equal clarity. Some features are detected with very good clarity while some are not. The basic idea behind fusing a number of images is to pick up the features that are best represented in any of the modalities and to recombine them to form the composite image. The features at each scale from the respective modalities are extracted using top-hat transformation. In this work, we have made use of conventional multi-scale morphological filters rather than filters by reconstruction.

As presented in chapter 2, the image resulting from the kth modality can be expressed in terms of its scale-specific bright and dark features as

$$g_k(r,c) = g_k^{smooth}(r,c) + \frac{1}{2}\sum_{i=1}^{n} F_{iBk}^{o}(r,c) - \frac{1}{2}\sum_{i=1}^{n} F_{iBk}^{c}(r,c) \tag{5.3}$$

where g_k^{smooth} is obtained by smoothing the image at scale n. It is basically the average of the images opened and closed with the SE at the largest scale n. For the image of k-th modality, F_{iBk}^{o} and F_{iBk}^{c} represent the images containing the bright and dark

features respectively at scale i as given below.

$$F^{o}_{iBk}(r,c) = (g_k \circ (i-1)B)(r,c) - (g_k \circ iB)(r,c) \tag{5.4}$$

$$F^{c}_{iBk}(r,c) = (g_k \bullet iB)(r,c) - (g_k \bullet (i-1)B)(r,c) \tag{5.5}$$

where, as usual, B is a point set representing convex structuring element of a definite shape while i is an integer representing the scale factor of the structuring element.

All the individual images in a multi-sensor image acquisition system may be expressed using equation (5.3). For constructing the fused image, we choose the best feature corresponding to each scale. Therefore, the fused image can be expressed as

$$\begin{aligned} g_{fuse}(r,c) = & \underbrace{avg\{g_1^{smooth}(r,c), g_2^{smooth}(r,c), \ldots g_m^{smooth}(r,c)\}}_{part1} \\ & + \underbrace{\frac{1}{2}\sum_{i=1}^{n} max\{F^{o}_{iB1}(r,c), F^{o}_{iB2}(r,c), \ldots F^{o}_{iBm}(r,c)\}}_{part2} \\ & - \underbrace{\frac{1}{2}\sum_{i=1}^{n} max\{F^{c}_{iB1}(r,c), F^{c}_{iB2}(r,c) \ldots F^{c}_{iBm}(r,c)\}}_{part3} \end{aligned} \tag{5.6}$$

The part1 of equation (5.6) presents the baseimage which comprises of relatively large regions of nearly constant intensity. This serves the purpose of a substrate over which the features are erected or scooped depending on whether the feature is bright or dark. The part2 and part3 are the scale-specific bright and dark features that are best represented in different modalities. The algorithm is clarified with a simple example in one dimension in the following subsection. This is followed by an elaborate description regarding the implementation of the proposed scheme using morphological towers.

5.3.2 A simple illustration in one-dimension

For a better understanding of the fusion scheme we first elaborate it in the context of one-dimensional functions as shown in Fig. 5.1. Fig. 5.1 provides a simplified illustration of the proposed strategy. Here we intend to fuse two functions $f_1(t)$ and $f_2(t)$. Both the functions $f_1(t)$ and $f_2(t)$ have salient features manifested by *crests* and *troughs* of different height (*or depth*) and width located at different position. We use a line segment L of unit length and its higher order dilates kL (where $k = 1, 2, 3..$) as structuring elements (SE) for extracting the salient features from both the functions as described below

- Opening by kL removes the crests narrower than length k from both the functions.
- The function $g_k^{O1}(t) = (f_1(t) \circ (k-1)L - f_1(t) \circ kL)$ contains the crests (see *fig.* 5.1) of $f_1(t)$ which are narrower than k but wider than $(k-1)$. Similarly, the function $g_k^{O2}(t) = (f_2(t) \circ (k-1)L - f_2(t) \circ kL)$ contains only the crests of $f2(t)$ which are narrower than k but wider than $(k-1)$.
- The function $h_k^O(t) = max(g_k^{O1}(t), g_k^{O2}(t))$ constructed by comparing $g_k^{O1}(t)$ and $g_k^{O2}(t)$ at each sample point t contains the crests from both $f_1(t)$ and $f_2(t)$. Thus the crests of width lying in between $(k-1)$ and k coming from $f_1(t)$ and $f_2(t)$ are combined in the function $h_k^O(t)$.

The function $S_{op}(t)$ constructed by superposing *(or, simply adding)* the functions $h_k^O(t)$ for $k = 1, 2, 3..$ contains all the crests of both the functions.

The same set of operations with closing helps us extract the troughs from both the functions and combine them into a single function $S_{cl}(t)$.

Opening the functions with the largest homothetic of the SE L (i.e. kL) removes all the crests from the functions leaving only their locally non-varying parts. While combining we must avoid clipping the highest crests. We therefore consider the minimum of $f_1(t) \circ nL$ and $f_2(t) \circ nL$ where n is the maximum value of k used in the operation. In this example $n = 2$. Let us denote it by $M_N(t)$.

Similarly, in case of closing, we consider the maximum of $f_1(t) \bullet nL$ and $f_2(t) \bullet nL$ for subsequent reconstruction. Let us denote it by $M_X(t)$.

Now, there should be an equal justice to all the crests and troughs of both the functions. Consequently, $M_N(t)$ and $M_X(t)$ should be given equal importance too. With such view we take the average $A(t)$ of $M_N(t)$ and $M_X(t)$ to construct the locally non-varying profile of the fused function. Finally we form the fused function $f_3(t)$ using equation (5.7). Equation (5.7) performs the placement of the crests and troughs at proper locations of the average function.

$$f_3(t) = A(t) + S_{op}(t) - S_{cl}(t) \tag{5.7}$$

Thus the fused function $f_3(t)$ is found to contain crests and troughs from both the functions $f_1(t)$ and $f_2(t)$. The scheme explained for this one-dimensional case may as well be extended to two-dimension.

5.3.3 Implementation

- **Construction of Morphological towers**

  The fusion algorithm proposed in this work is independent of imaging technology. However, in this work we have described the method for fusing CT and MR images of cross-section of human brain. The CT as well as the MR image are

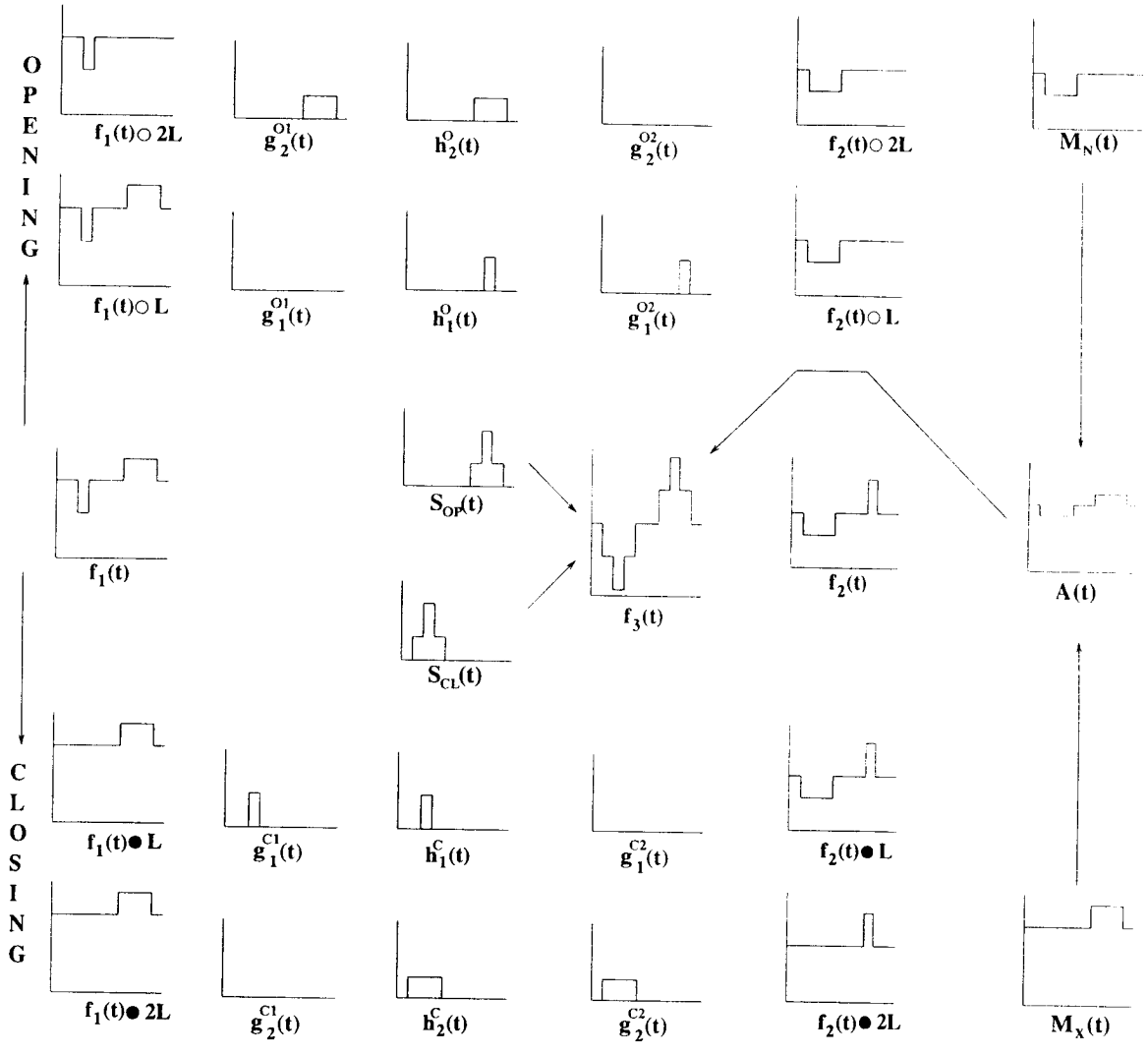

Figure 5.1: Fusion of two functions using multi-scale morphology.

made to undergo a sequence of morphological opening and closing operations with SEs of progressively increasing scale. Here we consider a family of filled circles or *disk*s of increasing radius as structuring elements. For generating the family of filled circles we made use of *Bresenham's* algorithm [42].

We construct two sets of morphological towers for multi-scale opening and closing operations. In each set we have two different towers corresponding to MR and CT images [please see fig. 5.2]. Thus the i-th entry in the multi-scale opening (closing) tower of the CT/MR image contains the image produced by opening (closing) the CT/MR image with a structuring element iB as given below.

$$CT \circ iB = (CT \ominus iB) \oplus iB \tag{5.8}$$

$$MR \circ iB = (MR \ominus iB) \oplus iB \tag{5.9}$$

$$CT \bullet iB = (CT \oplus iB) \ominus iB \tag{5.10}$$

$$MR \bullet iB = (MR \oplus iB) \ominus iB \tag{5.11}$$

for $i = 0, 1, \ldots, n$ where $CT \circ 0B = CT$, $MR \circ 0B = MR$, $CT \bullet 0B = CT$ and $MR \bullet 0B = MR$. Note that B is a structuring element of unit size.

- **Construction of Difference towers**

  We construct four difference towers corresponding to opening and closing operations of the CT and the MR images using difference operations between all successive pairs of images stacked in the opening and closing towers. Fig. 5.2 shows four such *difference towers*. The images in the $i - th$ entries in the difference towers contain features at scale i

$$D^{op}_{CT}(i) = (CT \circ (i-1)B) - (CT \circ iB) \tag{5.12}$$

$$D^{op}_{MR}(i) = (MR \circ (i-1)B) - (CT \circ iB) \tag{5.13}$$

$$D^{cl}_{CT}(i) = (CT \bullet iB) - (CT \bullet (i-1)B) \tag{5.14}$$

$$D^{cl}_{MR}(i) = (MR \bullet iB) - (MR \bullet (i-1)B) \tag{5.15}$$

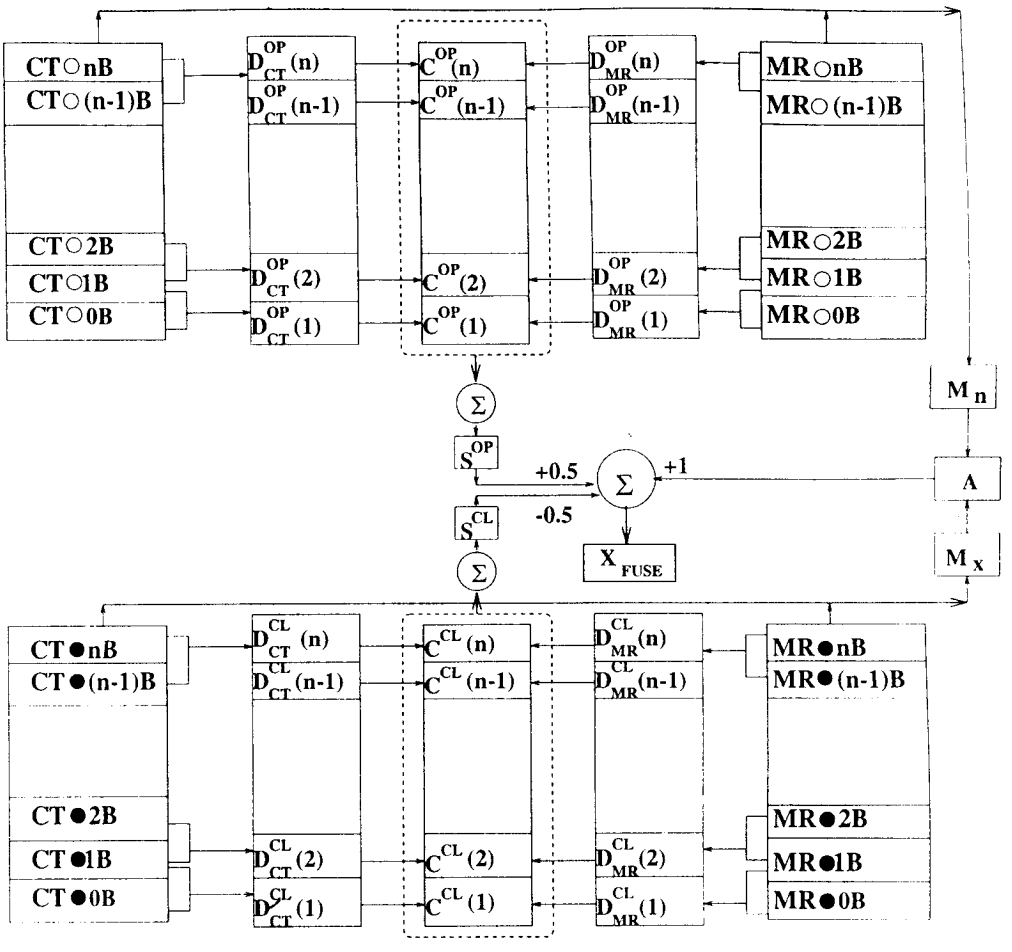

Figure 5.2: Morphological towers for image fusion

for $i = 1, 2, \ldots, n$.

- **Construction of Combined Tower**

  For constructing the fused image from the CT and the MR images, features from both of them are combined. At each scale the feature present in at least one image modality should be collected for fusion. However, if the feature is present in both the images we select the prominent one for constructing the fused image. With such views we extract the prominent features from difference towers for opening (closing) operation by taking pixel-wise *max* of two images as shown

in fig. 5.2. The set of images obtained through max operation are stacked in two more towers called the *combined towers*. The $i-th$ entries of combined tower corresponding to opening and closing operations are therefore the images produced respectively by

$$C^{op}(i) = max\{D^{op}_{CT}(i), D^{op}_{MR}(i)\} \tag{5.16}$$

$$C^{cl}(i) = max\{D^{cl}_{CT}(i), D^{cl}_{MR}(i)\} \tag{5.17}$$

for $i = 1, 2, \ldots, n$. Here max stands for a pixel-wise maximum of two images.

- **Reconstruction**

  For reconstructing the final image we do the following :

  - We sum up all the entries in the combined tower corresponding to the opening operation. This results in an image consisting of bright features of all possible scales that are present in at least one modality with relatively better clarity.

    $$S^{op} = \sum_{i=1}^{n} C^{op}(i) \tag{5.18}$$

    The summation, here, denotes pixel-wise sum of n images.

  - We perform the same operation on the combined tower corresponding to the closing operation. This results in an image consisting of dark features of all possible scales that are present in at least one modality with relatively better clarity.

    $$S^{cl} = \sum_{i=1}^{n} C^{cl}(i) \tag{5.19}$$

  - We take the pixel-wise min (max) operation between the CT and the MR images after opening (closing) them with nB. Then we take the average of these two resulting images.

    $$M_X = max\{CT \bullet nB, MR \bullet nB\} \tag{5.20}$$

    $$M_N = min\{CT \circ nB, MR \circ nB\} \tag{5.21}$$

    $$A = average(M_X, M_N) \tag{5.22}$$

Here *average* denotes the pixel-wise average of two images. Finally, the fused image is obtained by combining three images as given by

$$FUSE = A + \frac{1}{2}S^{op} - \frac{1}{2}S^{cl} \tag{5.23}$$

The '+' and '-' operations are applied between corresponding pixels of three different images.

The algorithm for multi-scale feature extraction is as given below. In the first pass the features at different scales from both the CT and MR image are extracted and stacked in respective morphological towers

Pass-1 : Multi-scale feature extraction

Procedure *Extract_multi-scale_features()*

input: $g_{ct}[][], g_{mr}[][]$; /* the registered input images */

output: open_tower_ct, close_tower, bright_top_tower, dark_top_tower;
/* towers of filtered images */

constant: $MAXSCALE$; /* upper bound of scale factor */

var: $g_{ct}^{op}[][]$, $g_{ct}^{cl}[][], g_{mr}^{op}[][]$, $g_{mr}^{cl}[][]$; /* intermediate images */

integer: i;

$i \leftarrow 1$;

begin

repeat

$g_{ct}^{op} \leftarrow open(g_{ct}, iB)$;

$g_{mr}^{op} \leftarrow open(g_{mr}, iB)$;

$g_{ct}^{cl} \leftarrow close(g_{ct}, iB)$;

$g_{mr}^{cl} \leftarrow close(g_{mr}, iB)$;

$insert\_in\_tower(g_{ct}^{op}, open\_tower\_ct, i)$;

$insert\_in\_tower(g_{mr}^{op}, open\_tower\_mr, i)$;

$insert\_in\_tower(g_{ct}^{cl}, close\_tower\_ct, i)$;

$insert\_in\_tower(g^{cl}_{mr}, close\_tower\_mr, i)$;

$increase\ i$;

until $i > MAXSCALE$;

end begin

end

$i \leftarrow 1$;

begin

repeat

$g_{temp1} \leftarrow get\_image\_from(open\_tower\_ct, i)$;

$g_{temp2} \leftarrow get\_image\_from(open\_tower\_ct, i+1)$;

$g_{temp3} \leftarrow g_{temp1}$ - g_{temp2};

$insert\_in\_tower(g_{temp3}, bright\_top\_tower\_ct)$;

$g_{temp1} \leftarrow get\_image\_from(open\_tower\_mr, i)$;

$g_{temp2} \leftarrow get\_image\_from(open\_tower\_mr, i+1)$;

$g_{temp3} \leftarrow g_{temp1}$ - g_{temp2};

$insert\_in\_tower(g_{temp3}, bright\_top\_tower\_mr)$;

$g_{temp1} \leftarrow get\_image\_from(close\_tower\_ct, i)$;

$g_{temp2} \leftarrow get\_image\_from(close\_tower\_ct, i+1)$;

$g_{temp3} \leftarrow g_{temp2}$ - g_{temp1};

$insert\_in\_tower(g_{temp3}, dark\_top\_tower\_ct)$;

$g_{temp1} \leftarrow get\_image\_from(close\_tower\_mr, i)$;

$g_{temp2} \leftarrow get\_image\_from(close\_tower\_mr, i+1)$;

$g_{temp3} \leftarrow g_{temp2}$ - g_{temp1};

$insert\_in\_tower(g_{temp3}, dark\_top\_tower\_mr)$;

$increase\ i$;

until $i > MAXSCALE$;

end begin

end Procedure

In the second pass we select at each scale the feature that is best represented in the CT and MR image to construct the fused image using the following algorithm.

Pass-2 : Selection of features and their fusion

Procedure *Select_features_and_fuse()*

input: open_tower_ct,open_tower_mr, close_tower_ct, close_tower_mr;

input: bright_top_tower_ct,bright_top_tower_mr dark_top_tower_ct, dark_top_tower_mr;

/* the towers obtained in Pass-1 */

output: g_{fuse}; /* the image containing the segmentation result */

constant: $MAXSCALE$; /* upper bound of scale factor */

var: $g_i^{temp1}[][], g_i^{temp2}[][], g_i^{temp3}[][], g_i^{top\_cont}[][], g_i^{bot\_cont}[][]$; /* intermediate images */

var: $LIST1$, $LIST2$; **ordered list** of components

integer: i;

$i \leftarrow 1$;

begin

repeat

$g_{temp1} \leftarrow get\_image(bright\_top\_tower\_ct, i)$;

$g_{temp2} \leftarrow get\_image(bright\_top\_tower\_ct, i+1)$;

g_{temp3} $g_{temp1} - g_{temp2}$;

$g_{temp1} \leftarrow get\_image(bright\_top\_tower\_ct, i)$;

$g_{temp2} \leftarrow get\_image(bright\_top\_tower\_ct, i+1)$;

g_{temp4} $g_{temp1} - g_{temp2}$;

$g_{ctmr}^{op} \leftarrow g_{ctmr}^{op} + max(g_{temp3}, g_{temp4})$;

$g_{temp1} \leftarrow get\_image(dark\_feature\_tower\_mr, i)$;

$g_{temp2} \leftarrow get\_image(dark\_feature\_tower\_mr, i+1)$;

g_{temp3} $g_{temp2} - g_{temp1}$;

$g_{temp1} \leftarrow get\_image(dark\_feature\_tower\_mr, i)$;

$g_{temp2} \leftarrow get\_image(dark\_feature\_tower\_mr, i+1)$;

g_{temp4} $g_{temp2} - g_{temp1}$;

$g^{cl}_{ctmr} \leftarrow g^{cl}_{ctmr} + max(g_{temp3}, g_{temp4})$;

$g^{cl}_{ctmr} \leftarrow g^{cl}_{ctmr} + g^{cl}_{ctmr\_i}$

if($i == MAXSCALE$) then

$g_{temp1} \leftarrow get\_image(open\_tower\_ct, i)$;

$g_{temp2} \leftarrow get\_image(open\_tower\_mr, i)$;

$g^{op}_{min} \leftarrow min(g_{temp1}, g_{temp2}$;

$g_{temp1} \leftarrow get\_image(close\_tower\_ct, i)$;

$g_{temp2} \leftarrow get\_image(close\_tower\_mr, i)$;

$g^{cl}_{max} \leftarrow max(g_{temp1}, g_{temp2})$;

$g_{baseimg} \leftarrow avg(g^{op}_{min}, g^{cl}_{max})$;

endif

$increase\ i$;

until $i > MAXSCALE$;

end begin

end Procedure

5.4 Experimental Results and Discussions

As stated earlier the proposed algorithm is independent of imaging technology. Hence it can be used for fusing images obtained through any multi-sensor image acquisition system. However, we have demonstrated the performance of the proposed algorithm using CT and MR images of cross-section of human brain. The details regarding the acquisition of the CT and MR images on which we have executed our proposed algorithmic steps are specified below.

The MR image has been obtained on a Genesis Sigma scanner. Window width and

the window length of the image are 1120 and 561 respectively. The slice thickness for the image is $5mm$ while the magnification ratio is 1.5. The field of vision for the image is 240.00. The MR image in its original form is basically a DICOM image. Finally, a pixel matrix of size 512×512 is obtained. The CT image, which also is originally a DICOM image, is obtained using a Rhapsode scanner with a magnification of 1.25 and field of vision equal to 189.89. The window width and length for the CT image are 2985 and 496 respectively while the slice thickness is $1.0mm$. Final image is again of size 512×512. The original CT and MR images are shown in fig. 5.3(a) and fig. 5.3(b) respectively.

Figs 5.3(c) and 5.3(d) are images obtained by applying registration technique as described in section 5.2. The fused image constructed according to the proposed method is shown in fig. 5.4(a). In our experiment we have taken B a disk of radius one and $n = 33$. The fused image is found to contain salient features that are present in either modalities without any distortion. Second, it is found to be clinically more informative as compared to the individual constituting images.

5.4.1 Performance analysis

The fusing ability of the algorithm is measured quantitatively by means of, say, pixel-gray level correlation between two images. Let us define correlation between two images f and g by

$$R(f,g) = \frac{\sum_{r,c}(f(r,c) - \bar{f})(g(r,c) - \bar{g})}{\sqrt{\sum_{r,c}(f(r,c) - \bar{f})^2}\sqrt{\sum_{r,c}(g(r,c) - \bar{g})^2}} \tag{5.24}$$

where, $\bar{f} = \frac{1}{N}\sum_{r,c} f(r,c)$ and $\bar{g} = \frac{1}{N}\sum_{r,c} g(r,c)$ and N is the total number of pixels in either of the images. In our experiment the computed values of $R(FUSE, CT)$, $R(FUSE, MR)$ and $R(CT, MR)$ are 0.89, 0.81 and 0.59 respectively. Since $R(FUSE, CT) > R(MR, CT)$ and $R(FUSE, MR) > R(MR, CT)$, the fused image

enjoys relatively high correlation with either of the images. This implies features of both the images are transported to the fused image. However, this measure is too simple to yield any strong conclusion. To account for a better measure for the extent of similarity between the fused image and either of its constituting images we carry out the following analysis.

Similarity measure

Two images, say for example, f and g are said to be similar subject to some *scaling* (by a constant factor C) and a d.c. bias (by a constant D), if the following relation holds for every pixel of f and g. That means f and g are similar if

$$g(r,c) = Cf(r,c) + D \tag{5.25}$$

for all (r,c). Based on this relation, one can estimate one of the images, say, g from the other image f about which one has relatively better knowledge. Thus the estimated image g_{est} is given by

$$g_{est}(r,c) = Cf(r,c) + D \tag{5.26}$$

However, the accuracy of this estimation relies on how correctly the parameters C and D are determined. The Euclidean distance or the error between images g and g_{est}, the image estimated from f, is then given by

$$E(g,g_{est}) = \sum_r \sum_c (g(r,c) - Cf(r,c) - D)^2 \tag{5.27}$$

The parameters C and d of this relation can be estimated in such a way that $E(g,g_{est})$ is minimum. However, the relation reflects our bias toward the knowledge about the image f. To get rid of such bias to any of the images under consideration we make use of the following expression for the error.

$$E(g,g_{est}) = \frac{\sum_r \sum_c (g(r,c) - Cf(r,c) - D)^2}{1 + C^2} \tag{5.28}$$

This is also known as *eigen-vector fitting* [54]. The parameters C and D are estimated by solving the normal equations generated by taking partial derivatives of $E(g, g_{est})$ with respect to C and D and equating them to zero, *i.e.*,

$$\frac{\partial}{\partial C}E(g, g_{est}) = 0 \tag{5.29}$$

$$\frac{\partial}{\partial D}E(g, g_{est}) = 0 \tag{5.30}$$

From the second normal equation we get:

$$\frac{2}{1+C^2}\sum_r\sum_c(g(r,c) - Cf(r,c) - D) = 0$$

$$\text{or,} \qquad D = \bar{g} - C\bar{f}$$

Substituting the value of D in equation (5.29) and solving it we get an expression for C as follows.

$$\sum_r\sum_c \frac{2(1+C^2)(g(r,c) - Cf(r,c) - D)(-f(r,c)) - 2C(g(r,c) - Cf(r,c) - D)^2}{(1+C^2)^2} = 0$$

$$\text{or,} \qquad \sum_r\sum_c(g(r,c) - Cf(r,c) - D)(f(r,c) + Cg(r,c) - CD) = 0$$

$$\text{or,} \qquad \sum_r\sum_c(g(r,c) - Cf(r,c) - \bar{g} + C\bar{f})(f(r,c) + Cg(r,c) - C\bar{g} + C^2\bar{f}) = 0$$

$$\text{or,} \qquad C^2V_{fg} + C(V_f - V_g) - V_{fg} = 0$$

where

$$V_f = \frac{1}{N}\sum_r\sum_c(f(r,c) - \bar{f})^2$$

$$V_g = \frac{1}{N}\sum_r\sum_c(g(r,c) - \bar{g})^2$$

$$V_{fg} = \frac{1}{N}\sum_r\sum_c(f(r,c) - \bar{f})(g(r,c) - \bar{g})$$

Solving the quadratic equation in C we get

$$C_1 = \frac{-(V_f - V_g) + \sqrt{(V_f - V_g)^2 + 4V_{fg}^2}}{2V_{fg}}$$

$$C_2 = \frac{-(V_f - V_g) - \sqrt{(V_f - V_g)^2 + 4V_{fg}^2}}{2V_{fg}}$$

The values of C and D are then used to find out the error $E(g, g_{est})$. Now corresponding to two values of C we get two values of the estimated error. For our purpose we choose the minimum of the two. The mathematical expression for the minimum error is

$$\begin{aligned}
E(g, g_{est}) &= \sum\sum \frac{(g(r,c) - Cf(r,c) - D)^2}{1+C^2} \\
&= \sum\sum \frac{((g(r,c) - \bar{g}) - C(f(r,c) - \bar{f}))^2}{1+C^2} \\
&= (\frac{1}{1+C^2})(\frac{1}{n}\sum\sum(g(r,c) - \bar{g})^2) \\
&\quad +(\frac{C^2}{1+C^2})(\frac{1}{n}\sum\sum(f(r,c) - \bar{f})^2) \\
&\quad -(\frac{2C}{1+C^2})(\frac{1}{n}\sum\sum(g(r,c) - \bar{g})(f(r,c) - \bar{f})) \\
&= \frac{1}{1+C^2}V_g + \frac{C^2}{1+C^2}V_f - \frac{2C}{1+C^2}V_{gf} \\
&= \frac{1}{1+C^2}V_g + \frac{C^2}{1+C^2}V_f - \frac{c}{1+C^2}V_{gf} - \frac{C}{1+C^2}V_{gf} \\
&= \frac{1}{1+C^2}(V_g - CV_{gf}) + \frac{C}{1+C^2}(CV_f - V_{gf}) \\
&= \frac{1}{1+C^2}(V_g - CV_{gf}) + \frac{C}{1+C^2}C(V_g - CV_{gf}) \\
&= (V_g - CV_{gf})(\frac{1}{1+C^2} + \frac{C^2}{1+C^2}) \\
&= V_g - CV_{gf}
\end{aligned}$$

Substituting the value of C we get

$$\begin{aligned}
E_1(g, g_{est}) &= \frac{1}{2}(V_f + V_g + \sqrt{(V_f - V_g)^2 + 4V_{fg}^2}) \\
E_2(g, g_{est}) &= \frac{1}{2}(V_f + V_g - \sqrt{(V_f - V_g)^2 + 4V_{fg}^2}) \\
E(g, g_{est}) &= min(E_1(g, g_{est}), E_2(g, g_{est})) \\
&= \frac{1}{2}(V_f + V_g - \sqrt{(V_f - V_g)^2 + 4V_{fg}^2})
\end{aligned} \tag{5.31}$$

The minimum error $E(g, g_{est})$ gives the measure of the unbiased distance between the two images f and g. Finally, based on this error we define a measure of similarity as

$$s(f, g) = 1 - \frac{E(g, g_{est})}{V_g + V_{g_{est}}} \tag{5.32}$$

When similarity measure, as given in equation (5.32), is not equal to one or, in other words, error between the functions, as given in equation (5.31) is not zero, similarity measure based on only their values is not a sufficient indication. In that case we need to compare spatial variation, too, of those functions. As we know, spatial variation can be analysed by means of derivative operators. Hence, to measure the similarity between two images we should not only compare their pixel values but also compare their spatial derivatives of different orders. That means two very similar images should have their derivative or gradient images also very similar. Consequently, the error or distance between their derivative images must also be small. To save time and space we have considered here only the first order (i.e. *gradient*) and the second order (i.e. *laplacian*) images along with the pair of original images for computing the error and, consequently, the similarity between each pair of images. As an overall measure of similarity we have taken the product of the individual similarities. Thus the *overall similarity* $S(f, g)$ is measured as

$$S(f, g) = s(f, g).s(f', g').s(f'', g'') \tag{5.33}$$

Finally, the *degree of fusion* is measured as:

$$\delta = min\{S(Fuse, CT), S(Fuse, MR)\} \tag{5.34}$$

At this point we like to present few other widely used image fusion methods with which we have compared the performance of our method. A brief description of other schemes is given below.

Averaging [53]

Averaging is the simplest technique of fusing two images in which the fused image is

formed by a pixel-wise averaging of the constituting images. This method is crude and does not hold good in many cases. The fused image may not contain many salient features of the individual images. As a result there may be a huge loss of information at the time of blending the multi-modal images. Fused image obtained by averaging the images shown in fig 5.3(c) and 5.3(d) is shown in fig. 5.4(b).

Fusion employing K-L Transform [53]

For constructing the fused image employing K-L transform, we form N vectors $\mathbf{f_1}$, $\mathbf{f_2}$, ..., $\mathbf{f_N}$ where $\mathbf{f_j} = \{f_{1j}, f_{2j}\}$. The first element comes from the first image while the second comes from the second image. We then construct the *mean* vector and the *variance-covariance matrix* from these N vectors. The fused image $F(r, c)$ is constructed from the individual images $F_1(r, c)$ and $F_2(r, c)$ using the following relation

$$F(r, c) = \phi_1 F_1(r, c) + \phi_2 F_2(r, c) \tag{5.35}$$

where $\mathbf{\Phi} = \{\phi_1, \phi_2\}$ is the normalized eigen vector of the variance-covariance matrix corresponding to its largest eigen value. Thus this method is nothing but a weighted averaging technique where the weights are determined by the K-L transform. Fused image obtained by using this method on the images shown in fig 5.3(c) and 5.3(d) is shown in fig. 5.4(c).

Fusion employing morphological pyramid [97]

This morphological fusion scheme uses a multi-resolution image decomposition method in order to improve the transformation of useful information from one image to the other at every decomposition level. The method relies on formation of image pyramid using morphological sampling theorem [62]. Fusion of images using this method can be found in [97]. Fused image obtained by using this method on the images shown in fig 5.3(c) and 5.3(d) is shown in fig. 5.4(d).

We have compared the performance of our fusion scheme with that of other well

(a)

(b)

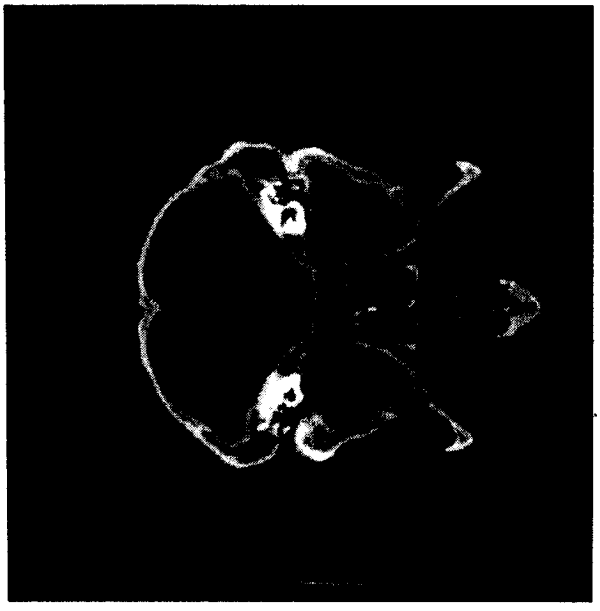

(c)

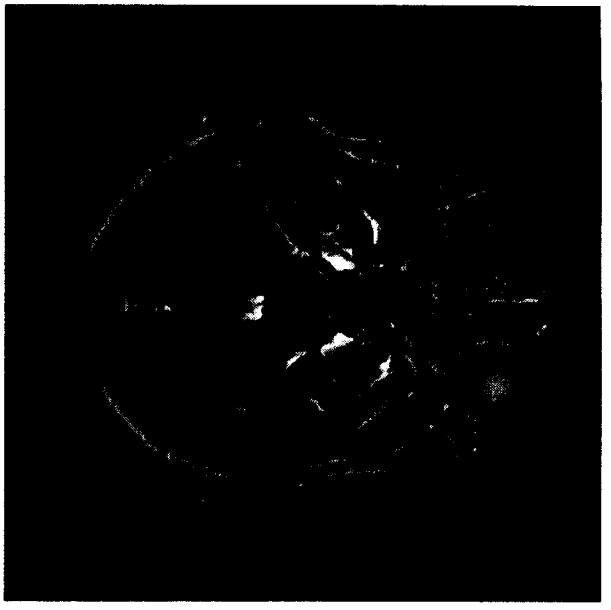

(d)

Figure 5.3: Test images used in the experiment (a) CT image, (b) MR image, (c) registered CT image and (d) registered MR image.

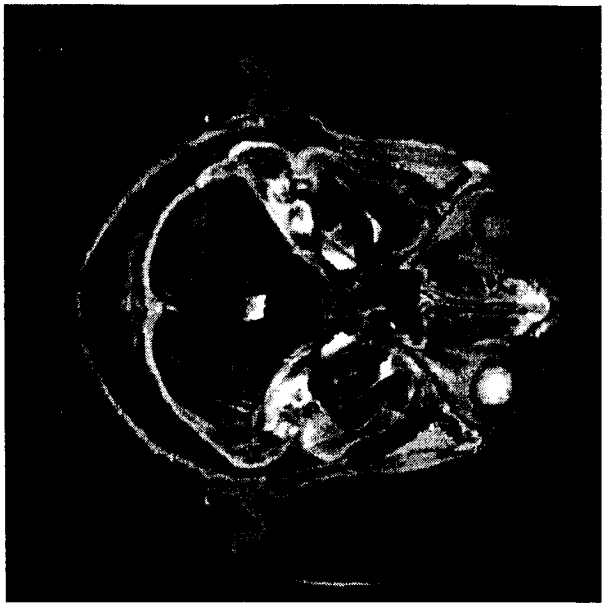

(a)

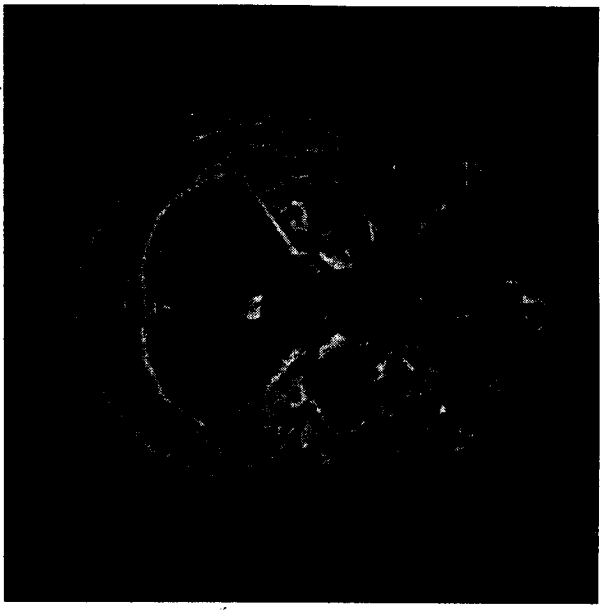

(b)

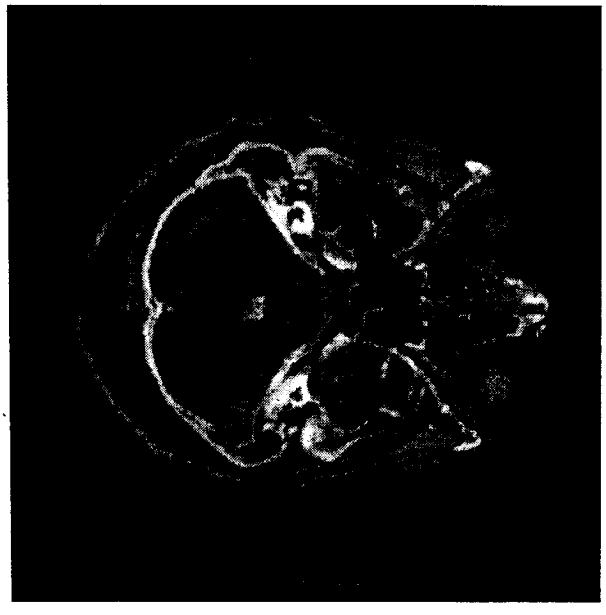

(c)

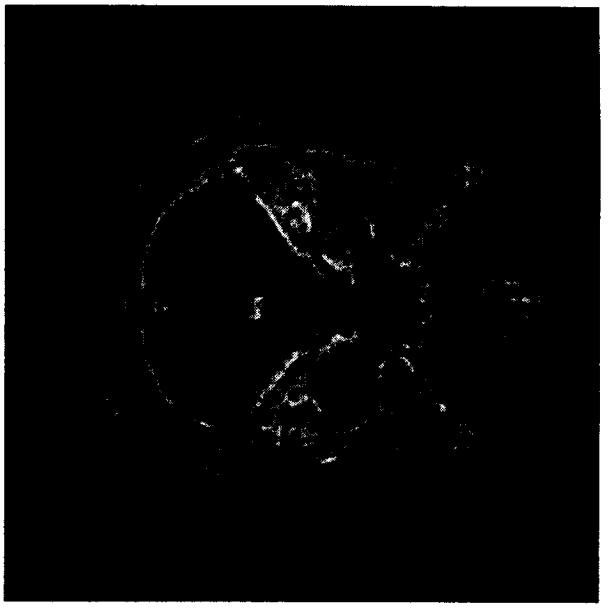

(d)

Figure 5.4: Results of fusion employing (a) morphological tower, (b) simple averaging (c) KL transform and (d) pyramid.

Table 5.1: Comparative study of different fusion schemes

Image1	Image2	Level of comparison						Overall Similarity	Degree of Fusion
		Original Images		Gradient Images		Laplacian Images			
		Error	Similarity	Error	Similarity	Error	Similarity		
$FUSE_{mmf}$	CT	295.99609	0.95019	32.25394	0.861920	1115.727539	0.952152	0.779797	0.779797
$FUSE_{mmf}$	MR	324.74359	0.94948	29.61146	0.865361	1223.828857	0.951479	0.781777	
$FUSE_{pyr}$	CT	158.84448	0.95525	19.68276	0.778367	587.132812	0.946611	0.712417	0.691508
$FUSE_{pyr}$	MR	271.66717	0.92718	17.56349	0.801107	1017.848145	0.930977	0.691508	
$FUSE_{avg}$	CT	136.04761	0.95186	16.47837	0.762021	505.472656	0.954643	0.692436	0.692436
$FUSE_{avg}$	MR	200.38049	0.93121	12.53961	0.823891	752.016602	0.934566	0.717018	
$FUSE_{KLT}$	CT	98.84716	0.98376	11.98582	0.920979	367.261719	0.984709	0.892174	0.670788
$FUSE_{KLT}$	MR	380.81756	0.94398	35.01140	0.750388	1418.872314	0.946963	0.670788	

mmf: Proposed approach, pyr: pyramidal approach, avg: averaging, KLT: K-L transform

known schemes such as *averaging*, *morphological pyramid* and *K-L transform*. A visual comparison among figs. 5.4(a–d) reveal that our method produces best result giving appropriate emphasis to features of all scales coming from both the images. For quantitative comparison of the results, we have computed the similarity between the *fused* image and the CT (or the MR) image for all the schemes mentioned above and, finally, computed the degree of fusion for each of them. The results are summarized in Table 5.1. Table 5.1 indicates that the *Degree of fusion* is maximum for the proposed fusion scheme. In that scheme the image pairs along-with their first and second-order gradients maintain consistently high similarity values. Morphological pyramidal approach and averaging technique fuse images with comparable degree of fusion. However, experimental results show that former one is much superior to the latter. Performance of averaging technique and K-L transform based technique are comparable for a large set of images. Moreover, K-L transform based fusion scheme is slightly better than averaging based scheme, though Table 5.1 shows the reverse for this particular example.

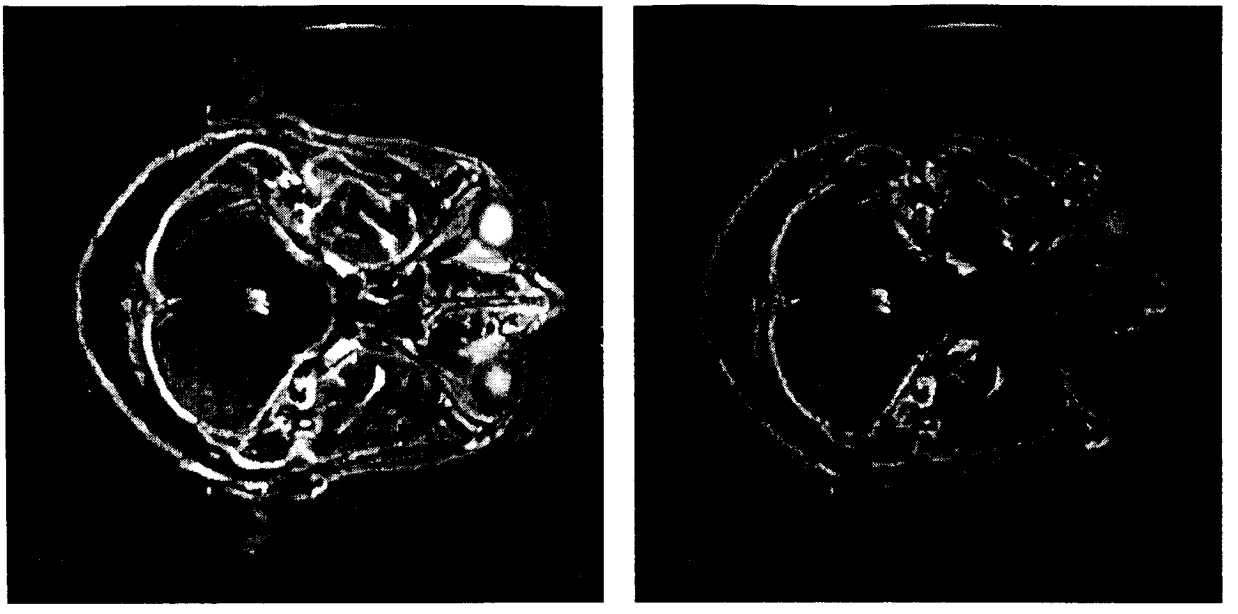

(a) (b)

Figure 5.5: fusion (a) employing only opening and (b) only closing

The proposed scheme emphasizes equally on the bright and dark features of both the images participating in fusion. The images may not have identical contents of bright and dark features at different scales. From the experimental point of view we have performed the operations of fusion on the same set of images using only opening and only closing and presented the results in fig. 5.5. The same performance metrics are computed for each of these images (see table 5.2). From the table the performance of is seen to be better in case of the fusion scheme employing only opening. However, this may not be true for all kinds of images specially where there are more dark features than bright features.

5.5 Conclusion

In this chapter we have presented a method for fusing two-dimensional multi-sensor gray-scale images using multi-scale morphology. The usefulness of the method is

Table 5.2: Comparative study of fusion employing different multi-scale morphological filtering (mmf)

Image1	Image2	Level of comparison						Overall Similarity	Degree of Fusion
		Original Images		Gradient Images		Laplacian Images			
		Error	Similarity	Error	Similarity	Error	Similarity		
$FUSE_{mmf}$	CT	295.99609	0.95019	32.25394	0.861920	1115.727539	0.952152	0.779797	0.779797
$FUSE_{mmf}$	MR	324.74359	0.94948	29.61146	0.865361	1223.828857	0.951479	0.781777	
$FUSE^{opn}_{mmf}$	CT	502.13635	0.93085	44.97159	0.935871	1872.425781	0.932908	0.812705	0.812705
$FUSE^{opn}_{mmf}$	MR	313.33133	0.95926	34.97646	0.939338	1183.401855	0.960059	0.865083	
$FUSE^{cls}_{mmf}$	CT	421.18301	0.83474	48.29529	0.902344	1544.046631	0.839928	0.632656	0.632656
$FUSE^{cls}_{mmf}$	MR	412.77920	0.85329	41.86358	0.898311	1570.447144	0.852041	0.653110	

mmf: proposed approach, opn: mmf using only opening, cls: mmf using only closing

illustrated using CT and MR images of cross-section of human brain. The result of the proposed method is compared with that of some widely used image fusion methods both qualitatively and quantitatively. Experimental results reveal that the proposed method produces better fused image than that by the latters. However, our method is computationally more expensive and needs more space for implementation. It should be noted that the proposed algorithm is domain-independent. That means it uses knowledge of neither the imaging device nor the objects being imaged. Therefore it can be applied to fusion of other kinds of multi-sensor images, e.g. satellite images, too. Second, as the actual fusion is done during the construction of combined towers by taking the pixel-wise maximum, the algorithm can readily be extended for fusing more than two images. We wish to extend our work for fusing multi-sensor images in three-dimension. Also, special attention needs to be paid for reducing space and time requirement for the implementation of the algorithm. Finally, the method may be straightaway extended to fuse more than two images.

In this chapter we have seen the application of morphological tower in a relatively

higher level processing. In the next chapter we will see how the morphological towers may be utilized in another higher level processing namely segmentation.

Chapter 6

Segmentation

6.1 Introduction

In this chapter we propose another important application of morphological tower. A method for segmenting gray-level real images using multiple morphology is presented in this chapter. Segmentation is widely demanded task of image processing. There are different standard techniques for image segmentation (see section 1.5.5). The applicability of a given segmentation algorithm also depends on the type of the image it is meant for. For example, an algorithm for segmenting a biomedical image will not perform well in segmenting textured images. In this work [116] we propose an algorithm for segmenting gray-level images consisting of features of different scales.

This region-based approach resembles watershed algorithm in finding the segments. The dark features at various scales are basically similar to canyons of different width and depth on the intensity surface topography of the gray level image. These canyons are gradually filled using multi-scale morphological closing by reconstruction with isotropic structuring element and its higher order dilates. The bright features on the

other hand are similar to mountains of different width and altitude on the intensity surface topography of the gray level image. These mountains are clipped in the same way using multi-scale morphological opening by reconstruction. The formation or existence of a valid or significant segment corresponding to bright and dark features at each scale is controlled by three criteria namely *growing, merging and saturation.* Segments formed from the features extracted at various scales are integrated in the final result. The algorithm is composed of two passes preceded by a preprocessing step for simplifying small scale details of the image that might cause over-segmentation. In the first pass feature images at various scales are collected and kept in respective towers. In the second pass, potential features contributing to the formation of segments at various scales are detected. Finally the algorithm traces the contours of all such contributing segments at various scales. The result is superposed on the original image to verify the efficacy of the method. The proposed algorithm has been implemented using morphological towers and executed on a set of images (real as well as synthetic). The results obtained from the proposed method have been compared with those from other standard methods.

The segmentation scheme proposed in this chapter involves morphological filtering over a large number of scale factors depending on the image under study. The issues like *causality, edge localization, scale-calibration* of features etc. are therefore very important. Therefore, the conventional morphological filtering is not used in this work. Instead, we have made use of filters by reconstruction. The computational time is therefore large.

The chapter is organized in the following way. In section 6.2 we have presented the proposed method. The theoretical formulation of the proposed method is discussed elaborately in section 6.2.1 while the implementational details are given in section 6.2.2. The experimental results are presented in section 6.3. A performance measure based on similarity of the segmenting contours with the ideal contours is

presented in section 6.3.1. Finally, the concluding remarks are given in section 6.4.

6.2 Proposed method

As mentioned in earlier section, a gray level image typically consists of both bright and dark object features which, in general, have a distribution with respect to size or *scale*. The basic objective of a segmentation algorithm is to isolate or sketch out the most optimal boundaries or contours of these bright and dark features of varying scale. Though the proposed method is basically region based but it produces contours enclosing pixels that have properties distinguishable from their immediate neighborhoods. In this section we first present the theoretical background of the proposed method. Then we present the implementational details in the next subsection.

6.2.1 Theoretical Formulation

A digital gray-tone image is basically an intensity surface defined over a spatial coordinate system. If $L = \{0, 1, \ldots, L_m\}$ be the set of intensity values and $S = \{(r, c) : r, c \in Z, 0 \leq r \leq N_r, 0 \leq c \leq N_c\}$ be the spatial coordinates of the pixels of the image, the digital image represented as a function g is then defined as

$$g : S \rightarrow L \tag{6.1}$$

Thus $g(r, c)$ represents the intensity value of the pixel located at $(r, c) \in S$ and the size of the image is $N_r \times N_c$.

The section of the image at a threshold intensity $k \in L$ is a set $X^k(g)$ of points defined as

$$X^k(g) = \{(r, c) : (r, c) \in S \text{ and } g(r, c) \geq k, k \in L\} \tag{6.2}$$

The binary or $0-1$ image or simply a black-and-white image $g_{bin} : S \rightarrow \{0,1\}$ constructed from this set $X^k(g)$ as described below.

$$g_{bin}(r,c) = \begin{cases} 1 & \text{if } (r,c) \in X^k(g) \\ 0 & \text{otherwise} \end{cases}$$

In the proposed formulation we have made use of multi-scale bright and dark top-hat transformation in order to extract scale specific bright and dark features. A thorough analysis of these extracted features might be useful for the task of segmentation of gray-level image. In morphological filtering a bright top-hat transformation on a gray tone image extracts bright objects that are smaller than the structuring element.

The bright top-hat image resulting after filtering by an SE of size i contains all bright features smaller than i as given below.

$$g_i^{top}(r,c) = g(r,c) - (g \circ iB)(r,c) \tag{6.3}$$

Similarly a dark top-hat or a *bottom-hat* transformation at scale i on a gray tone image sieves out the dark features smaller than i as shown below

$$g_i^{bot}(r,c) = (g \bullet iB)(r,c) - g(r,c) \tag{6.4}$$

Now, using equations (6.2), the section of the bright and dark top-hat images at a threshold intensity t are given by

$$\Pi_i^t = X^t[g_i^{top}] = \{(r,c) \in S : g_i^{top}(r,c) \geq t, t \in L\} \tag{6.5}$$

$$\Upsilon_i^t = X^t[g_i^{bot}] = \{(r,c) \in S : g_i^{bot}(r,c) \geq t, t \in L\} \tag{6.6}$$

The sets Π_i^t and Υ_i^t basically contain the coordinates of the supports of the features at scale i that are present in the bright and dark top-hat images respectively. Now, if the value of the intensity threshold t is kept fixed through out the process, the

superscript t may be dropped out from being appeared in the notations of the sets. In such a case we may simply use Π_i and Υ_i to denote Π_i^t and Υ_i^t respectively.

Now, the opening is an anti-extensive transformation [62] which means that the domain of the opened object is a subset of that of the original object. Also, the domain of the object opened at higher scale is a subset of that opened at lower scale. The top-hat images are obtained by subtracting the opened image from the original image. So, we necessarily have

$$\Pi_0 \subseteq \Pi_1 \subseteq \ldots \subseteq \Pi_i \subseteq \Pi_{i+1} \subseteq \ldots \subseteq \Pi_N \tag{6.7}$$

For similar reasons, for the dark features, we necessarily have

$$\Upsilon_0 \subseteq \Upsilon_1 \subseteq \ldots \subseteq \Upsilon_i \subseteq \Upsilon_{i+1} \subseteq \ldots \subseteq \Upsilon_N \tag{6.8}$$

Here N is an integer representing the largest scale of objects or features present in the image and it may be same as the size of the image itself. However, in practice, N is much less than the size of the image.

Now, the surface topography of a gray-level image, in general, is full of peaks, valleys and possibly plateaus of different height, width, extent. Consequently, each of the sets Π_i and Υ_i is found to consist of a number of maximally connected subsets [131], so that, each of them can be expressed as

$$\Pi_i = \Pi_i^1 \bigcup \Pi_i^2 \bigcup \Pi_i^3 \bigcup \ldots \bigcup \Pi_i^p \tag{6.9}$$

$$\Upsilon_i = \Upsilon_i^1 \bigcup \Upsilon_i^2 \bigcup \Upsilon_i^3 \bigcup \ldots \bigcup \Upsilon_i^q \tag{6.10}$$

where p and q are the number of maximally connected subsets in Π_i and Υ_i respectively. In addition, for any pair of distinct subsets of Π_i and Υ_i we strictly have

$$\Pi_i^u \bigcap \Pi_i^v = \emptyset \tag{6.11}$$

$$\Upsilon_i^u \bigcap \Upsilon_i^v = \emptyset \tag{6.12}$$

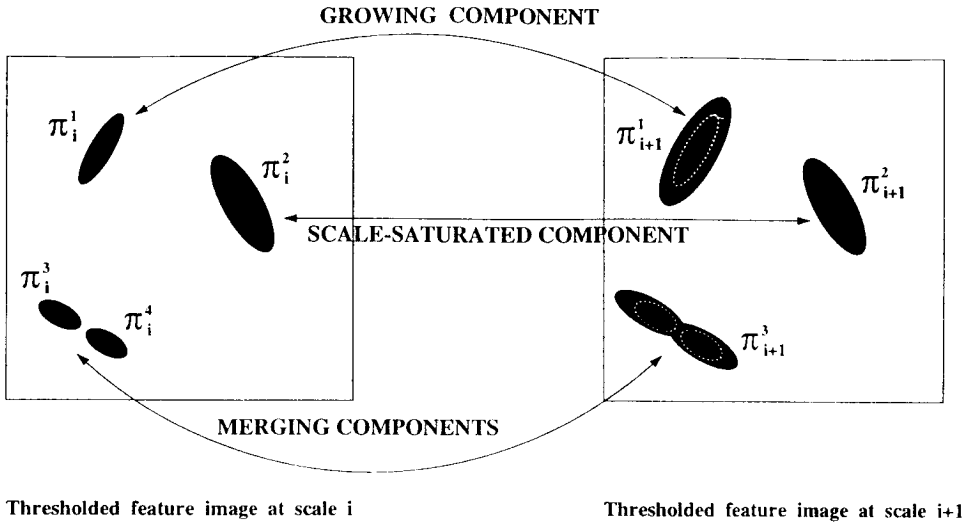

$\pi_i^1 \subset \pi_{i+1}^1$: The component π_i^1 grows in size as the scale increases from i to i+1

$\pi_i^2 \subseteq \pi_{i+1}^2$: The component π_i^2 remains same in size as the scale increases from i to i+1

$\pi_i^3 \cup \pi_i^4 \subset \pi_{i+1}^3$: The components π_i^3 and π_i^4 merge into π_{i+1}^3 as the scale increases from i to i+1

Figure 6.1: Different types of similar components at two successive scale i and $i+1$

for $u \neq v$. The subset Π_i^u (Υ_i^u) basically represents a bright (dark) feature or its part at scale i. In other words, the binary images constructed using these sets are found to contain a number of isolated black blobs against a white background.

Let us consider two sets Π_i and Π_{i+1} corresponding to two bright top-hat images at two successive scales i and $(i+1)$. For each subset Π_i^u of Π_i there exists one and only one subset Π_{i+1}^v of Π_{i+1} such that $\Pi_i^u \subseteq \Pi_{i+1}^v$. Let us call such subsets as *corresponding subsets*. It is important to note that the total number of subsets in Π_i and Π_{i+1} may not necessarily be the same. The above statements hold good for sets Υ_i and Υ_{i+1} also. At any given scale, the subsets Π_i^us of Π_i may encounter one of the following three situations

(1) Growing : A subset Π_i^u is said to be *growing* if it is a proper subset of its corresponding subset Π_{i+1}^v, i.e., $\Pi_i^u \subset \Pi_{i+1}^v$. In such cases, the black blob

represented by the subset Π_i^u in the binary image constructed from Π_i represents the support of a part of a potential feature or object. Fig. 6.1 illustrates the situation indicating a pair of corresponding subsets at two successive scales. The subset Π_i^1 in the set Π_i is a proper subset of Π_{i+1}^1 in Π_{i+1}. The bright dots in Π_{i+1}^1 indicates the growth of Π_i^1 with the scale parameter.

(2) Saturation : A subset Π_i^u is said to be *saturated* if it is congruent with its corresponding subset Π_{i+1}^v, i.e., $\Pi_i^u = \Pi_{i+1}^v$. In such cases, the black blob represented by the subset Π_i^u in the binary image constructed from Π_i covers the support of a feature or object as a whole. This case, as earlier, is illustrated in fig. 6.1. The subsets Π_i^2 and Π_{i+1}^2 are congruent and there is no change in Π_i^2 with the scale parameter.

(3) Merging : If at least two subsets Π_i^u and Π_i^w have the same corresponding subset Π_{i+1}^v, i.e., $\Pi_i^u \bigcup \Pi_i^w \subseteq \Pi_{i+1}^v$, the constituent subsets Π_i^u and Π_i^w are said to be *merging*. Two or more merging subsets might enjoy a subsequent growth or saturation with respect to the scale factor. In such a case, each of them individually represents a complete sub-feature which is a distinct part of a large valid feature or object at subsequent higher scale. This situation too, is clarified in fig. 6.1. The dark blobs represented by Π_i^1 and Π_i^2 are found to have the same corresponding subset Π_{i+1}^3. These two dark blobs merge into a single larger blob represented by Π_{i+1}^3.

The above observations hold good for Υ_i and Υ_{i+1} also. The proposed algorithm being a region-based technique should not treat the subsets of all three categories at various scales identically. Accordingly, the following four sets may be constructed.

$$Sat_i^{top} = [\{\Pi_i^u\} : \text{ if there exist } u \text{ and } w, \text{ such that, } \Pi_i^u \subseteq \Pi_{i+1}^w]$$

$$Sat_i^{bot} = [\{\Upsilon_i^u\} : \text{ if there exist } u \text{ and } w, \text{ such that, } \Upsilon_i^u \subseteq \Upsilon_{i+1}^w]$$

$$Mrg_i^{top} = [\{\Pi_i^u \bigcup \Pi_i^v\} : \text{ if there exist } u, v \text{ and } w, \text{ such that, } (\Pi_i^u \bigcup \Pi_i^v) \subset \Pi_{i+1}^w.]$$

$$Mrg_i^{bot} = [\{\Upsilon_i^u \bigcup \Upsilon_i^v\} : \text{ if there exist } u, v \text{ and } w, \text{ such that, } (\Upsilon_i^u \bigcup \Upsilon_i^v) \subset \Upsilon_{i+1}^w.]$$

for $1 \leq i \leq N-1$. Thus, the sets defined above, provides the bright and dark features at scale i present in the image.

Let $g_i^{top\_bin}$ and $g_i^{bot\_bin}$ be the binary images constructed from the sets C_i^{top} and C_i^{bot} respectively, where

$$C_i^{top} = Sat_i^{top} \bigcup Mrg_i^{top} \tag{6.13}$$

$$C_i^{bot} = Sat_i^{bot} \bigcup Mrg_i^{bot} \tag{6.14}$$

These binary images comprise of black blobs representing the supports of potential bright and dark features present in the input image at scale i. These blobs, therefore, correspond to the segments of the image. Suppose $g_i^{top\_cont}$ and $g_i^{bot\_cont}$ denote the images containing the closed edges of the blobs in $g_i^{top\_bin}$ and $g_i^{bot\_bin}$ respectively. Hence, the final contour-image g_{cont} is obtained by unifying the contour images at all possible scales as described by the following equation.

$$g_{cont} = \{\bigcup_{i=1}^{N} g_i^{top\_cont}\} \bigcup \{\bigcup_{i=1}^{N} g_i^{bot\_cont}\} \tag{6.15}$$

Encroachment problem :

Any segmentation algorithm follows its own predefined strategy. Quite often, the gray-level of the pixel or its gradient play important role in the construction of the segments. The problem of employing gradient magnitude is its noise sensitivity. The proposed algorithm, however, does not employ the knowledge about gradient magnitude. In case of watershed algorithm the basic objective is flooding the entire image surface into an infinite source of fluid with uniform vertical upward speed after boring small holes at the regional minima on the surface topography. In the proposed algorithm emphasis has been given on the *scale* of the image features while finding the

valid segments of the image. The bright and dark features of identical scale are detected sequentially at the same pass of the algorithm. The image, in general,consists of both the bright and dark features at varying scales. When a bright feature is adjacent to a dark feature, a problem of feature overlapping may occur. The SE has no preferred knowledge about the locations of bright and dark features and their scales. Therefore, if the SE is allowed to open and close the image with no restriction regarding when and where it must stop, it will cause an overlapping or *mutual encroachment* in the sets Π_i and Υ_j for same or different values of i and j (fig. 6.2 may be referred for an illustration). In other words, the same spatial domain of the image would be claimed as a support of a number of dark as well as bright features at same or different scales. In the foregoing discussion, no restriction was put to the relationship between Π_i and Υ_j . The binary images constructed using Π_i and Υ_j will therefore give rise to overlapping or encroaching segmenting contours. To get rid of this encroachment problem the following constraint may be enforced.

$$\Pi_i \bigcap \Upsilon_j = \emptyset \tag{6.16}$$

To satisfy the above constraint or, in other words, to avoid encroachment, equations (6.3) and (6.4) may be modified, respectively, as

$$g_i^{top}(r,c) = \tilde{g}_{i-1}(r,c) - (\tilde{g}_{i-1} \circ iB)(r,c) \tag{6.17}$$

$$g_i^{bot}(r,c) = (\hat{g}_{i-1} \bullet iB)(r,c) - \hat{g}_{i-1}(r,c) \tag{6.18}$$

where

$$\tilde{g}_i(r,c) = \begin{cases} -\infty & \text{if } (r,c) \in \Upsilon_{i-1} \\ \tilde{g}_{i-1}(r,c) & \text{otherwise} \end{cases}$$

and

$$\hat{g}_i(r,c) = \begin{cases} \infty & \text{if } (r,c) \in \Pi_{i-1} \\ \hat{g}_{i-1}(r,c) & \text{otherwise} \end{cases}$$

for $i \geq 1$ and $\tilde{g}_0(r,c) = g(r,c)$ and $\hat{g}_0(r,c) = g(r,c)$. That means once a pixel is marked or detected as a part of a dark feature it is ensured to remain a part of the

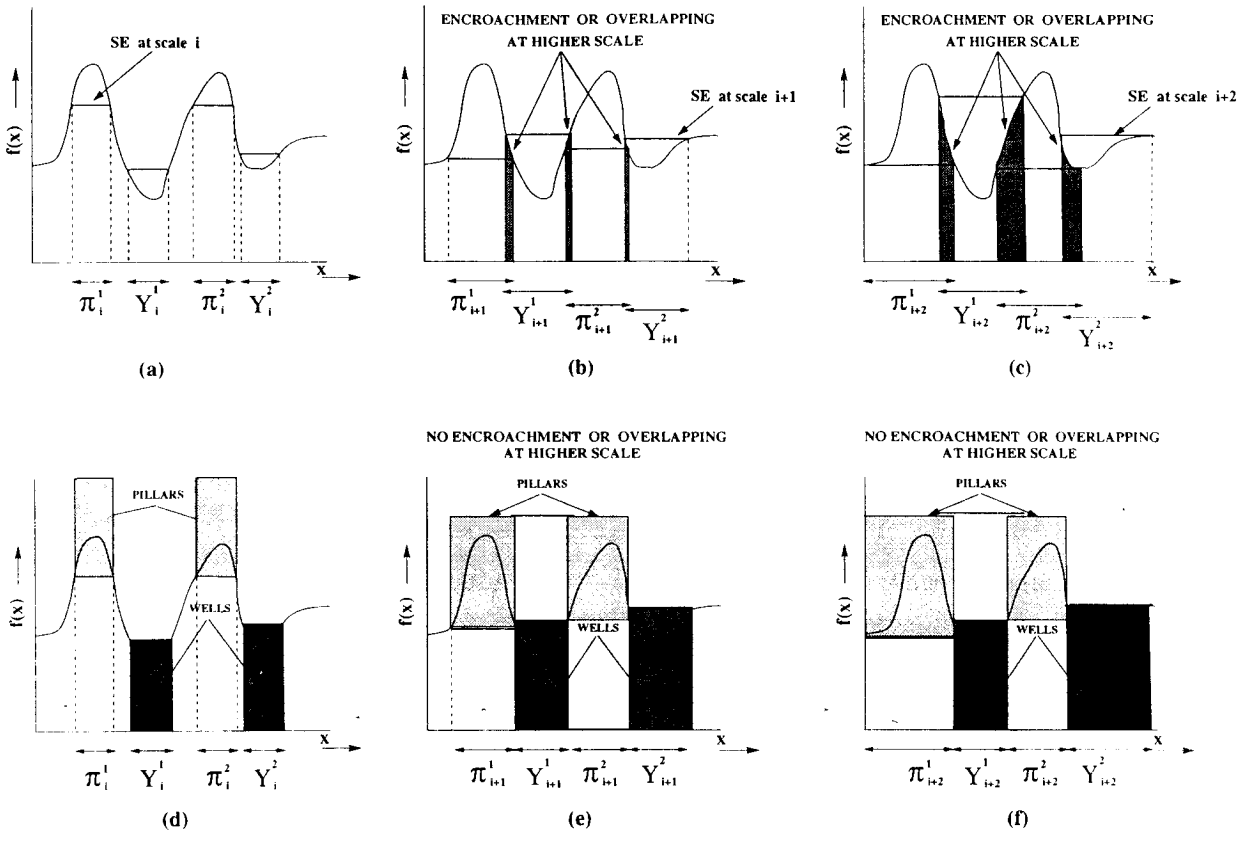

Figure 6.2: Illustration of encroachment

same dark feature at all higher scales by digging an well of infinite depth at that point. In a similar way, a pixel, once marked or detected as a part of a bright feature at a given scale, is ensured to remain a part of the same bright feature at all higher scales by raising a pillar of infinite altitude at that point. As a result, the possibility of a pixel being a part of a dark as well as a bright feature simultaneously is totally excluded and thus, the encroachment problem is also avoided.

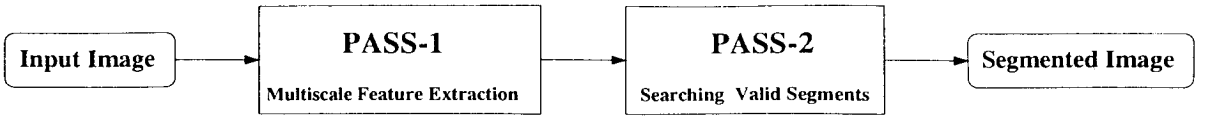

Figure 6.3: The stages of proposed multi-scale image segmentation algorithm

6.2.2 Implementation

The proposed algorithm starts with a *preprocessing* step as described below. The segmentation scheme is divided into two passes (see fig. 6.3) namely (i) *multi-scale region extraction* and (ii) *selection of valid regions that contribute to final segmentation.* Following subsections present them elaborately.

Preprocessing

A segmentation algorithm often needs a preprocessing step like noise smoothing to reduce the effect of undesired perturbations which might cause over- and under-segmentation. For example, *Gaussian* filtering is employed in *Marr-Hildreth* [95] and *Canny's* edge detector [26]. The very small scale details (i.e. the sudden discontinuity in gray-value over very small regions) are usually considered as noise. It is a necessity to estimate the scale (or size) of noise particles before removing them. Interested reader may refer to [117] for such analysis. However, the main concern, here, is the segmentation and we have used a morphological method which smooths out noise by applying iterative filtering until the spatial variation of intensity becomes locally monotonic with respect to the SE. The steps of the preprocessing operations are

(1) Perform conventional morphological opening and closing on the input image using an SE of small size. The size of the SE is greater than that of noise

particles.

(2) Construct the output image by averaging the images resulting after opening and closing.

(3) Compare the output image with the input image. If they are identical then halt. Otherwise consider the output image as the input image to the next iteration and go to step (1).

The algorithm for preprocessing step is as given below. In this particular algorithm all morphological operations i.e. opening and closing are conventional and do not employ reconstruction.

Procedure *remove_small_scale_details()*
input: $g_{in}[][]$; /* the input image */
output: $g_{out}[][]$; /* the output image after smoothing */
var: $g_{op}[][]$, $g_{cl}[][]$; /* intermediate images */
boolean: $flag$
$flag \leftarrow$ false;
begin
repeat
$g_{op} \leftarrow open\_image(g_{in})$;
$g_{cl} \leftarrow close\_image(g_{in})$;
$g_{out} \leftarrow average(g_{op}, g_{cl})$;
if($g_{in} = g_{out}$) $flag \leftarrow$ true; /* pixel-wise comparison*/
$g_{out} \leftarrow g_{in}$;
until $flag$=true;
end begin
end Procedure

Similar approach may be found in [23]. The main problem of this approach is to

determine the size of SE. Based on the domain knowledge and sensor parameters (namely, resolution and magnification factor) minimum size of the features of interest in the image can be determined in terms of pixels. Any feature of size smaller than that may be treated as noise. Size of isotropic SE to eliminate such noise can then simply be computed

Pass-1 : Multi-scale region extraction

The preprocessed image is the input to the first pass of our segmentation algorithm. In this pass information about potential bright and dark regions at different scales are collected by executing an alternate sequence of opening and closing by reconstruction on the preprocessed image (see fig 6.4). The bright top-hat image resulting after opening at scale i is thresholded at level 0. The resultant binary image contains all possible bright features in the image. However, all these features are not visually discernible. Only those features that have sufficient contrast with respect to its immediate background can readily be identified. Suppose Π_i^j is a component in the resultant binary image. Then local contrast is measured as

$$LC(\Pi_i^j) = [max\{g(r,c) \mid (r,c) \in \Pi_i^j\}] - [min\{g(r,c) \mid (r,c) \in \Pi_i^j\}] \qquad (6.19)$$

If the contrast is less than some specified threshold k, the feature is not visually discernible and the corresponding component is filtered out. Finally, the filtered binary image is kept in the $i-th$ cell of the *bright_feature_tower* . This binary image is then used as a mask for spatial locations of the input image where pillars of infinite altitude require to be erected according to equation (6.17). The modified or updated input image is then subjected to closing with reconstruction at scale i. Then proceeding in the similar way as described in case of opening a filtered binary image is obtained which is kept in the $i-th$ cell of the *dark_feature_tower*. This binary image too is used as a mask for spatial locations of the input image where we require to dig

wells of unreachable depth according to equation (6.18). Here, for practical purpose the height of pillars and depth of wells are chosen as 255 and 0 respectively for 8-bit image. The erection of pillars and excavation of wells are performed using

$$g(r,c) = \begin{cases} MAXVAL & \text{if } (r,c) \in \Pi_i \text{ and } LC(\Pi_i^j) \geq k \\ g(r,c) & \text{otherwise} \end{cases}$$

and

$$g(r,c) = \begin{cases} MINVAL & \text{if } (r,c) \in \Upsilon_i \text{ and } LC(\Upsilon_i^j) \geq k \\ g(r,c) & \text{otherwise} \end{cases}$$

where $MINVAL = 0$ and $MAXVAL = 255$ and k is a threshold value.

The steps in the multi-scale region extraction are as given below. The following steps are performed starting with the preprocessed image as input.

(1) The image is opened with reconstruction with a disk SE B. The bright top-hat image obtained by subtracting the opened image from the input image is then thresholded at the level 0. Components that do not have sufficient local contrast are then discarded. The resulting binary image $g_i^{top\_bin}$ consists of black blobs corresponding to visually discernible bright features. It is then stored in the i-th level in the *bright_feature_tower*.

(2) The binary image $g_i^{top\_bin}$ is then used as a mask for erecting pillars in the input image to prevent encroachment. The gray value of each pixel in the input image masked by this binary image is changed to 255.

(3) The modified input image is closed with reconstruction with the same SE B. The dark top-hat image is subjected to the same operations as in case case of bright top-hat image in step (1). As before, the resulting binary image $g_i^{bot\_bin}$ is saved in the $i - th$ cell in the *dark_feature_tower*.

(4) The binary image $g_i^{bot\_bin}$ is then used as a mask for digging wells in the input image to prevent encroachment. The gray value of each pixel in the input image masked by this binary image is changed to 0.

(5) Select the next higher homothetic of the SE B and if it is not larger than that at the prescribed largest scale, go back to step [(1)]. Otherwise halt.

The algorithm for multi-scale region extraction is as given below.

Pass-1 : Multi-scale feature extraction

Procedure *Extract_multi-scale_features()*

input: $g_{in}[][]$; /* the original preprocessed input image */

output: bright_feature_tower, dark_feature_tower; /* towers of filtered images */

constant: $MAXSCALE$; /* upper bound of scale factor */

constant: k; /* threshold parameter */

var: $g_i^{op}[][]$, $g_i^{cl}[][]$; /* intermediate images */

var: $g_i^{top}[][]$, $g_i^{bot}[][]$, $g_i^{top\_bin}[][]$, $g_i^{bot\_bin}[][]$; /* intermediate images */

integer: i;

$i \leftarrow 1$;

begin

repeat

$g_i^{op} \leftarrow open\_with\_reconstruction(g_{in}, iB)$;

$g_i^{top} \leftarrow g_{in}$ - g_i^{op};

$g_i^{top\_bin} \leftarrow threshold(g_i^{top}, 0)$;

$g_i^{top\_bin} \leftarrow delete\_trivial\_component(g_i^{top\_bin}, g_i^{top}, k)$;

$insert\_in\_tower(g_i^{top\_bin}, bright\_feature\_tower, i)$;

$g_{in} \leftarrow erect\_pillars\_at\_masked\_regions(g_{in}, g_i^{top\_bin})$;

$g_i^{cl} \leftarrow close\_with\_reconstruction(g_{in}, iB)$;

$g_i^{bot} \leftarrow g_i^{cl}$ - g_{in};

$g_i^{bot\_bin} \leftarrow threshold(g_i^{bot}, 0)$;

$g_i^{bot\_bin} \leftarrow delete\_trivial\_component(g_i^{bot\_bin}, g_i^{bot}, k)$;

$insert\_in\_tower(g_i^{bot\_bin}, dark\_feature\_tower, i)$;

$g_{in} \leftarrow dig\_wells\_at\_masked\_regions(g_{in}, g_i^{bot\_bin})$;

$increase\ i$;

until $i > MAXSCALE$;

end begin

end Procedure

Pass-2 : Selection of valid regions that contribute to final segments

After building the towers in the first pass the second pass of the algorithm is executed for selecting the valid segments at various scales that contribute to the final segmentation. By the term "valid segments" we mean either a self-contained complete object or a well-defined part of an object. The former is indicated by saturation of domain of support, while the latter by merging. The closed contours of such regions are traced out and combined together to obtain the final result.

In the second pass the valid segments corresponding to the bright features at various scales are searched using the binary images kept in *bright_feature_tower* constructed in the first pass. The steps are

We start with the image pair at the lower-most cells in the *bright_feature_tower*, set $i = 1$ and g_{bright_cont} to *null image*.

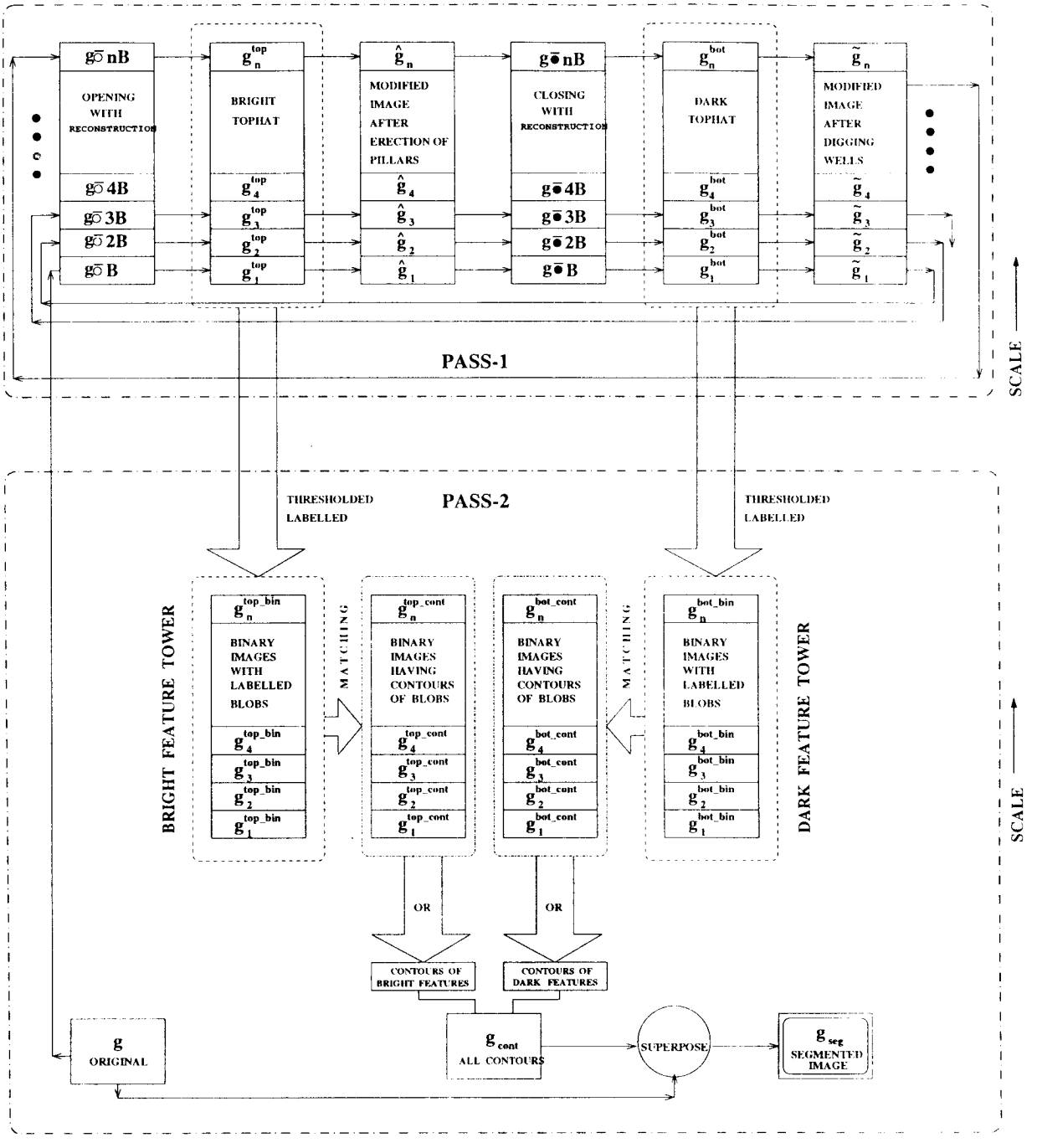

Figure 6.4: Schematic diagram for multi-scale image segmentation using morphological towers

(1) Consider the $i-th$ and $(i+1)th$ binary images in the *bright_feature_tower*. Label the components of the images using any standard connected component labeling algorithm [131].

(2) Modify the binary image $g_i^{top\_bin}$ by deleting its all components except those which (i) are identical in both the labeled images $g_i^{top\_bin}$ and $g_{i+1}^{top\_bin}$ and (ii) merge into a single component of the second labeled image $g_{i+1}^{top\_bin}$ over nearly same spatial locations.

(3) Trace the contours of the objects in binary image $g_i^{top\_bin}$ modified in the previous step using any standard edge detection algorithm for binary images [131]. Let $g_i^{top\_cont}$ be the corresponding edge images.

(3) Take the cumulative set-theoretic union of the images g_{bright_cont} and $g_i^{top\_cont}$

(4) Increase i. If $(i+1)$ is greater than the height of the tower, halt . Else go back to step [(1)].

The image g_{bright_cont} contains the closed contours of all prominent bright features in the input image.

We perform similar set of operations [i.e. steps (1)-(6)] with all successive pairs of binary images in the *dark_feature_tower* and construct a similar edge image g_{dark_cont} corresponding to all the dark features present in the input image. Finally, the image g_{cont} is obtained by taking set-theoretic union of g_{bright_cont} and g_{dark_cont}. The image g_{cont}, therefore, contains the closed contours of all bright and dark features present in the image and is the result of the proposed scheme.

The algorithm is as given below.

Pass-2 : Detection and tracing the segmenting contours at different scales

Procedure*Detect_and_trace_contours()*

input: bright_feature_tower, dark_feature_tower; /* the towers obtained in Pass-1 */

output: g_{cont}; /* the image containing the segmentation result */

constant: $MAXSCALE$; /* upper bound of scale factor */

var: $g_i^{temp1}[][], g_i^{temp2}[][], g_i^{temp3}[][], g_i^{top\_cont}[][], g_i^{bot\_cont}[][]$; /* intermediate images */

var: $LIST1$, $LIST2$; **ordered list** of components

integer: i;

$i \leftarrow 1$;

begin

repeat

$g_{temp1} \leftarrow get\_image(bright\_feature\_tower, i)$;

$g_{temp2} \leftarrow get\_image(bright\_feature\_tower, i+1)$;

$LIST1 \leftarrow label\_components\_of(g_{temp1})$;

$LIST2 \leftarrow label\_components\_of(g_{temp2})$;

$g_{temp3} \leftarrow image\_with\_saturated\_and\_merging\_components(LIST1, LIST2)$;

$g_i^{top\_cont} \leftarrow trace\_contours(g_{temp3})$;

$g_{temp1} \leftarrow get\_image(dark\_feature\_tower, i)$;

$g_{temp2} \leftarrow get\_image(dark\_feature\_tower, i+1)$;

$LIST1 \leftarrow label\_components\_of(g_{temp1})$;

$LIST2 \leftarrow label\_components\_of(g_{temp2})$;

$g_{temp3} \leftarrow image\_with\_saturated\_and\_merging\_components(LIST1, LIST2)$;

$g_i^{bot\_cont} \leftarrow trace\_contours(g_{temp3})$;

$g_{cont} \leftarrow g_{cont} \cup g_i^{top\_cont} \cup g_i^{bot\_cont}$;

increase i;

until $i > MAXSCALE$;

end begin

end Procedure

6.3 Experimental Results and Discussions

The proposed algorithm has been executed on a set of images. Some results are shown in figs. 6.5 - 6.8. Figures 6.5(a) - 6.8(a) show some of the test images used in the experiment. The images in fig. 6.5(a) and fig. 6.6(a) are synthetic images depicting dark and bright spheres of arbitrary radii. The image in fig. 6.6(a) is generated by corrupting the image in fig. 6.5(a) with random noise. Fig. 6.7(a) and 6.8(a) represent real images of blood cells and skin lesions respectively. The results produced by the proposed multi-scale morphological segmentation algorithm are shown in fig. [6.5-6.8](b). The results have been compared with those of two other well known methods. Figures [6.5-6.8](c) show the respective results of Canny's edge based segmentation technique. The results of basic watershed segmentation (BWSD) algorithm are shown in figures [6.5-6.8](d) in the identical order. Oversegmentation is a known drawback of the basic watershed algorithm [145]. The marker-controlled watershed is known to provide an effective solution to the oversegmentation problem [104, 126]. In so-called marker-controlled watershed algorithm only a subset of minima (the marked minima) is allowed to evolve into catchment basins. Similar results may be obtained by choosing an appropriate flooding step size for the advancement of the intensity (or gradient) level [163]. We have compared our results also with that of marker-controlled watershed (MWSD) algorithm provided by Volkmann [163] in two-dimension. Results MWSD are shown in figures [6.5-6.8](e). Contours obtained due to different methods are superposed on the respective original images for testing the efficacy of the methods. Table 6.1 shows the values of different parameters used in the experiment in order to produce visually optimum results in each case. It is important to observe the results in somewhat a greater detail to compare the performance. For subjective evaluation of performance of the said methods we concentrate on the following qualities of the segmentation results and judge them visually.

(a) *Continuity or encompassing in the extracting contours:* The segmenting contours in case of all the images resulting due to the proposed method are closed and continuous [see fig [6.5-6.8](b)]. So are the results of marker-controlled watershed [see fig [6.5-6.8](e)]. The contours produced by the basic watershed algorithm are not always continuous and closed as can be seen in fig. [6.6-6.8](d). The contours produced by Canny's edge based technique in all the resulting images are mostly discontinuous and open [see fig [6.5-6.8](c)]..

(b) *Mutual exclusion of different adjacent segments:* The significant regions are successfully separated by contours in case of the images produced by the proposed method. There is no encroachment among different adjacent segments in the output images produced by the proposed method. Mutual exclusion in regions are also observed in the results of both the BWSD and the MWSD algorithm. However, in some cases of BWSD, a part of an object has appeared to be claimed simultaneously by more than one segment [see fig. 6.5(d) and fig. 6.8(d)]. Such requirement may not be attained by Canny's method due to presence of open contours.

(c) *Over- and under-segmentation:* The results of the proposed method are nearly free from the problem of over- and under-segmentation. This is also true for MWSD algorithm, except presence of under-segmentation in a few cases [see fig [6.7-6.8](e)]. The problem of over-segmentation is grossly present in case of basic watershed algorithm as mentioned earlier [see fig [6.6-6.8](d)]. Canny's method, has however, produced improperly segmented output images in this respect.

(d) *Emphasis on sub-features:* The proposed method has given emphasis on sub-features. The relatively smaller darker (respectively brighter) sub-regions within relatively larger dark (respectively bright) regions have been contoured separately. This has however, not happened with other methods.

(e) *Emphasis on shape and scale:* Primary emphasis on shape and scale has been given in case of the proposed method. Emphasis on scale only is given in the case of Canny's edge based technique. No emphasis on shape and scale is given by the watershed algorithms considered here.

(f) *Other overheads:* The proposed method has largest time and space-complexity. It makes use of two control parameters *viz.* k and $MAXSCALE$ and checks. However, the results do not depend strongly on the choice of the threshold (k) for local contrast. Secondly, $MAXSCALE$ is chosen trivially based on the maximum size of objects we are interested in, just to reduce time complexity. In case of basic watershed algorithm the selection of initial marker points is a crucial overhead on which the results depend seriously. In marker-controlled watershed (MWSD) algorithms either the minima are selected manually [104] which is a tedious work or some parameters are to be set [163]. The time complexity is also reasonably high in both the cases. In case of Canny's edge based technique two parameters namely the scale and the hysteresis are used to control the output. The space complexity is not as high as that of other methods considered here.

In a summarized form it is quite evident that the results produced by Canny's edge based segmentation technique are far behind than that of the proposed scheme as well the watershed algorithms for the class of images we consider. The basic watershed algorithm, however, produces over-segmentation in many cases. The performance of marker-controlled watershed (MWSD) algorithm surely better compared to that of BWSD. It should be noted that the watershed algorithms, when work directly on the intensity image, assume that all the objects are darker (or brighter) than the background [163]. If the darker as well as the brighter objects are present simultaneously present the watershed algorithms have to work on the gradient image [70], which is ill-defined in discrete domain and thus causes problem. Whereas, the proposed method

can directly work on the intensity image in both the above mentioned situations.

Table 6.1: Values of the parameters used in the experiment.

Serial No.	Fig. No.	Description of Image	MMS		CEST		MWSD
			minimum contrast (k)	maximum diameter of B	sigma	hysteresis	for all the images considered here
1	6.5(a)	bright and dark balls of different radii	5	43	0.742	35	low contour cutoff: 0.5 std. high contour
2	6.6(a)	noisy 7(a)	5	51	0.750	30	cutoff: 5.0 std.
3	6.7(a)	myelin	10	39	1.200	32	contour step
4	6.8(a)	skin lesions	11	59	1.000	40	size: 0.5 std.

MMS: Multiscale Morphological Segmentation, CEST: Canny's Edge based Segmentation Technique, MWSD: Marker-controlled Watershed algorithm [163]

6.3.1 Performance analysis

For the purpose of comparing the performance of the segmentation algorithms used in this work, we propose a simple measure based on similarity between the segmenting contours generated by the respective algorithms with the ideal ones. The synthetic image shown in fig. 6.5(a) consisting of bright and dark spheres of different radii is chosen as a reference image for performance analysis [and it is redisplayed in fig. 6.9(a)]. The contours corresponding to the ideal segmentation are shown in fig. 6.9(b). The contours produced by a segmentation algorithm must be very close or similar to the ideal ones.

Let I_{id} be the binary image which consists of the contours traced by the ideal segmentation algorithm. Let I_{sg} denote the binary image consisting of the contours traced by a segmentation algorithm. The pixel-wise *exclusive-OR* operation between these two images gives an idea about the mismatch in the contours present in the images.

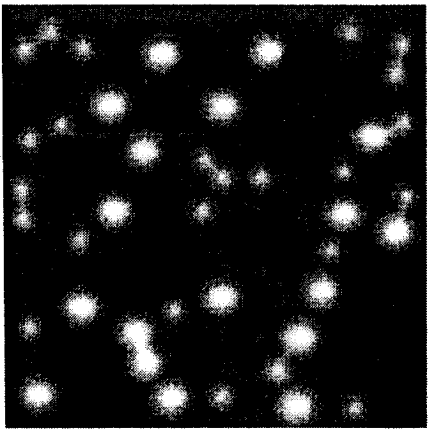

(a)

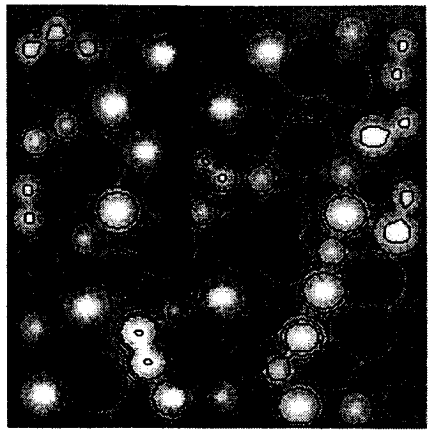

(b)

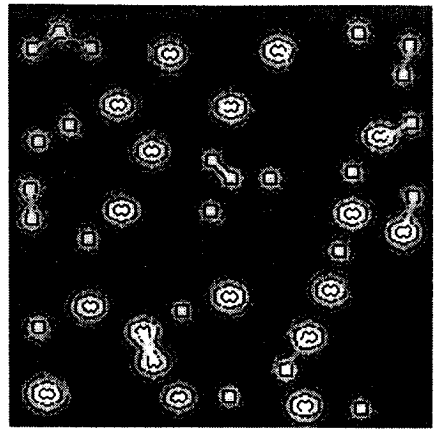

(c)

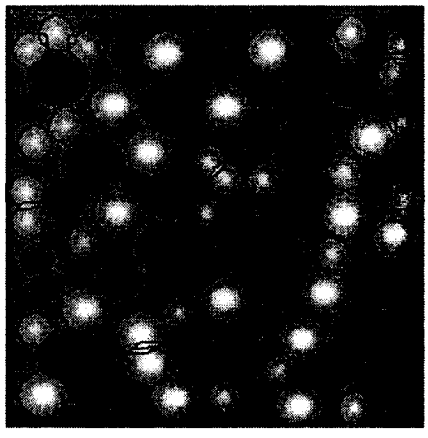

(d)

(e)

Figure 6.5: Results of segmentation. (a) (synthetic input) image of bright and dark balls of varying radii, (b)-(d) output images, (b) result of multi-scale morphological segmentation, (c) result of Canny's edge-based technique, (d) result of basic watershed segmentation, and (e) result of marker-controlled watershed segmentation.

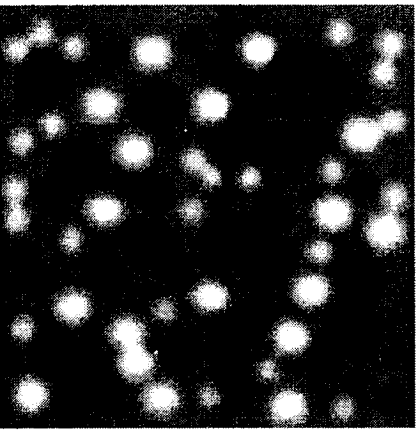

(a)

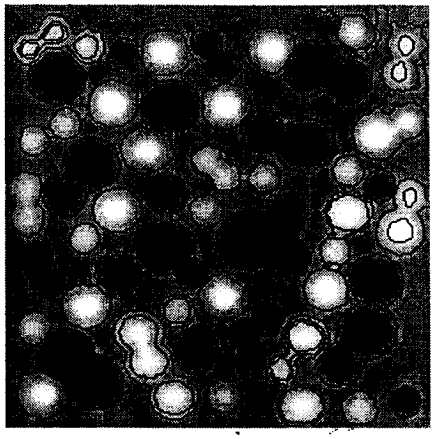

(b)

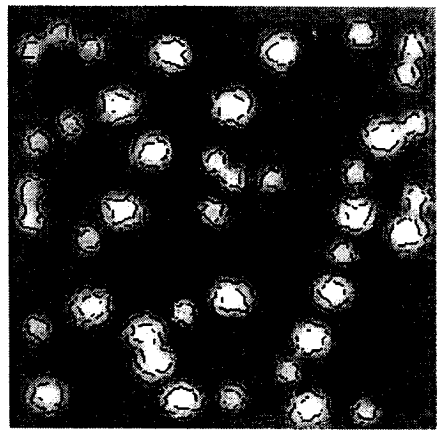

(c)

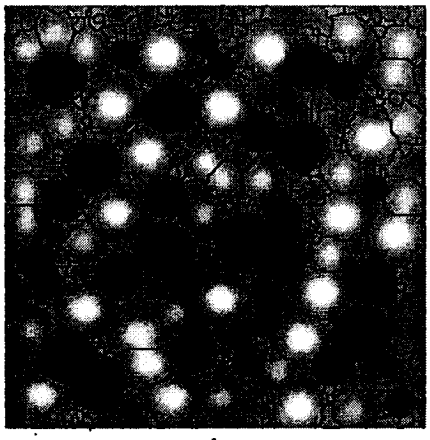

(d)

(e)

Figure 6.6: Results of segmentation (a) (input image) noise-corrupted version of the image shown in fig. 6.5(a), (b)-(d) output images, (b) result of multi-scale morphological segmentation, (c) result of Canny's edge-based technique, (d) result of basic watershed segmentation, and (e) result of marker-controlled watershed segmentation.

(a)

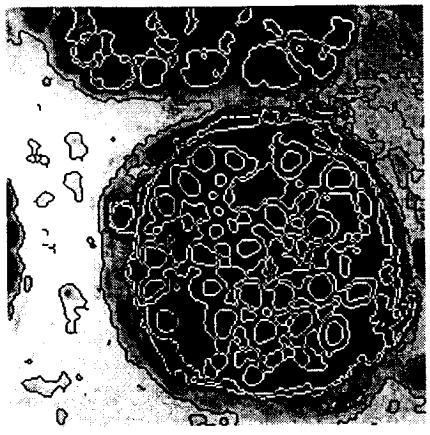

(b)

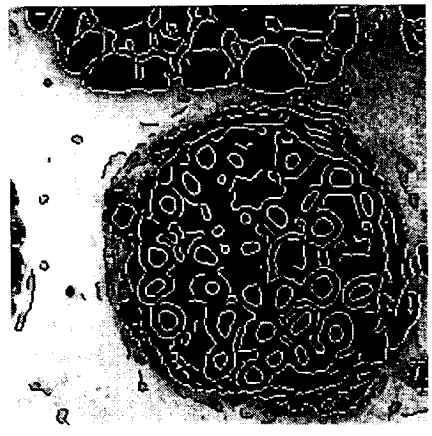

(c)

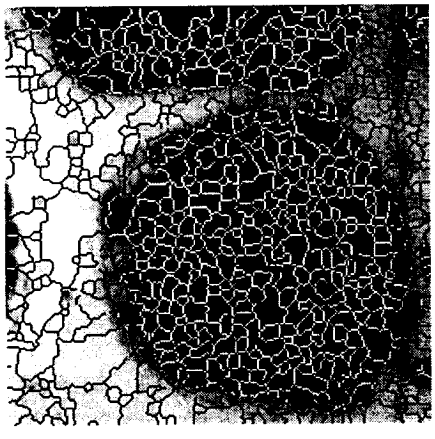

(d)

(e)

Figure 6.7: Results of segmentation (a) (input) image of myelin, (b)-(d) output images, (b) result of multi-scale morphological segmentation, (c) result of Canny's edge-based technique, (d) result of basic watershed segmentation, and (e) result of marker-controlled watershed segmentation.

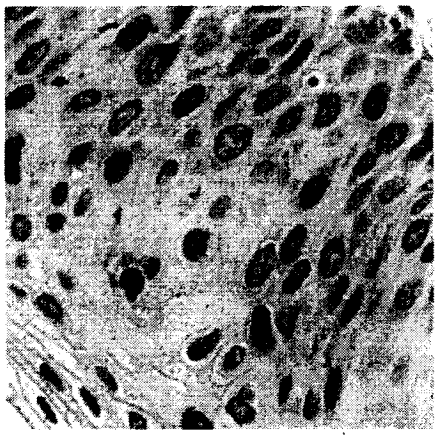

(a)

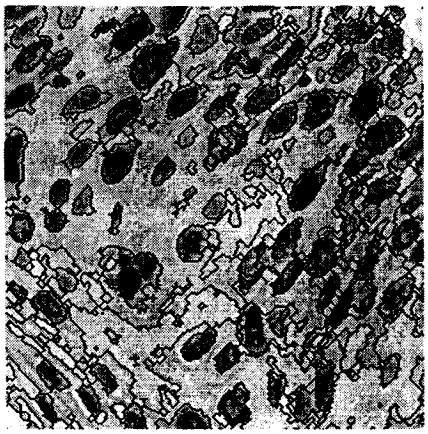

(b)

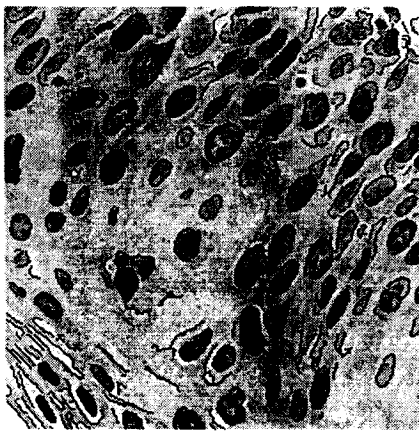

(c)

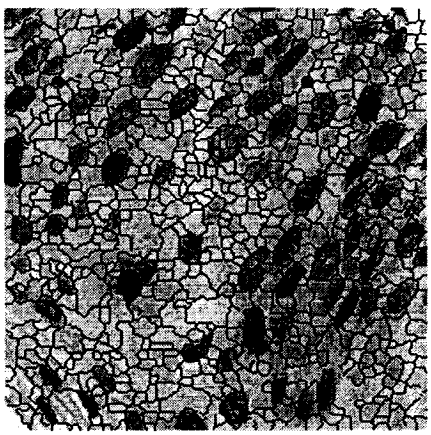

(d)

(e)

Figure 6.8: Results of segmentation (a) (input) image of skin lesions, (b)-(d) output images, (b) result of multi-scale morphological segmentation, (c) result of Canny's edge-based technique, (d) result of basic watershed segmentation, and (e) result of marker-controlled watershed segmentation.

Let I_{op} denote the image constructed by pixel-wise exclusive-OR operation between the images I_{id} and I_{sg} as shown below

$$I_{op}[r][c] = I_{id}[r][c] \tilde{\oplus} I_{sg}[r][c] \tag{6.20}$$

where $\tilde{\oplus}$ is the exclusive-OR operation and r, c are the spatial coordinates of the images.

If N_{id} and N_{op} be total number of black pixels in the images I_{id} and I_{op} respectively, we define the *correct segmentation factor* CSF as

$$CSF = \frac{N_{op}}{N_{id}} \tag{6.21}$$

The value of CSF should ideally be zero. However, a low value CSF indicates a good performance. Table 6.2 shows the values of CSF for algorithms executed on the image of fig. 6.9(a). Figure 6.9(b) shows the contour of the ideal segmentation (ground-truth) of (a). Fig. 6.10(a-d) show the contours produced by the proposed multi-scale morphological segmentation, Canny's edge based technique, basic watershed algorithm and marker-controlled watershed algorithm. The results of executing pixel-wise *exclusive-OR* operation of each of these images with the ideal contour image are shown in fig. 6.11(a-d). The presence of black pixels in these images indicates dissimilarity with ideal segmentation. This is also reflected in the corresponding CSF values in table 6.2.

The reason for high value of CSF in case of the proposed method may be explained easily. The proposed method emphasizes on segmenting sub-features. The high value of CSF is mainly contributed by the closed contours produced due to sub-features. To verify this, we have made a little modification in our algorithm. By adjusting the scale-parameter we can selectively remove the sub-features [please see fig. 6.10(d)]. As a result there is a significant improvement (i.e. reduction) in CSF as may be observed from table 6.2.

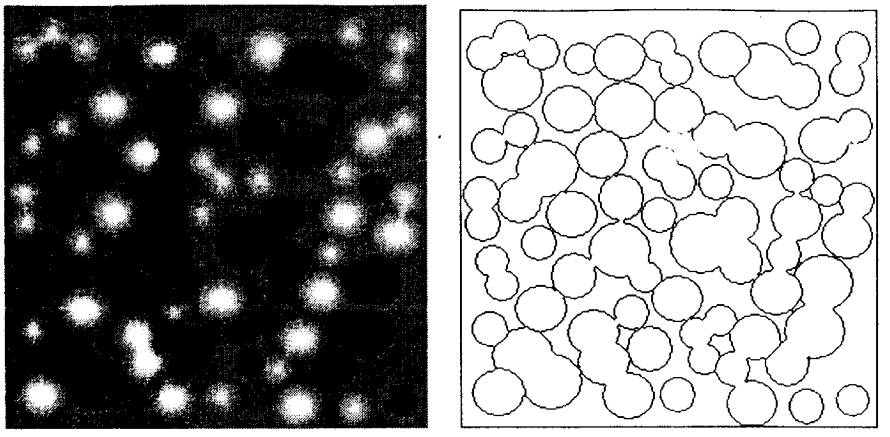

(a) (b)

Figure 6.9: (a) the input image and (b) the ideal segmentation.

In case of Canny's edge based technique the algorithm traces the contours along the points of *inflexion* where the second order spatial derivative of the image is zero. As a result the contours are bit shifted from the ideal ones and hence it results in high value of CSF.

In case of watershed algorithms too the reason for relatively higher value of CSF may be explained. In watershed algorithm the pixels of two different catchment basins require different labeling. A pixel equidistant from two adjacent catchment basins require an arbitration as it may be simultaneously claimed by both of them. The arbitration causes a shift in waterlines (i.e., the segmenting contours). As a result the CSF increases to a higher value. In case of MWSD, because of the step size (not equal to one) the algorithm may miss the contour at its exact location. As a result, waterlines are extracted at a few pixels apart from the ideal contour as seen in figure 6.11(d). This results in even higher value of CSF for MWSD. However, this is not a serious problem because much better localized contour may be obtained by reducing the step size, and consequently the value of CSF would be improved.

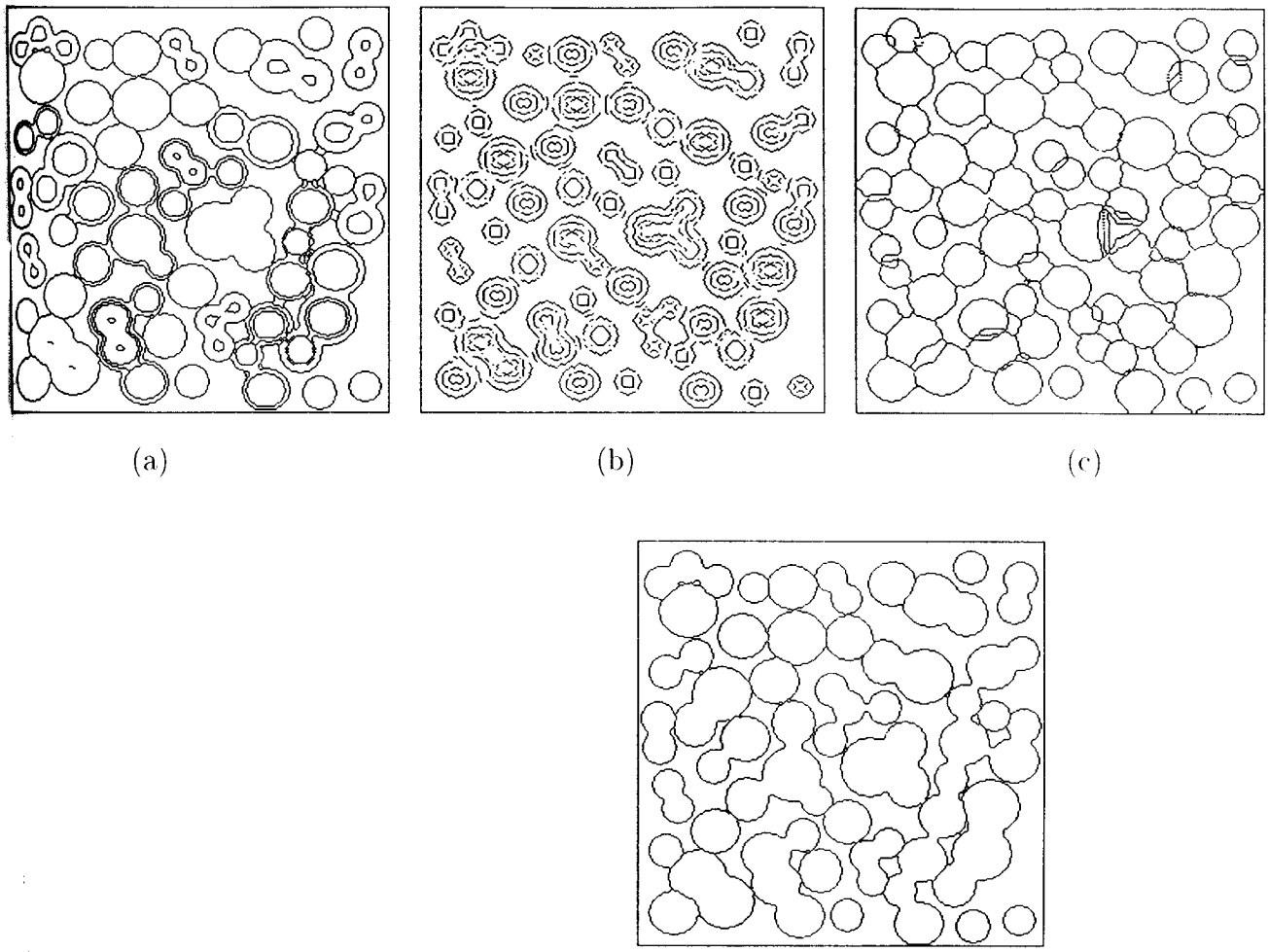

Figure 6.10: Segmentation contours traced by (a) multi-scale morphological segmentation, (b) Canny's edge-based segmentation, (c) basic watershed segmentation, (d) marker-controlled watershed segmentation, and (e) multi-scale morphological segmentation with no emphasis on sub-features.

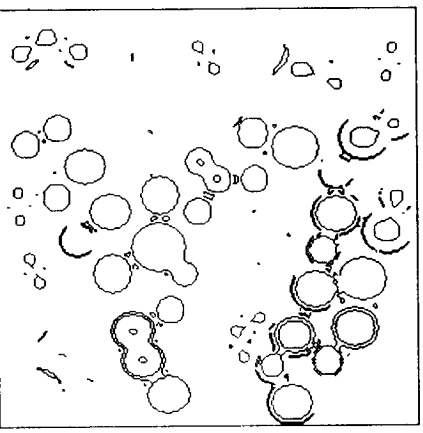

(a)

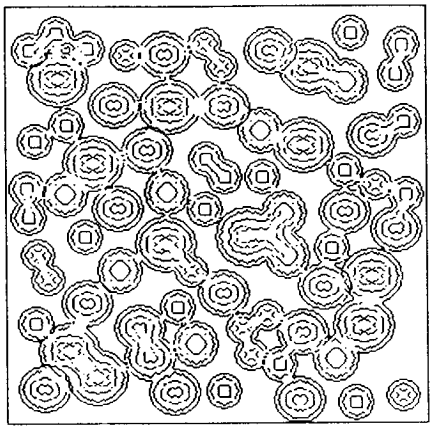

(b)

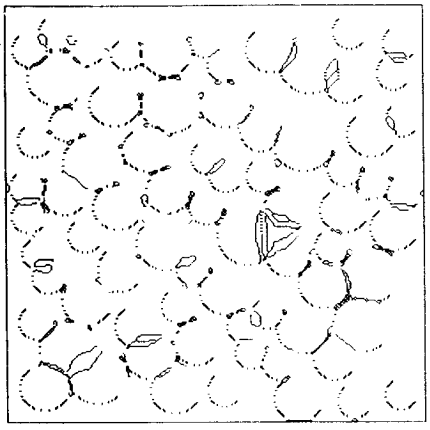

(c)

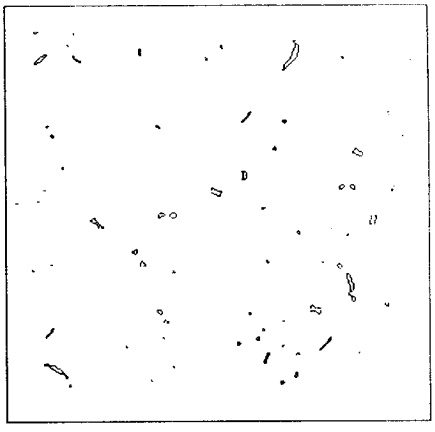

(d)

(e)

Figure 6.11: Images generated by pixel-wise exclusive-OR operation between the ideally segmented image and the image generated (a) multi-scale morphological segmentation, (b) Canny's edge-based segmentation, (c) basic watershed segmentation, (d) marker-controlled watershed segmentation, and (e) multi-scale morphological segmentation with no emphasis on sub-features.

Table 6.2: Relative performance of the segmentation algorithms

Correct Segmentation Factor CSF				
$MMS-I$	$CEST$	$BWSD$	$MWSD$	$MMS-II$
1.6957	2.6019	1.4645	1.7566	0.1280

MMS-I: Multiscale Morphological Segmentation, CEST: Canny's Edge based Segmentation Technique, BWSD: Basic Watershed algorithm, MWSD: Marker-controlled Watershed algorithm, MMS-II: Multiscale Morphological Segmentation with no emphasis on sub-features.

6.4 Conclusion

In this chapter we have proposed a scheme for segmenting gray-level images of cluttered objects of different shape and size. This multi-scale morphological method is expected to work satisfactorily on gray-level images containing bright and dark features of various scales. The scheme starts with simplifying the image in the preprocessing step. In the first pass the algorithm collects potential regions at various scales resulting after morphological filtering by reconstruction in different towers. In the second pass the algorithm compares pair of feature images corresponding to two successive scales and selects the potential regions that contribute to the formation of valid segments based on three criteria namely, *growing, merging* and *saturation.* Finally the contours of all such potential regions are integrated. The results of the proposed scheme have been compared with those of two other well known methods namely watershed algorithm and Canny's edge-based algorithm. The positive features of the proposed scheme is that it is *shape* and *edge preserving, scale-calibrated.* However, the CPU time and memory space requirement of the scheme are relatively higher. The proposed scheme being inherently parallel might improve this short-

coming after suitable parallel implementation. However, it should be noted that the watershed algorithms, when work directly on the intensity image, assume that all the objects are darker (or brighter) than the background. If the darker as well as the brighter objects are present simultaneously present the watershed algorithms have to work on the gradient image, which is ill-defined in discrete domain and thus causes problem. Whereas, the proposed method can directly work on the intensity image in both the above mentioned situations.

In chapters 3-6 we have presented application of morphological towers to a number of well known problems in image processing. The performance in each case is found to be quite satisfactory and in some cases better than other known algorithms. In the next chapter we present the concluding discussions on the entire thesis work.

Chapter 7

Conclusions

Multi-scale image processing techniques have become quite popular in recent years. In this context our works on multi-scale processing are quite relevant. The multi-scale representation of gray-level image adopted in this thesis for image processing and analysis is given in equation (2.43) obtained from [160], [98] and [86]. This is a special case of well-known granulometry using structural opening and closing by reconstruction with convex structuring elements of increasing scale. The said representation is implemented here as a stack of morphologically filtered images of same size and is referred by *morphological tower*. Then the proposed implementation has been employed as a *tool* to solve a number of problems in image processing. Thus the morphological tower is a stack of morphologically filtered images (i.e. the feature images at different scales) using a family of structuring elements of increasing scales. The objects in the feature images are thus scale-calibrated. The conceived morphological tower has been analyzed from the perspective of scale-space filtering. The conditions namely *causality, edge localization, isotropy, scale-calibratedness* etc. are found to be satisfied. In addition, morphological tower unlike other scale-space representation like *pyramid* does not involve construction of sub-sampled or interpolated

(i.e. super-sampled) image.

We have employed morphological tower in solving a number of standard problems in image processing. These include (i) noise smoothing, (ii) local contrast enhancement of graylevel images, (iii) local contrast enhancement of color images, (iv) multimodal image fusion and (v) segmentation of graylevel images. In all cases, the basic methodology adopted is same. Solving a problem using morphological tower consists of three main stages.

In the first stage we construct a set of morphological towers which stacks the scale-specific bright and dark features extracted employing multi-scale morphological filters.

In the second stage the feature images in the towers may need to undergo further analysis. For example in case of multi-modal image fusion (chapter 5) the feature images extracted from different modalities are mutually compared. In case of segmentation (chapter 6) the feature images in the towers are subjected to component level analysis.

In the third stage, the final (i.e. the result) image is constructed by integrating the feature images of the morphological towers in a suitable way. The integration of feature images of different scales are integrated following simple arithmetic operations (like addition, subtraction, recursive averaging etc). The process of integration of feature images for each of the applications mentioned above depends on the purpose of the concerned application. In the integration process the contribution of feature information from the scale-space filtered images are realized in terms of judiciously chosen weight factors. In all cases these weight factors are set by simple and straightforward combination of the feature images in the towers. For example, in case of noise smoothing (please see section 3.2.1 in chapter 3) the recursive average starting at the bottom of the tower assigns smaller weights to features of small scales which is a basic requirement of smoothing random noise from gray-level images. In case of

contrast enhancement (chapter 3) and color enhancement (chapter 4) the feature images are combined with more weights assigned to the images at smaller scales so that the resulting enhanced image highlights the smaller features more intensely. This is accomplished simply by cumulative addition of multi-scale top-hat images. In case of fusion and segmentation (chapters 5, 6) integration of features is realized through simple addition or subtraction. The simple and straightforward combination of the scale-space images in the towers is an attractive feature of the tool conceived in the thesis. Morphological tower is also sensitive to shape of the features.

In each application presented from chapter 3 through 6, the basic problem has been analysed from the perspective of multi-scale approach. Then a theoretical formulation of the solution of that particular problem in the framework of morphological tower has been built up. The algorithms are then implemented on morphological towers. and tested on several images.

In case of noise smoothing (chapter 3), we have studied the performance of the proposed algorithm in smoothing seven kinds of noise namely *Exponential, Gaussian, Poisson, Rayleigh, Shot, uniform* and *speckle noise*. The proposed algorithm has been found to work reasonably good. The experimental results have been compared [please see fig. 3.4] with those of other standard filters namely *median filters* [131], *Crimmin's filter* [35] and *anisotropic diffusion smoothing filter* [165, 123]. The performance metrics like *signal to noise ratio, deviation in mean busyness* and *correct processing ratio* have been computed for each method for comparing the performance [please see tables (3.3 - 3.5)]. We have also modified the proposed algorithm considering noise statistics into account. The modified scheme ($MMS-2$) performs almost same as the original scheme ($MMS-1$). The variation of the measures SNR, DMB and the CPR with the largest scale factor n (i.e. the height of the tower) has been presented graphically [please see fig (3.5 - 3.7)].

In case of local contrast enhancement of gray-level images (section 3.5.1 in chapter 3) the basic principle has been extended in a multi-scale sense under the framework of morphological tower. The algorithm has been tested on a set of real images. For the sake of comparison, other standard algorithms like *local contrast enhancement based on local statistics* [119], *local histogram equalization* [53] and the method due to *Dorst* [39] are executed on the same set of images. From the experimental result [please see fig. (3.12 - 3.14)] it is observed that the proposed method performs better than the other methods. The features are enhanced without appreciable enhancement of noise particles.

In case of contrast enhancement of color image (chapter 4), we extend the previous algorithm with the objective of preserving the hue of the color image. The algorithm is tested on several color images. The results are compared with two other standard methods (based on *genetic algorithm* [144] and *pyramids* [156]). From the results [please see figs. (4.6-4.9)] it is observed that the proposed method has performed reasonably better as compared to other methods. A quantitative measurement of color enhancement (*the overall contrast*) has been computed for the result images of all the methods. The proposed method is found to be the best according to the quantitative measurement [please see table 4.1]. A graphical plot of the overall contrast against the largest scale factor is also presented [fig. 4.10]. The proposed multi-scale method preserves hue and saturation of the color image.

In case of multi-modal image fusion (chapter 5), the selection of prominent features at each scale is guided by mutual comparison of the feature images of both the modalities. The proposed algorithm is tested on a pair of MR and CT images. The method performs registration of the images prior to fusion. The result of the proposed algorithm is compared with that produced by three other methods namely fusion employing simple averaging, KL transformation [53] and *pyramid* [97] [please see fig. 5.4]. For quantitative analysis we have provided a measure called *degree*

of fusion. It is observed that the degree of fusion is maximum for the proposed method [please see table 5.1]. The same fusion scheme is executed using (i) only multi-scale opening and (ii) only multi-scale closing instead of both multi-scale opening and closing simultaneously. The result has been found to be better in case of multi-scale opening and worse in case of only closing. These two methods however, emphasize on either bright or dark features and not on both.

In case of gray-level image segmentation (chapter 6), the concepts of region-based techniques have been extended under the framework of proposed morphological towers. The criteria of defining a valid segment are decided based on which the image is segmented. The algorithm has been tested on synthetic as well as real images. The results are compared with that of two other methods namely *Canny*'s edge-based technique [26], standard *watershed* [104] algorithm and marker-controlled watershed algorithm [163] [please see fig. 6.5-6.8]. The performance of the proposed algorithm has been found quite satisfactory. The output image resulting from the proposed method shows continuity of the segmenting contour, mutual exclusion of adjacent features, and emphasis on the sub-features. The result is free from over or under-segmentation. A performance (CSF) measure based on the mismatch between the segmenting contours produced by each method and that produced by ideal segmentation is also suggested.

The methods employing the morphological towers are parallel as far as the computation is concerned. It may be noted that the algorithms consume considerable space and time in sequential execution. But the parallel implementation on reconfigurable architecture (using FPGA) is expected to be reasonably fast. The shape of the structuring elements used in all the applications presented in the thesis is circular considering *function-* and *set-* processing [86]. These structuring elements have no directional property. However, structuring elements of different shape profiles may as well be used based on the requirement of the concerned application. The morphologi-

cal scale-space using such types of structuring element must satisfy the requirement of scale-space filters. Morphological towers may be constructed using other variants of morphological filters provided they satisfy the criteria of scale-space representation. In this sense the scope for employing morphological towers in problems related to image processing is wide-open. For example, morphological towers may be realized using area morphology [158, 159], soft morphology [46, 125]).

7.1 Future scope of work

In all the applications, we have chosen the maximum scale factor (i.e. the height of the tower) based on extensive observation of a large class of images. For example, in cases of noise smoothing, contrast enhancement (chapters 3-4) we have suggested low values of the maximum scale factor as the situation does not improve much appreciably beyond that for various reasons. In case of multimodal image fusion and segmentation (chapters 5 and 6) we, however, need to go for relatively higher scale factors. The selection of maximum scale factor, thus, depends on the content of the image under study as well as the concerned application. In all cases it has been selected to get a result which is visually optimum. One important problem as a continuation in the mainstream of the thesis work is to estimate mathematically the largest scale factor that one should use.

In this thesis we have employed morphological towers in solving some basic and fundamental problems in image processing. However, there is ample scope of exploring the applicability of morphological towers in many more problems. We enlist below some of the problems which we believe may be explored as a continuation of this work.

- Analytical derivation of range of scale

- More rigorous derivation of weight factors during the reconstruction of the image from its feature images
- Selective enhancement (like anisotropic diffusion) to avoid undue enhancement of noise
- Fusion of more than two images
- Fusion of color images
- Segmentation of color images
- Segmentation of texture images
- Visual cryptography and steganography
- Extension of application to 3D images

We have started to solve some of the above mentioned problems using morphological tower. The work is in progress and we look forward to establish the usefulness of the proposed multi-scale tool - the morphological tower.

Bibliography

[1] M. A. Abidi and R. C. Gonzalez. *Data fusion in Robotics and Machine Intelligence*. Academic Press Inc., Boston, 1992.

[2] E. Aboufadel and S. Schlicker. *Discovering Wavelets*. John Wiley and Sons, New York, 1999.

[3] R. Acharya and R. P. Menon. A review of biomedical image segmentation techniques. In *Deformable models in medical image analysis. edited by A. Singh, D. Goldgof and D. Terzopoulos, IEEE Computer Society*, pages 140–161, Los Alamitos, CA, 1998.

[4] S. T. Acton and A. C. Bovic. Nonlinear regression for image enhancement via generalized deterministic annealing. In *Proc. of the SPIE Symp. Visual Communication and Image Processing, Boston, November 7-12, 1993*, volume -, pages -, 1993.

[5] S. T. Acton, A. C. Bovic, and M. M. Crawford. Anisotropic diffusion pyramids for image segmentation. In *Proc. IEEE Int. Conf. Image Processing ICIP-94, Austin, November 13-16, 1994*, volume 3, pages 478–482, 1994.

[6] G. Agam, H. Luo, and I. Dinstein. Morphological approach for dashed line detection. In R. Kasturi and K. Tombre, editors, *First international workshop*

on graphics recognition - methods and applications, University Park, PA, USA, 1995, Lecture notes in Computer Science, pages 92–105. Springer, -, 1995.

[7] L. Alvarez, F. Guichard, P. L. Lions, and J. M. Morel. Axioms and fundamental equations of image processing. *Archive for Rational Mechanics*, 123(3):199–257, 1993.

[8] L. Alvarez and J. M. Morel. Formalization and computational aspects of image analysis. *Acta Numerica*, 123:1–59, 1994.

[9] H. Atmaca, M. Bulut, and D. Demir. Histogram based fuzzy kohonen clustering network for image segmentation. In *International Conference on Image Processing*, pages 18A6–, 1996.

[10] I. Attas, J. Louis, and J. Belward. A variational approach to the radiometric enhancement of digital imagery. *IEEE Transactions on Image Processing*, 4(6):845–849, 1995.

[11] S. Banerjee, D. P. Mukherjee, and D. Dutta Majumdar. Point landmarks for the registration of Ct and Mr images. *Pattern Recognition Letters*, 16:1033–1042, 1995.

[12] J. A. Bangham, T. G. Campbell, and R. V. Aldridge. Multiscale median and morphological filters for 2d pattern recognition. *Signal Processing*, 38:387–415, 1994.

[13] J. A. Bangham, P. Chardaire, C. J. Pye, and P. D. Ling. Multiscale nonlinear decomposition theorem. *IEEE Transactions on Pattern Analysis and Machine Intelligence*, 18:529–539, 1996.

[14] J. A. Bangham, R. Harvey, P. D. Ling, and R. V. Aldridge. Morphological scale-space preserving transforms in many dimensions. *Journal of Electronic Imaging*, 5(3):283–299, 1996.

[15] J. A. Bangham, P. D. Ling, and R. Harvey. Scale-space from nonlinear filters. *IEEE Transactions on Pattern Analysis and Machine Intelligence*, 18:520–528, 1996.

[16] A. Betti, M. Barni, and A. Mecocci. Using a wavelet-based fractal feature to improve texture discrimination on sar images. In *Proceedings of the 1997 International Conference on Image Processing (ICIP '97), October 26-29, 1997, Vol. 1*, pages –, Washington, DC, 1997.

[17] S. Beucher. Watersheds of functions and picture segmentation. In *Proceedings IEEE International Conference Acoustics, Speech and Signal Processing, Paris, France*, volume -, pages 1928–1931, 1982.

[18] I. Bloch. Information combination operators for data fusion : a review with classification. *IEEE Transactions on Systems Man and Cybernatics, Part A: Systems and Humans*, 26:52–67, 1996.

[19] G. Boccignone and A. Picariello. Multiscale contrast enhancement of medical images. *Proc. ICASSP'97, Munich, Germany, April 21-24*, 4:2789– , 1997.

[20] I. M. Bockstein. Color equalization method and its application to color image processing. *Journal of Opt. Soc. Am.*, A 3(5):735–737, 1986.

[21] R. V. D. Boomgaard and L. Dorst. *The Morphological Equivalent of Gaussian Scale-space, Gaussian Scale-space Theory.* Editor: J. Sporring, M. Nielsen, L. Florack and P. Johansen, Kluwer Academic Press, Netherlands, 1997.

[22] R. V. D. Boomgaard and A. Smeulders. The morphological structure of images: the differencial equations of morphological scale-space. *IEEE Transactions on Pattern Analysis and Machine Intelligence*, 16:1101–1113, 1994.

[23] J. H. Bosworth and Scott T. Acton. Morphological image segmentation by local monotonicity. In *Proc. of the Asilomar Conference on Signals, Systems, and*

Computers, Pacific Grove, California, October 24-27, 1999, volume 1, pages 53–57, 1999.

[24] R. W. Brockett and P. Maragos. Evolution equations of continuous-scale morphological filtering. *IEEE Transactions on Signal Processing*, 42:3337–3386, 1994.

[25] L. G. Brown. A survey of image registration. *ACM Computing Survey*, 24:325–376, 1992.

[26] J. F. Canny. A computational approach to edge detection. In M. A. Fischler and O. Firschein, editors, *Readings in Computer Vision: Issues, Problems, Principles and Paradigms*, volume -, pages 184–203. Morgan Kaufmann, -, 1986.

[27] B. Chanda, B. B. Chaudhuri, and D. Dutta Majumder. A modified scheme for segmenting noisy images. *IEEE Transactions on Systems, Man and Cybernetics*, 18(3):458–467, 1988.

[28] B. Chanda and D. Dutta Majumder. A note on use of gray-level co-occurrence matrix in threshold selection. *Signal Processing*, 15(2):149–167, 1988.

[29] B. Chanda and D. Dutta Majumder. *Digital Image Processing and Analysis*. Prentice-Hall of India Pvt. Ltd., New Delhi, 2000.

[30] B. chanda, S. Mukhopadhyay, and P. Ghosh. Multiscale morphological fusion of mr and ct images. In *Proc. ICVGIP-1998, New Delhi, India, Dec 21- 23,1998*, pages 21–26, New Delhi, India, 1998.

[31] M. Chen and P. Yan. A multiscaling approach based on morphological filtering. *IEEE Transactions on Pattern Analysis and Machine Intelligence*, 11:694–700, 1989.

[32] D. N. Chun and H. S. Yang. Robust image segmentation using genetic algorithm with a fuzzy measure. *Pattern Recognition*, 29:1195–1211, 1996.

[33] J. J. Clark and A. L. Yuille. *Data fusion for sensory information processing systems.* Kuwer Academic Publishers, Boston, 1990.

[34] A. Colligon, D. Vandermeulen, P. Seutens, and G. Marchal. Registration of 3d multimodality medical imaging using surfaces and point landmarks. *Pattern Recognition Letters*, 15:461–467, 1994.

[35] T. R. Crimmins. Geometric filter for speckle reduction. *Applied Optics*, -:24 . 1985.

[36] I. Daubechies. *Ten lectures on Wavelets.* Society of Industrial and Applied Mathematics, Philadelphia, 1992.

[37] L. Davis and A. Rosenfeld. Noise cleaning by iterated local averaging. *IEEE Transactions Systems, Man, and Cybernetics*, 8:1006–1010, 1978.

[38] H. Digabel and C. Lantuejoul. Iterative algorithms. In *Proceedings of the 2nd European Symposium Quantitative Analysis of Microstructures in Material Science, Biology and Medicine, Caen, France, 1977. Riederer Verlag, Stuttgart, 1978*, volume -, pages 85–99, 1978.

[39] L. Dorst. A local contrast enhancement filter. In *Proc. of the 6th Intl. Conference on Pattern recognition*, pages 604–606, Munich, Germany, 1982.

[40] M. Duff. Parallel processors for digital image processing. In P. Stucki, editor, *Advances in Digital Image Processing.* Plenum, New York, 1979.

[41] L. Floreby, F. Satter, and G. Salomonsson. Image enhancement by morphological pyramid decomposition and modified reconstruction. In *Proc. ICASSP'97*, pages 2585–2588, Munich, Germany, 1997.

[42] J. D. Foley, A. Van Dam, S. K. Feiner, and J. F. Hughes. *Computer Graphics Priciples and Practice.* Addison-Wesley Publishing Company, second edition, Reading, MA, 1997.

[43] R. J. Frank, T. J. Grabowski, and H. Damasio. Voxelvise percentage tissue segmentation of human brain magnetic resonance images (abstract). In *Abstracts, 25th Annual Meeting, Society for Neuro-science Society for Neuroscience, Washington, DC*, volume 1, pages 694–, 1995.

[44] K. S. Fu. A survey on image segmentation. *Pattern Recognition*, 13:3–16, 1981.

[45] A. Gady and I. Dinstein. Compound regulated morphological operations applied to map analysis. In *Proceedings of the third IAPR international workshop on graphics recognition, GREC'99, Jaipur, India, September 26-27*, pages 83–90, 1999.

[46] A. Gasteratos and I. Andreadis. Soft mathematical morphology: extensions, algorithms and implementations. In P.W. Hawkes (Editor), editor, *Advances in Imaging and Electron Physics*, volume 110(3), pages 63–99. Academic Press, San Diego, California, 1999.

[47] J. Gauch and C. W. Hsia. A comparison of three color image segmentation algorithms in four color spaces. In *Proceedings of the SPIE, SPIE, Bellingham, WA*, volume 1818, pages 1168–1181, 1992.

[48] M. J. E. Golay. Hexagonal parallel pattern transformations. *IEEE Transactions on Computer*, C-18:733–740, 1969.

[49] M. Goldberg and J. Zhang. Hierarchical segmentation using a composite criterion for remotely sensed imagery. *Photogrammetria*, 42:87–96, 1987.

[50] R. C. Gonzalez and B. A. Fittes. Gray-level transformations for interactive image enhancement. In *Proc. 2nd Conf. on Remotely Manned Systems*, pages 17–19, 1975.

[51] R. C. Gonzalez and B. A. Fittes. Gray-level transformations for interactive image enhancement. *Mechanism and Machine Theory*, 12:111–122, 1977.

[52] R. C. Gonzalez and P. Wintz. *Digital Image Processing, 2nd ed.* Addison-Wesley, Reading, MA, 1987.

[53] R. C. Gonzalez and R. E. Woods. *Digital Image Processing.* Addison-Wesley, Reading, MA, 1999.

[54] E. Gose, R. Johnsonbaugh, and S. Jost. *Pattern Recognition and Image Analysis.* PPrentice Hall of India, New Delhi, 1999.

[55] A. A. Goshtasby and J. L. Moigne. Image registration guest editor's introduction. *Pattern Recognition*, 32:1–2, 1999.

[56] J. Goutsias and S. Batman. Morphological methods for biomedical image analysis. In M. Sonka and J. M. Fitzpatric, editors, *Handbook of Medical Imaging, Vol-2, Medical Image Processing and Analysis*, pages 175–272. Spie Press, -, 2000.

[57] J. Goutsias and H. J. A. M. Heijmans. *Mathematical Morphology.* IOS Press, Ohmsha, 2000.

[58] J. Goutsias and H. J. A. M. Heijmans. Nonlinear multiresolution signal decomposition schemes - Part I: Linear and morphological pyramids. *IEEE Transactions on Image Processing*, 9(11):1862–1866, 2000.

[59] A. Gupta and B. Chanda. A hue preserving enhancement scheme for a class of color images. *Pattern Recognition Letters*, 17:109–114, 1996.

[60] E. L. Hall. *Computer Image Processing and Recognition.* Academic Press, New York, 1979.

[61] R. M. Haralick and L. Shapiro. Survey: Image segmentation techniques. *Computer, Vision, Graphics, and Image Processing*, 29:100–132, 1985.

[62] R. M. Haralick and L. G. Shapiro. *Computer and Robot Vision, Vol. 1.* Addison-Wesley, Reading, MA, 1992.

[63] R. M. Haralick, S.R.Sternberg, and Xnnhua Zhuang. Image analysis using mathematical morphology. *IEEE Transactions on Pattern Analysis and Machine Intelligence*, Pattern Analysis and Machine Intelligence-9(4):142–156, 1987.

[64] R. Harvey, A. Bosson, and J. A. Bangham. A comparison of linear and nonlinear scale-space filters in noise. *Signal Processing*, VIII-1,isbn 88-86179-83:1777 1781, 1996.

[65] V. D. Heijden. Edge and line feature extraction based on covariance models. *IEEE Transactions on Pattern Analysis and Machine Intelligence*. 17:69–77, 1995.

[66] H. J. A. M. Heijmans and J. Goutsias. Nonlinear multiresolution signal decomposition schemes - Part II: Morphological wavelets. *IEEE Transactions on Image Processing*, 9(11):1897–1913, 2000.

[67] M. A. Hurn, K. V. Mardia, T. J. Hainsworth, J. Kirkbride, and E. Berry. Bayesian fused classification of medical images. In *Tech. Rep. No. STAT/95/20/C, Univ. of Leeds, Dept. of Statistics, 1995*, volume -. -, 1995.

[68] P. T. Jackway. Morphological scale-space. In *Proceedings, 11th IAPR International Conference on Pattern Recognition*, pages 252–255, the Hague, the Netherlands, September, 1992, 1992.

[69] P. T. Jackway. Multiscale image processing: A review and some recent developments. *Journal of Electrical and Electronics Engineering*, 13(2):88–98, 1993.

[70] P. T. Jackway. Gradient watershed in morphological scale-space. *IEEE Transactions on Image Processing*, 5:913–921, 1996.

[71] P. T. Jackway and M. Deriche. Scale-space properties of multiscale dilation-erosion. *IEEE Transactions on Pattern Analysis and Machine Intelligence*, Pattern Analysis and Machine Intelligence-18:38–51, 1996.

[72] A. K. Jain. *Fundamentals of Digital Image Processing.* Prentice-Hall, Englewood Cliffs, N.J., 1989.

[73] J. C. Klein and J. Serra. The texure analyzer. *J. Microscopy*, 95:349–356, 1977.

[74] J. Koenderink. The structure of images. *Biological Cybernatics*, 50:363–370, 1984.

[75] X. Kong and J. Goutsias. A study of pyramidal techniques for image representation and compression. *Journal of Visual Communication and Image Representation*, 5:190–203, 1994.

[76] C. J. Kuo, C. H. Lin, and C. H. Yeh. Noise reduction of vq encoded images through anti-gray coding. *IEEE Transactions on Image Processing*, 8:33–40, 1999.

[77] C. Lantuejoul and F. Maisonneuve. Geodesics methods in image analysis. *Pattern Recognition*, 17:117–187, 1984.

[78] J. S. Lee. Digital image enhancement and noise filtering by use of local statistics. *IEEE Transactions on Pattern Analysis and Machine Intelligence*, Pattern Analysis and Machine Intelligence-2:165–, 1980.

[79] J. S. Lee. Refined filtering of image noise using local statistics. *Computer Graphics and Image Processing-4*, 15:380–389, 1981.

[80] P. F. Leonard. Pipeline architechture for real time machine vision. In *Proc. IEEE Comp. Soc. Workshop on Computer Architecture for Pattern Analysis and Image Database Management*, pages 502–505, 1985.

[81] H. Li, B. S. Manjunath, and S. K. Mitra. Multisensor image fusion using the wavelet transform. *Graphical Models and Image Processing*, 57(3):235–245, 1995.

[82] L. M. Lifshitz and S. M. Pizer. Multi-resolution hierarchical approach to image segmentation based on intensity extrema. *IEEE Transactions on Pattern Analysis and Machine Intelligence*, 12(6):529–540, 1990.

[83] T. Lindeberg. *Scale-Space Theory in Computer Vision.* Kluwer Academic Publishers, Dordrecht, Netherlands, 1994.

[84] R. C. Luo, M. Lin, and R. S. Scherp. Multisensor integration and fusion in Intelligent Systems. *IEEE Transactions on Systems Man and Cybernatics*, 19:901 . 1989.

[85] S. Mallat. *A wavelet tour of signal processing 2nd ed.* Academic Press, NY, 1999.

[86] P. Maragos. Pattern spectrum and multiscale shape representation. *IEEE Transactions on Pattern Analysis and Machine Intelligence*, 11:701–716, 1989.

[87] P. Maragos. A representation theory for morphological image and signal processing. *IEEE Transactions on Pattern Analysis and Machine Intelligence*, 11:586 599, 1989.

[88] P. Maragos. Differential morphology and image processing. *IEEE Transactions on Image Processing*, 5(6):922–937, 1996.

[89] P. Maragos and F. Meyer. Nonlinear PDEs and numerical algorithms for modeling levelings and reconstruction filters. *Lecture Notes in Computer Science*, 1682:363–374, 1999.

[90] P. Maragos and R. W. Schafer. Morphological filters - Part I: Their set theoretic analysis and relations to linear shift-invariant filters. *IEEE Transactions on Acoustics, Speech and Signal Processing*, 35(5):1153–1169, 1987.

[91] P. Maragos and R. W. Schafer. Morphological filters - Part II: Their relations to median, order-statistics, and stack filters. *IEEE Transactions on Acoustics, Speech and Signal Processing*, 35(5):1170–1184, 1987.

[92] K. V. Mardia and I. L. Dryden. *Statistical Shape Analysis.* Wiley, Chichester, 1998.

[93] K. V. Mardia and T. J. Hainsworth. Image warping and bayesian reconstruction with grey-level templates. In K. V. Mardia and G. K. Kanji, editors, *Advances in Applied Statistics, Statistics and Images.* Carfax Publishing Company, -, 1993.

[94] D. Marr. *Vision - A Computational Investigation into the Human Representation and Processing of Visual Information.* Freeman, San Francisco, CA, 1982.

[95] D. C. Marr and E. Hildreth. Theory of edge detection. In *Proc. Royal Soc. Lond, Vol. B, 1962*, pages 187–217, London, 1962.

[96] G. M. Matheron. *Random sets and integral in Geometry.* Wiley, New York, 1975.

[97] G. K. Matsopoulos, S. Marshall, and J. N. H. Brunt. Multiresolution morphological fusion of MR and CT images of the human brain. *IEE Proc.-Vis. Image Signal Process.*, 141:137–142, 1994.

[98] F. Meyer. Contrast feature extraction. In J. L. Chermant, editor, *Quantitative Analysis of Microstructures in Material Sciences, Biology and Medicine.* Riederer Verlag, Stuttgart, Germany, 1978.

[99] F. Meyer. Integrals and gradients of images. In *Proc. SPIE vol. 1769: Image Algebra Morph. Image Processing III*, volume 1769, pages 200–211, 1992.

[100] F. Meyer. Morphological image segmentation for coding. In *1st workshop on mathematical morphology and its applications to signal processing,Ed. J. Serra and P. Salembier*, pages 46–51, Bercelona, Spain, 1993.

[101] F. Meyer. Topographic distance and watershed lines. *Signal Processing*, 38:113–125, 1994.

[102] F. Meyer. Morphological segmentation on a neighborhood graph. *Acta Stereologica*, 16(3):175–182, 1997.

[103] F. Meyer. Flooding and segmentation. In L. Vincent J. Goutsias and D. S. Bloomberg, editors, *Mathematical morphology and its applications to image and signal processing*. Kluwer Academic Publishers, USA, 2000.

[104] F. Meyer and S. Beucher. Morphological segmentation. *Journal of Visual Communication and Image Representation*, 1:21–46, 1990.

[105] F. Meyer and P. Maragos. Morphological scale-space representation with levelings. *Lecture Notes in Computer Science*, 1682:187–198, 1999.

[106] F. Meyer and P. Maragos. Multiscale morphological segmentations based on watershed, flooding, and eikonal pde. *Lecture Notes in Computer Science*, 1682:351–362, 1999.

[107] H. Minkowski. Volume and oberflache. *Math. Ann.*, 57:447–495, 1903.

[108] D. M. Mount, N. S. Netanyahu, and J. L. Moigne. Efficient algorithms for robust feature matching. *Pattern Recognition*, 32:17–38, 1999.

[109] D. Mukherjee and B. N. Chatterji. Adaptive neighborhood extended contrast enhancement and its modification. *Graphical Models and Image Processing*, 57:254–265, 1995.

[110] D. P. Mukherjee, P. Dutta, and D. Dutta Majumdar. Entropy theoretic fusion of multimodal medical images. In *Tech. Rep. ECSU/2/98, Electronics and Communication Sciences Unit, ISI, 1998*, volume -. -, 1998.

[111] S. Mukhopadhyay and B. Chanda. Multi-scale morphological noise smoothing of grayscale images. In *Proc. ICAPRDT'99, Calcutta, India, Dec 27- 29,1999.* pages 160–164, Calcutta, India, 1999.

[112] S. Mukhopadhyay and B. Chanda. Local contrast enhancement of grayscale images using multiscale morphology. In *Proc. ICVGIP-2000, Bangalore, India. Dec 20- 22,2000*, pages 17–24, Bangalore, India, 2000.

[113] S. Mukhopadhyay and B. Chanda. A multiscale morphological approach to local contrast enhancement. *Signal Processing*, 80(4):685–696. 2000.

[114] S. Mukhopadhyay and B. Chanda. Fusion of 2d grays-cale images using multiscale morphology. *Pattern Recognition*, 34(10):1939–1949, 2001.

[115] S. Mukhopadhyay and B. Chanda. Local contrast enhancement of color images using multiscale morphology. *Communicated to IEEE Transactions on Image Processing*, -:-, 2001.

[116] S. Mukhopadhyay and B. Chanda. Multiscale morphological segmentation of gray-scale images. *IEEE Transactions on Image Processing, in press*, -:-, 2001.

[117] S. Mukhopadhyay and B. Chanda. An edge preserving noise smoothing technique using multiscale morphology. *Signal Processing*, 82(4):527–544, 2002.

[118] S. Mukhopadhyay and B. Chanda. Hue preserving color image enhancement using multiscale morphology. *Accepted for publication in Proceedings of ICVGIP-2002 to be held in India during Dec 16–18, 2002*, -:-, 2002.

[119] P. M. Narendra and R. C. Fitch. Real-time adaptive contrast enhancement. *IEEE Transactions on Pattern Analysis and Machine Intelligence*, Pattern Analysis and Machine Intelligence-3:655–661, 1981.

[120] W. J. Niessen, K. L. Vincken, J. Weickert, and M. A. Viergever. Nonlinear multiscale representations for image segmentation. *Computer Vision and Image Understanding*, 66:233–245, 1997.

[121] R. B. Paranjape, W. M. Morrow, and R. M. Rangayyan. Adaptive-neighborhood histogram equalization for image enhancement. *Graphical Models and Image Processing*, 54:259–267, 1992.

[122] K. R. Park and C. N. Lee. Scale-space using mathematical morphology. *IEEE Transactions on Pattern Analysis and Machine Intelligence*, 18:1121 1126, 1996.

[123] P. Perona and J. Malik. Scale-space and edge detection using anisotropic diffusion. *IEEE Transactions on Pattern Analysis and Machine Intelligence*, 12(7):629–639, 1990.

[124] S. M. Pizer, E. P. Amburn, J. D. Austin, R. Cromartie, A. Geselowitz, T. Geer, B. H. Romeny, J. B. Zimmerman, and K. Zuiderveld. Adaptive histogram modification and its variation. *Computer Vision, Graphics and Image Processing*, 39:355–368, 1987.

[125] C. C. Pu and F. Y. Shih. Threshold decomposition of grey-scale soft morphology into binary soft morphology. *CVGIP-Graphical Models and Image Processing*, 57(6):522–526, 1995.

[126] J. F. Rivest, S. Beucher, and S. Delhomme. Marker-controlled segmentation: an application to electrical borehole imaging. *J. Electron. Imaging*, 1:136 142, 1992.

[127] J. B. T. M. Roerdink and A. Meijster. The watershed transform: definitions, algorithms, and parallellization strategies. In J. Goutsias and H.J.A.M. Heijmans, editors, *Mathematical Morphology*, pages 187–228. IOS Press, Amsterdam, 2000.

[128] A. Rosenfeld. *Multiresolution image processing and analysis, Vol. 12, Springer series in information sciences.* Springer-Verlag, NY, 1984.

[129] A. Rosenfeld and L. Davis. Image segmentation and image modeling. *Proc IEEE*, 67(5):764–772, 1979.

[130] A. Rosenfeld, R. A. Hummel, and S. W. Zucker. Scene labeling by relational operations. *IEEE Transactions Systems, Man, and Cybernetics*, SMC(6):420–424, 1976.

[131] A. Rosenfeld and A. C. Kak. *Digital Picture Processing, 2nd ed., Vol. 1 & 2.* Academic Press, NY, 1982.

[132] A. Rosenfeld and M. Thurston. Edge and curve detection for visual scene analysis. *IEEE Transactions on Computers*, C-20:562–569, 1971.

[133] F. Safa and G. Flouziat. Speckle removal on radar imagery based on mathematical morphology. *Signal Processing*, 16:319–333, 1989.

[134] P. Salembier. Morphological multiscale segmentation for image coding. *Signal Processing*, 38:359–386, 1994.

[135] P. Salembier and M. Pardas. Hierarchical morphological segmentation for image sequence coding. *IEEE Transactions on Image Processing*, 3:639–651, 1994.

[136] P. Salembier and J. Serra. Morphological multiscale image segmentation. In *Proceedings, Visual Communication and Image Processing*, pages 620–631, Boston, MA, 1992.

[137] P. Salembier and J. Serra. Flat zones filtering, connected operators and filters by reconstruction. *IEEE Transactions on Image Processing*, 4(8):1153–1160, 1995.

[138] D. Salomon. *Data Compression : The Complete Reference*. Springer-Verlag, NY, 2000.

[139] R. Schettini. A segmentation algorithm for color images. *Pattern Recognition Letters*, 14:499–506, 1993.

[140] D. Schonfeld and J. Goutsias. Optimal morphological pattern restoration from noisy binary images. *IEEE Transactions on Pattern Analysis and Machine Intelligence*, 13:14–29, 1991.

[141] C. A. Segall and S. T. Acton. Morphological anisotropic diffusion. In *Proc. 1997 IEEE International Conference on Image Processing, Santa Barbara, CA, October 26-29*, volume III, pages 348–351, 1997.

[142] J. Serra. *Image analysis using mathematical morphology*. Academic Press, London, 1982.

[143] C. Shekhar, V. Govinder, and R. Chellappa. Multisensor image registration by feature consensus. *Pattern Recognition*, 32:39–52, 1999.

[144] M. Shyu and J. Leou. A geneticle algorithm approach to color image enhancement. *Pattern Recognition*, 31(7):871–880, 1998.

[145] J. Sijbers, P. Scheunders, M. Verhoye, A. Van der Linden, D. Van Dyck, and E. Raman. Watershed based segmentation of 3d mr data for volume quantization. *Magn. Reson. Imaging*, 15:679–688, 1997.

[146] K. Sivakumar and J. Goutsias. Discrete morphological size distributions and densities: Estimation techniques and applications. *Journal of Electronic Imaging*, 6:31–53, 1997.

[147] P. Soille. *Morphological Image Analysis.* Springer-Verlag, Berlin New York, 1999.

[148] X. Song and Y. Neuvo. Robust edge detector based on morphological filters. *Pattern Recognition Letters*, 14:889–894, 1993.

[149] S. R. Sternberg. Gray scale morphology. *Computer Graphics and Image Processing*, 35:333–355, 1986.

[150] R. N. Strickland, C. S. Kim, and W. F. McDonnell. Digital color image enhancement based on the saturation component. *Optical Engineering*, 26:609 616, 1987.

[151] B. Tang and G. Sapiro. Color image enhancement via chromaticity diffusion. *IEEE Transactions on Image Processing*, 10(5):701 707, 2001.

[152] S. Tanimoto and T. Pavlidis. A hierarchical structure for picture processing. *Computer, Vision, Graphics, and Image Processing*, 4:104 119, 1975.

[153] B. M. ter Haar Romeny (Ed.). *Geometry-driven diffusion in Computer Vision.* Kluwer, Dordrecht, 1994.

[154] A. Toet. Adaptive multi-scale contrast enhancement through non-linear pyramid recombination. *Pattern Recognition Letters*, 11(11):735–742, 1990.

[155] A. Toet. A hierarchical morphological image decomposition. *Pattern Recognition Letters*, 11(4):267–274, 1990.

[156] A. Toet. Multi-scale color image enhancement. *Pattern Recognition Letters*, 13(3):167–174, 1992.

[157] J. K. Udupa and S. Samarasekera. Fuzzy connectedness and object definition: Theory, algorithms, and applications in image segmentation. *Graphical Models and Image Processing*, 58:246 261, 1996.

[158] L. Vincent. Morphological area openings and closings for gray-scale images. In *Proc. NATO Shape in Picture Workshop, Driebergen, The Netherlands*, pages 197–208, 1992.

[159] L. Vincent. Gray-scale area openings and closings, their efficient implementation and applications. *In Jean Serra and Phillipe Salembier, editors, Proceedings of the international workshop on mathematical morphology and its applications to signal processing*, pages 22–27, 1993.

[160] L. Vincent. Morphological grayscale reconstruction in image analysis: Applications and efficient algorithms. *IEEE Transactions on Image Processing*, 2:176–201, 1993.

[161] L. Vincent. Granulometries and opening trees. In J. Goutsias and H.J.A.M. Heijmans, editors, *Mathematical Morphology*, pages 57–90. IOS Press, Amsterdam, 2000.

[162] T. Vlachos and A. G. Constantinides. Graph-theoretical approach to color picture segmentation and contour classification. In *IEE Proceedings Communication, Speech and Vision*, volume 140, pages 36–45, 1993.

[163] N. Volkmann. A novel three-dimensional variant of the watershed transform for segmentation of electron density maps. *J. Structural biology*, 138:123–129, 2002.

[164] J. Weickert. *A review of non-linear diffusion filtering, Lecture Notes in Computer Science, Vol. 1252, invited paper, pp. 3-28.* Springer, Berlin, 1997.

[165] J. Weickert. *Anisotropic diffusion in image processing.* ECMI Series, Teubner-Verlag, Stuttgart, 1998.

[166] J. S. Weszka and A. Rosenfeld. Threshold evaluation techniques. *IEEE Transactions on Systems, Man and Cybernetics*, 8:622–629, 1978.

[167] A. Witkin. Scale-space filtering. In *International Joint Conference on Artificial Intelligence*, pages 1019–1021, Karlsruhe, West Germany, 1983.

[168] A. P. Witkin. Scale-space filtering: a new approach to multiscale description. In *Image Understanding, S. Ullman and W Richards, Eds*, pages 79–95, Ablex, Norwood, NJ, 1984.

[169] W. Wu, M. J. Wang, and C. Liu. Performance evaluation of some noise reduction methods. *Graphical Models and Image Processing*, 54(2):134–146, 1992.

[170] H. Zhu, F. H. Y. Chan, and F. K. Lam. Image contrast enhancement by constrained local histogram equalization. *Computer Vision and Image Understanding*, 73(2):281–290, 1999.

List of publications of S. Mukhopadhyay

- B. Chanda, S. Mukhopadhyay, and P. Ghosh. Multi-scale morphological fusion of MR and CT images. In *Proc. ICVGIP-1998, New Delhi, India, Dec 21-23,1998*, pages 21–26, New Delhi, India, 1998.

- S. Mukhopadhyay and B. Chanda. A scheme for vectorization of engineering drawings. In *Proc. ICVGIP-98, New Delhi, India, Dec 21- 23,1998*, pages 396–401, New Delhi, India, 1998.

- S. Mukhopadhyay and B. Chanda. A simple approach for vectorization of engineering drawings. In *Proc. GREC'99, Jaypur, India, Sept 26- 27, 1999*, pages 24–31, Jaypur, India, 1999.

- S. Mukhopadhyay and B. Chanda. Multi-scale morphological noise smoothing of grayscale images. In *Proc. ICAPRDT'99, Calcutta, India, Dec 27- 29,1999*, pages 160–164, Calcutta, India, 1999.

- S. Mukhopadhyay and B. Chanda. A multi-scale morphological approach to local contrast enhancement. *Signal Processing*, 80(4):685–696, 2000.

- S. Mukhopadhyay and B. Chanda. Local contrast enhancement of grayscale images using multi-scale morphology. In *Proc. ICVGIP-2000, Bangalore, India, Dec 20- 22,2000*, pages 17–24, Bangalore, India, 2000.

- S. Mukhopadhyay and B. Chanda. Fusion of 2d grayscale images using multi-scale morphology. *Pattern Recognition*, 34(10):1939–1949, 2001.

- S. Mukhopadhyay and B. Chanda. An edge preserving noise smoothing technique using multi-scale morphology. *Signal Processing*, 82(4):527–544, 2002.

- S. Mukhopadhyay and B. Chanda. Multi-scale morphological segmentation of gray-scale images. *Accepted in IEEE Transactions on Image Processing* in 2002.

- S. Mukhopadhyay and B. Chanda. Local contrast enhancement of color images using multi-scale morphology. *Communicated to IEEE Transactions on Image Processing* in July 2001.

- S. Mukhopadhyay and B. Chanda. Hue preserving color image enhancement using multiscale morphology *Accepted for oral presentation in ICVGIP-2002* to be held during Dec 16–18, 2002.